SURFACE PLASMON MICROARRAY AND VOLTAGE-DRIVEN BIOCATALYSIS FOR DRUG DEVELOPMENT AND BIOELECTRONICS

By

CHARUKSHA THAMEERA WALGAMA

Bachelor of Science in Chemistry
University of Kelaniya
Sri Lanka
2010

Submitted to the Faculty of the
Graduate College of the
Oklahoma State University
in partial fulfillment of
the requirements for
the Degree of
DOCTOR OF PHILOSOPHY
July, 2017

SURFACE PLASMON MICROARRAY AND

VOLTAGE-DRIVEN BIOCATALYSIS FOR DRUG

DEVELOPMENT AND BIOELECTRONICS

Dissertation Approved:

Dr. Sadagopan Krishnan

Dissertation Adviser

Dr. K. Darrell Berlin

Dr. Nicholas F. Materer

Dr. Barry K. Lavine

Dr. Julie Angle

ACKNOWLEDGEMENTS

This doctorial study would not have been possible without the support and guidance of a few special people in my life. I would like to show my heart-felt gratitude to my PhD advisor and committee chair, Dr. Sadagopan Krishnan, who continually and convincingly convey his guidance and spirit of inspiration towards my research. It was my pleasure to work with my advisor in an enthusiastic research environment. I would like to thank my graduate committee members Dr. K. Darrell Berlin, Dr. Nicholas F. Materer, Dr. Barry K. Lavine (Department of Chemistry of OSU, Stillwater, OK USA) and Dr. Julie Angle (College of Education, OSU, Stillwater, OK, USA), whose comments and ideas nourish my capabilities of inventions in regard to research.

I'm truly grateful for the donors of my scholarships [Electrochemical Society (ECS) for W. Richards Summer Fellowship (2016), OSU Chemistry Department for O. C. Dermer, Henry P. Johnston and Skinner Fellowships (2012-2016), OSU Spears School of Business for Creativity, Innovation and Entrepreneurship (CIE) Scholar Award (2015) and OSU Graduate College for Distinguished Graduate Fellow (DGF) Award (2015-2017)].

Also, I thank my current and former lab mates Dr. Vini Singh, Dr. Manoj K Patel, Dr. K. S. Prasad, Rajasekhar Nerimetla, Gayan Premaratne, Jinesh Niroula, Zainab Al Mubarak, Asantha Dharmaratne, Sabrina Farias, Jimmy Dickinson, James Moulton, Mayowa Akinwale, Matthew Gallman, Roberto Montealegre, Ryan Matlock, and Anuruddha Pathiranage, whom I spent a valuable time with sharing knowledge and experience.

Furthermore, I give my special thanks to all my professors at University of Kelaniya, Sri Lanka for providing me the foundation of science education and all my teachers at D.S. Senanayake College, Colombo 7, Sri Lanka for providing me a strong primary and secondary educational background.

Finally, I would like to acknowledge with gratitude my father (Upali Walgama), mother (Thilaka Walgama), wife (Lakmini Senavirathna), brother (Gihan Walgama) and all other family members for their unconditional love and care.

Name: CHARUKSHA THAMEERA WALGAMA

Date of Degree: JULY, 2017

Title of Study: SURFACE PLASMON MICROARRAY AND VOLTAGE-DRIVEN BIOCATALYSIS FOR DRUG DEVELOPMENT AND BIOELECTRONICS

Major Field: CHEMISTRY

Abstract: The objectives of the research described in this dissertation are driven with a broader motivation to provide scientific solutions to real world problems related to human health and cleaner energy. Under global health issues, there are many challenges that need to be addressed, specifically in the laborious drug development process and characterization of small-molecule cancer drugs. The research strategies described in this work focus on developing analytical solutions for drug candidate identification, preclinical metabolite screening, and quality assurance of active pharmaceutical ingredients. A surface plasmon methodology was developed to study binding kinetics of oncogenic protein-protein interactions and their inhibition by small-molecule drugs. Additionally, a rapid one-step construction of the human liver membrane bioelectrodes for inexpensive, electrochemical drug metabolism and inhibition was formulated. Thirdly, the applicability of the screen printed electrodes was validated towards single drop electrocatalysis of pharmaceuticals as a cost-effective and instant analytical tool to determine the purity of an active chemical form of a drug. Under the focus of biocatalysis, high efficient nanostructure bioelectrode designs have been investigated for model catalytic reactions.

TABLE OF CONTENTS

LIST OF TABLES

CHAPTER 2

CHAPTER 3

CHAPTER 4

CHAPTER 5

TABLE PAGE

CHAPTER 6

TABLE PAGE

LIST OF FIGURES

CHAPTER 1

FIGURE PAGE

CHAPTER 2

FIGURE PAGE

CHAPTER 3

FIGURE PAGE

CHAPTER 4

FIGURE PAGE

CHAPTER 5

FIGURE PAGE

CHAPTER 6

FIGURE PAGE

CHAPTER 1

RESEARCH OVERVIEW

This chapter provides a concise account of this dissertation. The research objectives (see Figure 1) were driven with a broader motivation to provide scientific solutions for real world issues related to health and energy applications. In the first branch (see Figure 1), array based optical imaging and electrochemical methodologies to provide constructive insights for a drug development process were investigated. In the second branch, the implications of nanostructure bioelectrode architectures for catalytic applications were investigated.

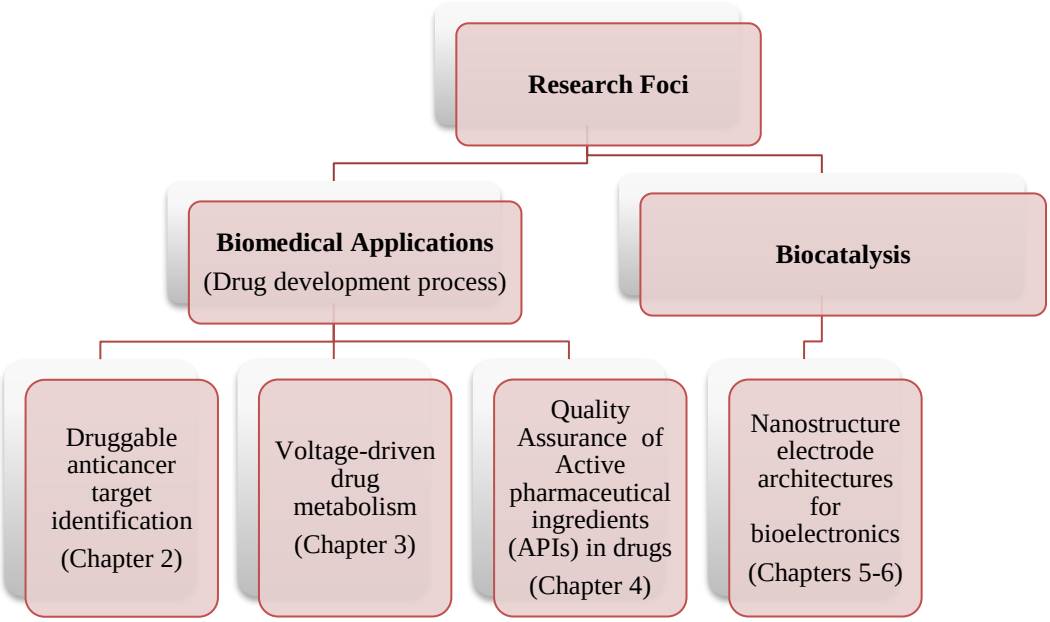

Figure 1. Major research paradigms of the dissertation

1.1 Research Foci on Biomedical Applications

The time to develop a pharmaceutical drug and bring it to the market takes on average 12.5 years and billions of dollars. This is a laborious multi-phase process, which involves discovering druggable targets, performing pre-clinical and clinical studies, obtaining regulatory certifications and initiating the manufacturing process (Figure 2).[1-3]

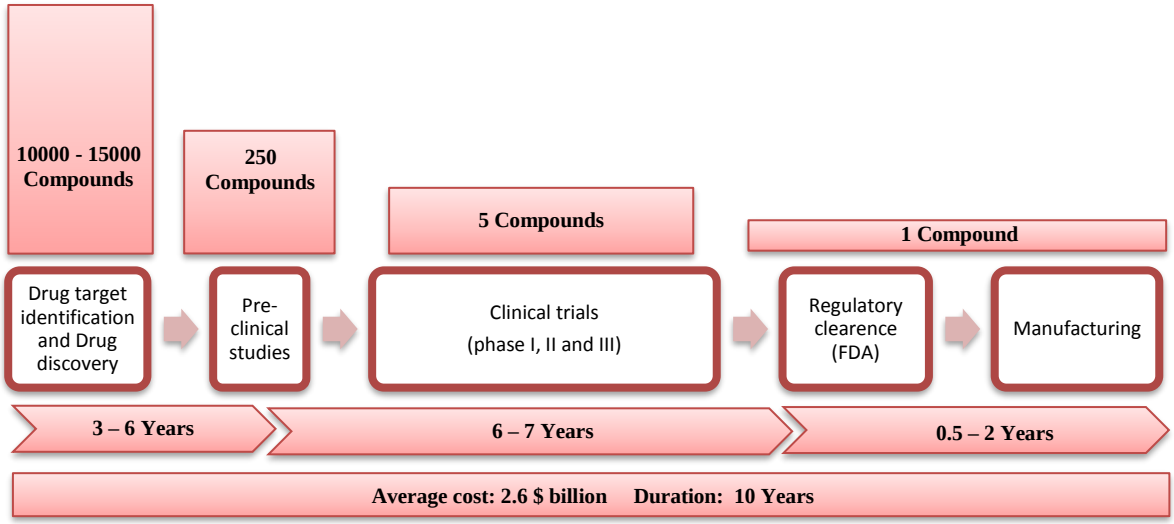

Figure 2. Drug development process, length and cost[4] (source: Pharmaceutical Research and Manufacturers of America).

As part of the research described in this dissertation, analytical knowledge gained in these studies has provided better scientific intuitions to various stages of the drug development process.

1.1.1 Cancer Target Identification and Inhibition by Small Molecule Drugs (see Chapter 2)

Cancer target identification and anticancer drug development have gained an attention in biomedical pre-clinical research.[5] A surface plasmon resonance imaging (SPRi) microarray-platform has been developed in the research described in this dissertation to study druggable cancer protein-protein interactions with binding kinetics.[6] In vitro interactions involving tumor suppressor p53 and its negative regulator murine double minute 2 (MDM2)[7] was successfully imaged on a 16

spot SPRi multi-array chip with high sensitivity and specificity over mutant controls. This imaging array platform involved a rapid microfluidic system attached to the SPR imager and a single step immobilization of p53 transactivational domain (TAD) peptides on the gold surface (see Figure 3) as self-assembled monolayers (SAMs). Different nanomolar to micromolar concentrations of an MDM2 oncoprotein in a buffer solution was allowed to bind to the surface of p53 TAD. Real time percentage reflectivity changes of the array spots upon the interaction of MDM2 to surface p53 TAD were monitored and used for calculating apparent binding kinetics. Additionally, the inhibition of MDM2-p53 interaction by Nutlin-3a (a potential drug in a clinical stage) was also measured. Moreover, molecular level mass changes were obtained using a quartz crystal microbalance (QCM). It is envisioned that an imaging array combined with a mass sensor could be used to quantitatively study any protein-protein interactions and to screen for both binding and potency evaluations of small molecules.

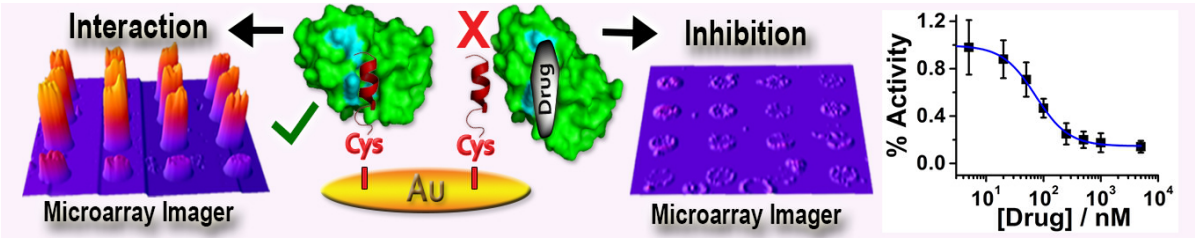

Figure 3. Micro array imager for the identification of cancer protein interactions and their inhibition by small molecule drugs.

1.1.2 Potential Driven, Microsomal Drug Metabolite synthesis and Inhibition Assays (see Chapter 3)

Aside from the target identification, the most prominent burden of the drug development process is the pre-clinical screening process, which ensures the effectiveness and safety of the drug. During this screening process, how a drug works; which chemical products (metabolites) are formed; and whether it is safe enough to be tested in humans are evaluated. Therefore, examining the metabolic

fate of drugs is an essential part of the drug development process. Metabolism is a course of biotransformation of drugs into different chemical entities, prominently through liver enzymatic reactions. It is a natural activity in our body to increase drug hydrophilicity and decrease toxicity.[8] However, in some cases, drugs can produce reactive metabolites, which are harmful and toxic for biological systems. Related to the pharmaceutical industry, the efficacy and beneficial properties of a drug depend on the biological activity of the metabolites formed in the liver. Therapeutic or toxic properties of those metabolites should be investigated sensibly since the toxicity or side effects of a drug can counteracts its therapeutic effectiveness. Therefore, all synthetic drugs should be screened through liver mimics under in-vitro conditions before any drug is subjected to clinical studies.

Membrane bound enzymes in hepatocytes (liver cells) govern the majority of metabolic reactions (hydrolysis, oxidation, reduction and conjugation). Human liver microsomes (HLM), which are subcellular fractions derived from differential centrifugation of liver homogenates, are used as rich source of liver enzymes (cytochrome P450s (CYPs), cytochrome P450 reductases (CPRs), carboxyl esterases, and UDP- glucuronosyltransferases (UGTs)) for in-vitro drug screening assays.[9] Presently, these studies are conducted using hepatic or purified liver enzyme-based biological assays. Longer incubation times, lower yield of drug metabolites, use of expensive NADPH cofactor and purified enzymes, and tedious purification protocols are some practical issues integrated with these conventional biological assays.[10] A simple HLM based bioreactor technology for electrochemical drug activity assay has been developed as part of this dissertation research.

In this preliminary study, the influence of various electrode materials on the direct electron transfer and electrocatalytic properties of one-step immobilized HLMs was examined. Electrode roughness and surface defects were found to favor enhanced amounts of electroactive microsomal proteins, and the surface oxygen density of a carbon electrode influences the charge transport kinetics

between the electrode surface and microsomal enzymes. The CYP-specific bioactivity of the liver microsomal film on the electrode was confirmed by monitoring the electrocatalytic conversion of testosterone to 6β-hydroxytestosterone and its inhibition by the CYP-specific ketoconazole inhibitor (see Figure 4). These findings provided successful implications in the design of a one-step, electrochemical bioelectrode for drug activity and inhibition assay for preclinical drug development application.

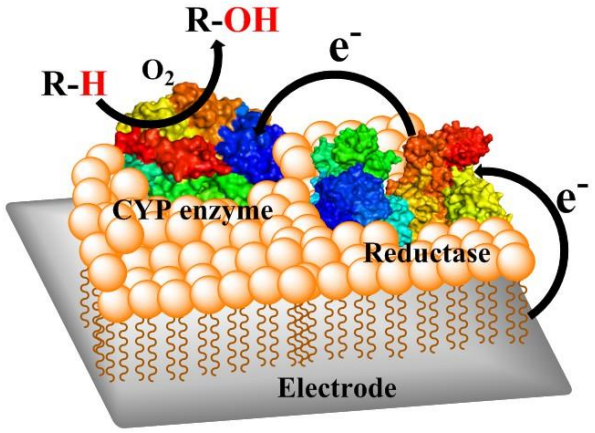

Figure 4. Potential driven drug metabolism by HLM

1.1.3 Single Drop Electro-analysis for low-cost Quality Control Testing of Oxidative Pharmaceuticals (see Chapter 4)

Quality control analysis of drugs for their active pharmaceutical ingredients (APIs) is an important process in drug manufacturing.[11] The applicability of screen-printed electrodes was validated as a cost-effective and instant analytical tool in the quality assurance process of oxidative drugs to quantify active pharmaceutical ingredients. Electroanalysis of oxidative pharmaceuticals as single 50 µL drops on screen printed electrodes (SPEs) modified with carboxylated multi-walled carbon nanotubes was demonstrated (see Figure 5) with low limits of detection and high sensitivity

expressed in nA current per µM analyte. It was determined that chemical structure, molecular size, and polar/nonpolar properties contribute significantly to the interaction of a single drop of analyte with the electrode surface to facilitate interfacial charge transport, and thus the oxidation current. This approach was tested using commercially available model pharmaceuticals with percentage recovery in the range of 92-99%. These successful findings suggest the applicability of a single drop electroanalysis as a cost-effective and instant analytical tool for the quality assurance (QA) process in the pharmaceutical industry, especially to determine the purity of a drug.

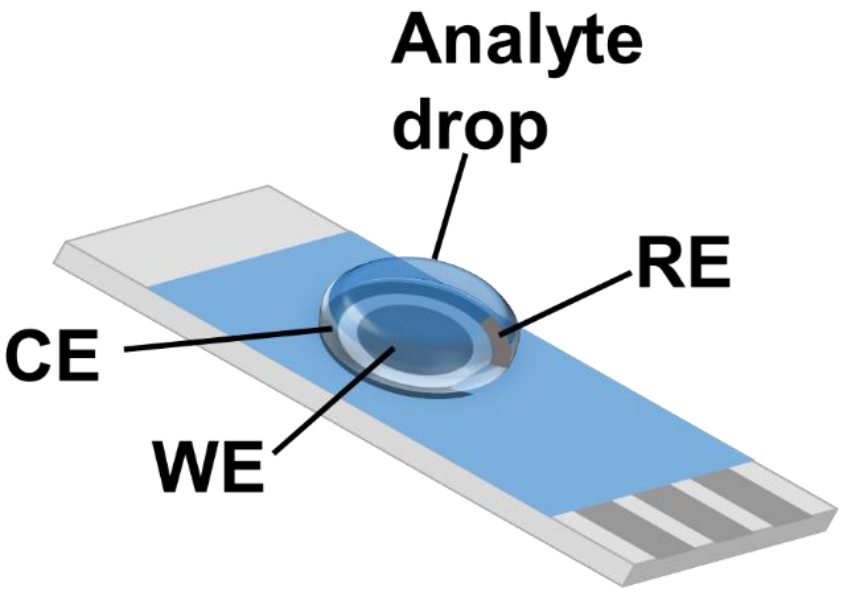

Figure 5. Single drop electroanalysis on a screen printed electrode (WE- working electrode, CE- counter electrode, and RE- reference electrode).

1.2 Research Foci on Bio-electrocatalysis

1.2.1 Nanostructure Electrode Architectures for Bioelectronics (see Chapters 5 and 6)

Novel bioelectronics rely on the surface design of electrodes to sustain active redox enzymes with good stability and electronic connectivity.[11-13] It has been demonstrated in the dissertation research that tailoring of the electrode with carbon nanostructure modifications can facilitate the controlled immobilization of redox enzymes and offer enhanced direct electron transfer electrocatalytic properties.[14] One study performed as part of the dissertation research proposed that edge plane, pyrolytic graphite electrodes plays an important role in exposing a large proportion of the basal planes of the carbon nanotubes to allow enhanced π-π stacking of a pyrenyl compound and subsequent high density protein immobilization yielding large electrocatalytic currents (see Figure 6).

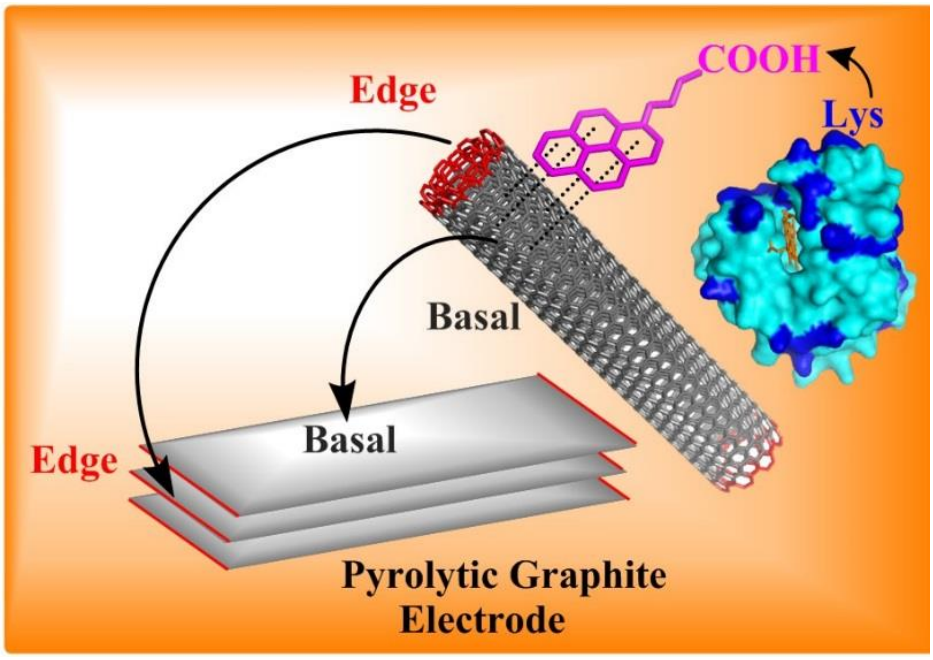

Figure 6. Proposed electrode effect on carbon nanotube orientation.

Another study described in this dissertation showed an unprecedented peroxide reduction current density by MP-11 (an 11-amino acid heme-iron peptide) immobilized on the similar nanostructure design (see Figure 7). Electrocatalytic activities of large, fragile, redox-center buried, or otherwise difficult to study metalloenzymes can be overcome by changing the proteins into small catalytically-active redox domains that can effectively connect with the electrodes.

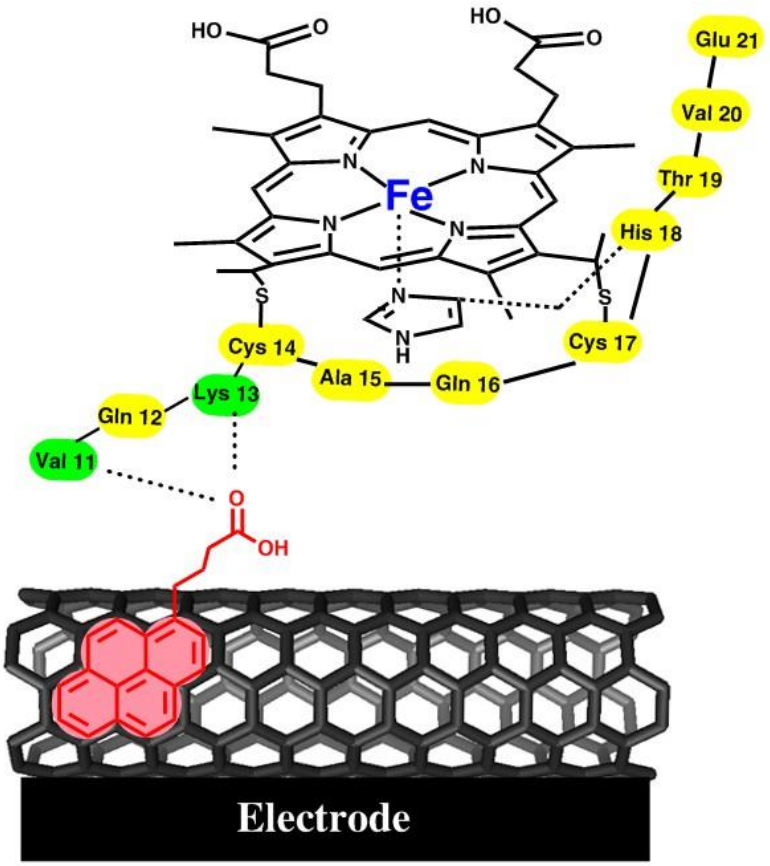

Figure 7. Covalent immobilization of MP-11 onto pyrenyl carbon-nanostructures.

1.3 References

1. Morgan, S.; Grootendorst, P.; Lexchin, J.; Cunningham, C.; Greyson, D. *Health Policy* **2011**, *100*, 4-17.
2. Lombardino, J. G.; Lowe, J. A. *Nature Reviews. Drug discovery* **2004**, *3*, 853-862.
3. DiMasi, J. A.; Grabowski, H. G.; Hansen, R. W. *J. Health Econ.* **2016**, *47*, 20-33.
4. Pharmaceutical Research and Manufacturers of America, PhRMA, 2016 [http://chartpack.phrma.org/2016-perspective/chapter-2/the-lengthy-costly-and-uncertain-biopharmaceutical-research-and-development-process (accessed 04-20-2017)].
5. Prasad, V.; De Jesús, K.; Mailankody, S. *Nature Reviews Clinical Oncology* **2017**.
6. Walgama, C.; Al Mubarak, Z. H.; Zhang, B.; Akinwale, M.; Pathiranage, A.; Deng, J.; Berlin, K. D.; Benbrook, D. M.; Krishnan, S. *Anal. Chem.* **2016**, *88*, 3130-3135.
7. Zhao, Y.; Aguilar, A.; Bernard, D.; Wang, S. *J. Med. Chem*. **2015**, *58*, 1038-1052.
8. Kirchmair, J.; Goller, A. H.; Lang, D.; Kunze, J.; Testa, B.; Wilson, I. D.; Glen, R. C.; Schneider, G. *Nature Reviews. Drug discovery* **2015**, *14*, 387-404.
9. Fasinu, P.; J. Bouic, P.; Rosenkranz, B. *Curr. Drug Metab*. **2012**, 13, 215-224.
10. Chan, T. S.; Yu, H.; Moore, A.; Khetani, S. R.; Tweedie, D. *Drug Metab. Disposition* **2013**, 41, 2024-2032.
11. Newton, P. N.; Green, M. D.; Fernández, F. M. *Trends Pharmacol. Sci.* **2010**, 31, 99-101.
12. Milton, R. D.; Wang, T.; Knoche, K. L.; Minteer, S. D. *Langmuir* **2016**, *32*, 2291-2301.
13. Zhang, A.; Lieber, C. M. *Chem. Rev.* **2016**, *116*, 215-257.
14. Walgama, C.; Krishnan, S. *J. Electrochem. Soc.* **2014**, *161*, H47-H52.
15. Rasmussen, M.; Abdellaoui, S.; Minteer, S. D. *Biosens. Bioelectron.* **2016**, *76*, 91-102.
16. Pankratov, D.; González-Arribas, E.; Blum, Z.; Shleev, S. *Electroanalysis* **2016**, *28*, 1250-1266.
17. Bandodkar, A. J.; Wang, J. *Electroanalysis* **2016**, *28*, 1188-1200.

CHAPTER 2

LABEL-FREE REAL-TIME MICROARRAY IMAGING OF CANCER PROTEIN-PROTEIN INTERACTIONS AND THEIR INHIBITION BY SMALL MOLECULES

2.1 Introduction

In addition to important biological roles, protein-protein interactions (PPIs) are known to block cellular defenses against diseases such as cancer. Thus, targeting oncogenic PPIs for the development of small molecule therapeutics has become a hot research topic.[1-3] One such PPI is be-tween p53, a tumor suppressor protein and transcriptional factor that plays an important role in cell cycle arrest, apoptosis, DNA repair, differentiation, and senescence,[4] and the oncoprotein murine double minute 2 (MDM2, an analogue of human double minute 2 protein),[5] which inhibits p53. In many tumors, overexpression of MDM2 has been shown to block the function of p53 and promote tumor progression. Numerous research groups have developed methods to detect biomolecules and study PPIs. For example, Corn and co-workers developed a 16-spot array for detection of genomic materials, proteins, and on-chip enzymatic reac-tions,[6,7] and Kim et al. characterized the binding of the yeast GAL4 dimerization domain to GAL11 protein, which is involved in galactose metabolism, using a chip-based cell cultivation system integrated with the SPRi technique.[8]

Using an SPR method, Domenici et al. found that the interaction of the bacterial protein azurin with p53 modulates MDM2–p53 binding.[9] Quantitative screening of small molecule G4 ligands on a G-quadruplex was also investigated using the SPRi technique.[10] Chen et al. demonstrated real-time monitoring of antibody-polypeptide binding as a drug screening platform using an SPRi microarray chip.[11] The interaction between human papillomavirus (HPV) E7 protein and retinoblastoma tumor suppressor protein (RB) was investigated for potential inhibition by an RB binding peptide (PepC) using an SPRi system.[12] Vassilev et al. analyzed small molecule-mediated inhibition of MDM2 binding to p53 using a conventional SPR assay method.[13] Recently, macrocyclic organopeptide hybrid inhibitors of the MDM2-p53 interaction were assessed by an SPR inhibition assay.[14,15]

Relevant to the importance of rapid small molecule screening arrays to inhibit cancer PPIs, an SPR imaging of cancer PPIs and their inhibition by small molecule drugs along with real-time binding kinetics determined for the same sample in a single assay wered presented. The microarray imaging feature of SPR over conventional non-imaging methods has the following advantages: (i) SPRi offers simplicity and relatively better throughput than conventional single or dual channel SPR. Thus, shorter assay times with enhanced precision of analytical data are available; (ii) An image-based bioanalytical approach allows easy interpretation of results useful for rapid biosensing and screening applications; (iii) SPRi allows measurements of mutlianalytes and multiple concentrations along with controls in a single measurement; and (iv) In addition to the rapid imaging feature of SPRi, one can obtain real time refractive index changes (association and dissociation curves) for all spots in the microarray and thus measure fundamental binding kinetics of any biological interaction (for e.g., protein-protein, antibody-antigen, nucleotide-protein, nucleotide-nucleotide, ligand-receptor, cell-cell, cell-biomolecule, and biomolecule-small molecule interactions).[16,17]

In this study, additional quantitative information were obtained by combining SPRi with a quartz crystal microbalance (QCM). Specifically, the interaction between p53 and MDM2 was utilized as a model system, because blocking the MDM2-p53 interaction by small molecules has been identified as a promising therapeutic strategy for cancer treatment.[18-20] To assess the specificity of the SPRi signals for MDM2 binding and drug inhibition assays, both the wild-type and mutant forms of p53 trans-activation domains (TADs) were examined.

Figure 1 shows the strategy for imaging cancer protein interactions and inhibition of these interactions by small molecules, providing binding kinetics and quantitative information.

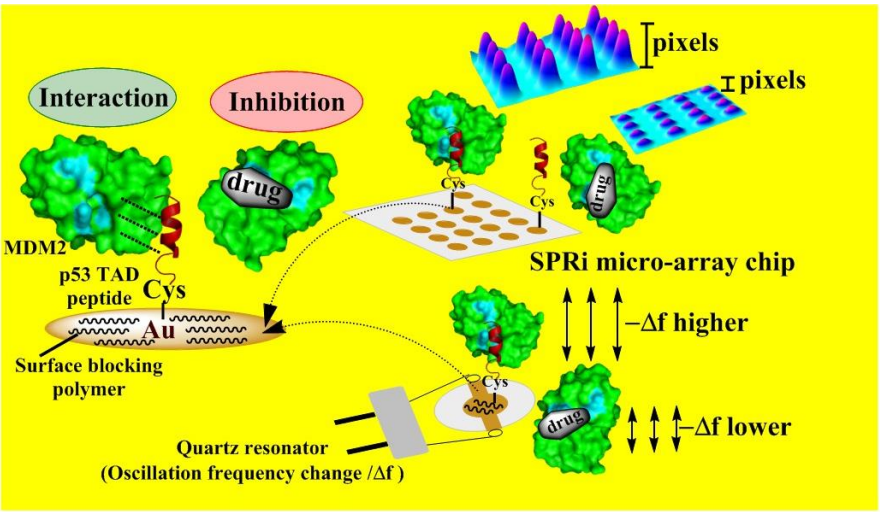

Figure 1. Schematic representation of SPRi and QCM strategies for detection of the MDM2-p53 TAD interaction and its inhibition by small molecules (MDM2 PDB: 1YCR).

p53 TAD peptides were immobilized as self-assembled monolayers (SAMs) on gold surfaces of both SPRi microarray chips and gold-coated quartz crystal resonators. The interaction of added MDM2 solution to surface p53 TAD was investigated by measuring the pixel intensity increase in SPRi and the frequency decrease (mass addition) in QCM. Rapid, label-free and real-time microarray analysis of PPIs with simplicity is preferred over other time consuming, tedious

analytical methods. Moreover, a microarray platform that can also provide binding kinetics and selectivity and allow detection of small molecule inhibitors with inhibition efficiency parameter has the potential to significantly advance the present paradigm of studying important cancer and other disease-related PPIs and screening of small molecule drugs. Such approaches are expected to accelerate subsequent cell based in vitro studies and the results of which can allow further in vivo evaluations of potential drug candidates.

2.2 Experimental

2.2.1 Materials

Wild-type (CSQETFSDLWKLLPEN, 1910.1 Da) and mutant (CSQETASDAAKLLPEN, 1676.8 Da) peptides of p53 TAD (15-29 aa), custom designed with an added free cysteine at the end of each peptide sequence, were purchased from Biomatik (Ontario, Canada). Nutlin-3a was purchased from Cayman Chemical Company (Ann Arbor, MI) and O-Methyl-heptaethylene glycol (mPEG-7) polymer was purchased from Polypure (Oslo, Norway). All other analytical grade chemicals were purchased from Sigma.

2.2.2 Expression and Purification of Recombinant MDM2

The expression and purification of the p53-binding N-terminal domain of MDM2 (17-125 amino acids, 12.5 kDa) was performed similar to the reported literature.[13] Briefly, *E. coli* BL21 (DE3) cells (Stratagene Inc., CA, USA), containing the MDM2 construct with an N-terminal 6 x His tag, was grown in Luria-Bertani nutrient medium with 50 μg mL^{-1} kanamycin at 37 ºC until OD_{600} reached 0.7. Then, 1 mM of isopropyl β-thiogalactopyranoside (IPTG) was added to the medium to induce MDM2 expression at 18 ºC overnight. Cells were harvested by centrifugation at 6000 g

for 20 min at 4 ºC and suspended in buffer A (20 mM Tris pH 7.0, 20 mM imidazole, 500 mM sodium chloride, 10 % glycerol).

The cells were lysed by a high-pressure homogenizer and centrifuged at 20,000 g for 30 min to remove insoluble debris. The supernatant containing MDM2 was loaded onto a Ni-NTA column (GE Healthcare). After washing with 100 mL of buffer A, the purified MDM2 was eluted with buffer B (20 mM Tris pH 7.0, 250 mM imidazole, 500 mM sodium chloride, 10% glycerol) and further purified by a gel filtration column (Superdex 200, GE Healthcare) with buffer C (50 mM sodium phosphate pH 7.0, 100 mM sodium chloride). Gel filtration fractions corresponding to the MDM2 elution peaks were collected and stored frozen as aliquots of small volumes at -80 ºC until use. The purity of the prepared MDM2 protein was confirmed by the standard polyacrylamide gel electrophoresis (SDS-PAGE) experiment.[21] By following the above described isolation and purification procedures, about 6 mg of purified MDM2 (> 98% purity, SDS-PAGE, see Figure 2) per liter of culture was obtained.

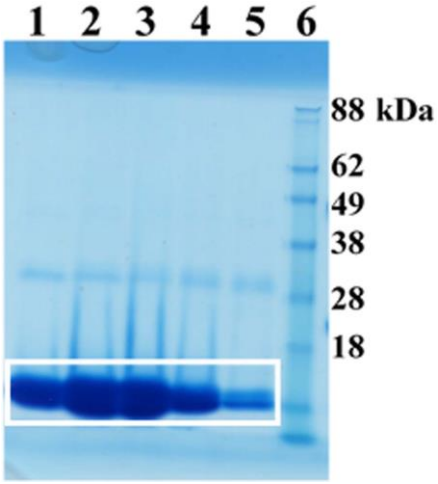

Figure 2. SDS-PAGE analysis of purified fractions of MDM2 from a gel filtration column (12.5 kDa size for monomer, Lanes 1-5). Lane 6 corresponds to standard molecular weight markers.

2.2.4 Preparation of SPRi Chips

Both the wild and mutant types of p53 peptides were separately immobilized as self-assembled monolayers (SAMs) on 16-spot, gold SPRi array chips. The SAMs were formed between the gold surface and cysteinyl thiol end groups of each p53 peptide by manually spotting 450 nL (per spot) of the respective peptide solutions (1.0 mg mL^{-1} in pH 7.4 phosphate buffer) using a pipette dispenser and incubating for 3 h at 4 ^{o}C inside a moisturized chamber to avoid drying of the samples. To reduce non-specific binding, p53-immobilized, gold surfaces were incubated with mPEG-7 blocking polymer (1% in pH 7.4 phosphate buffer) for 30 minutes. A series of drug solutions were prepared by diluting 1 mg mL^{-1} of stock solution of Nutlin-3a (1.72 mM) in dimethylformamide (DMF) for the inhibition study.

2.2.4 SPRi Measurements

Real time SPRi experiments were performed using a GWC SPRimager-II attached to a Pico Plus Elite Pump11 (Harvard apparatus, MA, USA) and a dual injector valve (Rheodyne Model 9725i PEEK injector, IDEX Health & Science LLC, CA, USA). The sample loop volume was 100 µL. Both the running and sample buffers were with 10 mM phosphate buffer, pH 7.4. SPRi chips were fabricated containing both the wild-type and mutant p53 TAD peptides (8 spots each) within a single microarray to assess selectivity. Additionally, drug-free and Nutlin-3a-incubated MDM2 samples were injected onto SPRi array spots featuring either the surface immobilized wild-type or the mutant p53 TAD peptide. Percentage reflectivity change (Δ%R) from the MDM2-p53 interaction and inhibition by a small molecule were recorded in real time. Finally, difference images (difference between pre- and post-binding events) were processed through ImageJ software to obtain 3D representations of the net changes from interaction or inhibition.[22]

2.2.5 QCM Analysis

The frequency change due to the interaction of surface p53 peptide with added MDM2 in buffer was validated with quantitative information using a QCM (Gamry Instruments, Warminster, PA, USA). The Sauerbrey equation was used to estimate the amount of bound molecules per unit geometric area of a QCM gold substrate, which is analogous to the SPRi microarray gold surface and thus justifies the validation.[23, 24]

$$\Delta f = -\frac{2f_0^2}{A\sqrt{\mu\rho}}\Delta m$$

where Δf = frequency decrease due to mass change; f_o = fundamental oscillation frequency of the quartz crystal (10 MHz in our case); A = geometric area of Au-surface (0.2 cm^2); ρ = density of quartz (2.648 g cm^{-3}), μ = shear modulus of quartz (2.947 x 10^{11} dyn cm^{-2}), and Δm = mass change (g).

2.3 Results and Discussion

The three amino acid residues of p53 (so called "hot spots"), Phe19, Trp23, and Leu26, have been shown to offer the maximum binding energy for the interface formation between p53 and MDM2 binding domains.[25] Specificity of the MDM2-p53 interaction was investigated by examining a mutated p53 TAD peptide immobilized as a SAM on an SPRi microarray chip. To generate the mutant, the wild-type p53 TAD was mutated to alanine at the most destructive Phe19, Leu22, and Trp23 residues as reported in the literature[26] (mutated p53 TAD was custom prepared from Biomatik, Ontario, Canada). In the SPRi chip, eight gold array spots in the C1 and C2 columns were immobilized with the mutant p53 TAD peptide, and the remaining eight spots were immobilized with the wild-type p53 TAD peptide (see labels in Figure 3A). A blocking step was

conducted using mPEG-7 as described in the methods. MDM2 solutions (10 μM) then were passed over the wild-type and mutant p53 spots via a microfluidic flow channel. The mutant p53 TAD peptides were considered to be negative controls.

Figure 3A shows the raw difference image (difference between pre- and post-binding events), and Figure 3B is the corresponding 3D representation. Wild-type p53 exhibited 3.5-times greater reflectivity change (Δ%R) than the mutated p53 array spots (see Figures 3C and 3D) upon MDM2 binding in the real-time analysis. Mutations of the wild type p53 TAD at predetermined amino acids has been shown to diminish the binding conformation required for MDM2 binding due to energetically unfavorable interactions.[27] In agreement with this, the designed p53 peptide array chip and SPRi detection method exhibit excellent specificity for studying and identifying similar cancer PPIs.

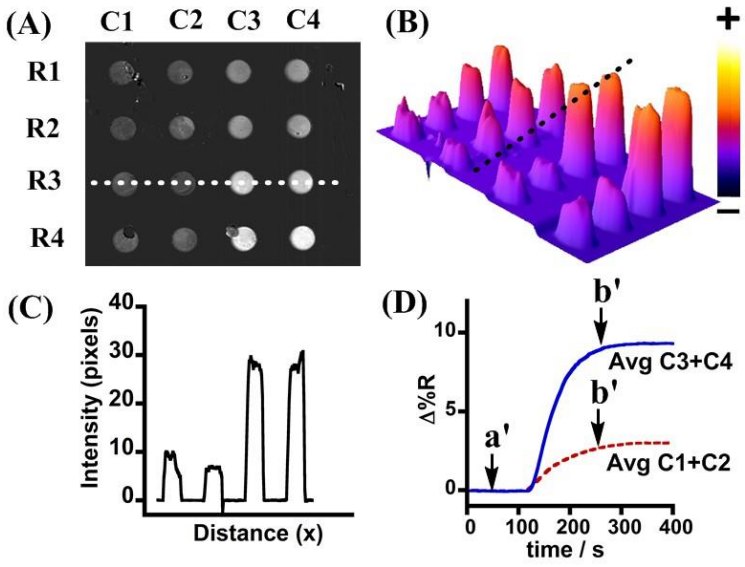

Figure 3. (A) SPR difference image, (B) 3D representation of the SPR difference image, (C) line profile of row 3 in A (R3), and (D) real-time average (Avg) responses from each of the eight-array spots for MDM2 binding (10 μM) to surface wild-type p53 peptide (C3 and C4 array spots) or mutated p53 (C1 and C2 array spots). MDM2 solution flow rate used was 50 μL min^{-1}. Label a': point of sample injection; label b': onset of rinse in buffer.

As another comparison, mutated p53 peptides were replaced with 1% bovine serum albumin (BSA, see Figure 4A, C1 and C2 array spots) and compared for the binding signals of MDM2 with wild-

type p53 TAD (see Figure 4A, C3 and C4 array spots). Significant signal enhancement was observed only for the MDM2-p53 interaction and not for the MDM2-surface BSA interaction, which further confirmed the specificity of the microarray approach (see Figures 4C and 4D). In addition, it was noted that such specific PPIs can be monitored even at a high MDM2 solution flow rate of 100 μL min^{-1}.

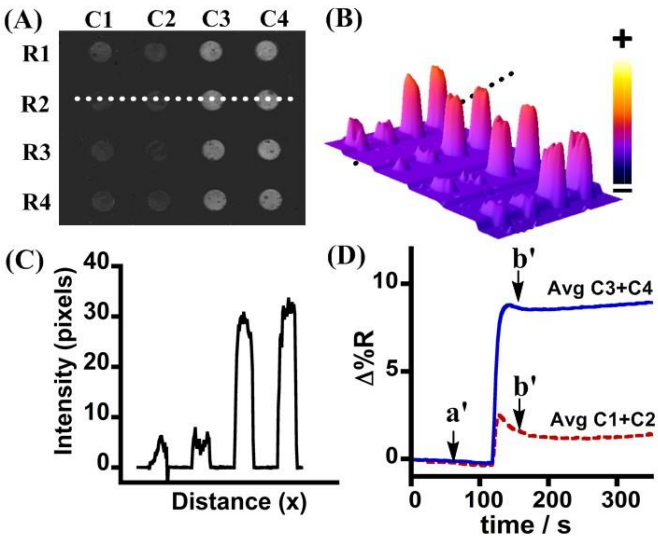

Figure 4. (A) SPR difference image, (B) 3D representation of the SPR difference image, (C) line profile of row 2 in A (R2), and (D) average of the real time sensograms of MDM2 binding (10 μM) to wild-type p53 array spots (C3 and C4 columns) or to BSA array spots (C1 and C2 columns). MDM2 solution flow rate used was 100 μL min^{-1}. Label a': point of sample injection; label b': onset of rinse in buffer.

Small peptides with Cys end groups have been shown to form highly dense SAMs.[28] Hence, it is feasible to attain high density SAMs of the immobilized p53 TADs in the designed microarray chips, and the thiol end group linkages can favorably orient the p53 peptide units to allow binding of significant amounts of MDM2 molecules. This should in turn offer good sensitivity of detection. In agreement with this, nM levels of MDM2 interaction with the surface p53 peptide SAM were easily detectable in the microarray (see Figure 5). The measured limit of detection (LOD) of MDM2 was 72 nM (LOD = $M_b + 3S_d$, where M_b is the mean and S_d is the standard deviation of Δ%R signal for 0 nM MDM2 solution).[29] This indicates that the designed microarray can also be used for

sensitive protein detection and by appropriate surface modification of the microarray, one may be able to further enhance the sensitivity and obtain even lower detection levels.

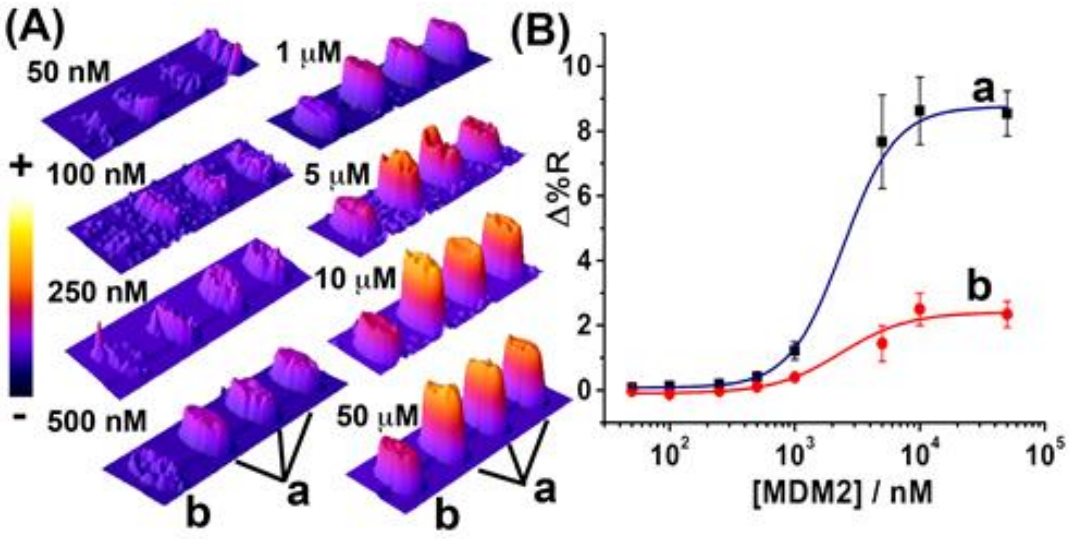

Figure 5. (A) 3D representations of the SPR difference images of 4 adjacent spots and (B) percentage reflectivity changes for the binding interactions related to varying concentrations of MDM2 with (a) wild and (b) mutated types of immobilized p53 TAD peptides.

Figure 5 shows the trend in responses for various nM to μM concentrations of MDM2 upon interaction with the surface immobilized wild-type p53 TAD peptide. Increments of pixel intensities of the SPR images are illustrated as 3D representations with increase in MDM2 concentrations (see Figure 5A). The percentage reflectivity increase resulting from the MDM2-p53 interaction was plotted against MDM2 concentrations, and the signals were saturated at 10 μM of

MDM2 (see Figure 5B). Real-time sensograms of each MDM2 concentration are provided in Figure 6.

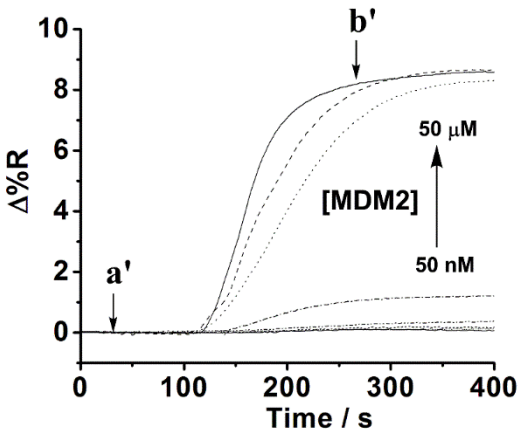

Figure 6. Real time percentage reflectivity changes for the binding interactions of varying concentrations of MDM2 to surface wild-type p53 TAD. MDM2 solution flow rate of 50 μL min^{-1} was used in this experiment. Label a': point of sample injection; label b': onset of rinse in buffer.

Possible high-density construction of the small p53 peptide SAM on gold surfaces of the SPRi microarray allowed detection of small concentrations of MDM2 with a relatively large dynamic range of up to 10 μM MDM2. Interaction between MDM2 and mutated p53 peptides was negligible at lower MDM2 concentrations, but it significantly increased at MDM2 concentrations > 1 μM, possibly due to non-specific interactions caused by high loading of MDM2 molecules (see Figure 5B-b). The objective of this study was to develop a simple and rapid SPRi-based strategy to identify potential cancer-causing PPIs and to convert this design into an efficient drug-screening platform. Therefore, relatively large flow rates of samples in the microfluidics (50 to 100 μL min–1) were used to obtain instant results, within a few minutes, without requiring any prolonged incubation or tedious procedures on the microarray.

The inhibition of the MDM2-p53 interaction was measured by Nutlin-3a, which is a pre-clinical small molecule drug developed by a group of scientists at Hoffmann-La Roche in Nutley, New Jersey.[13, 30] For the inhibition assay, different concentrations of Nutlin-3a pre-incubated with 1 μM MDM2 were passed over a SPRi chip fabricated with the wild type p53 (see Figure 7A).

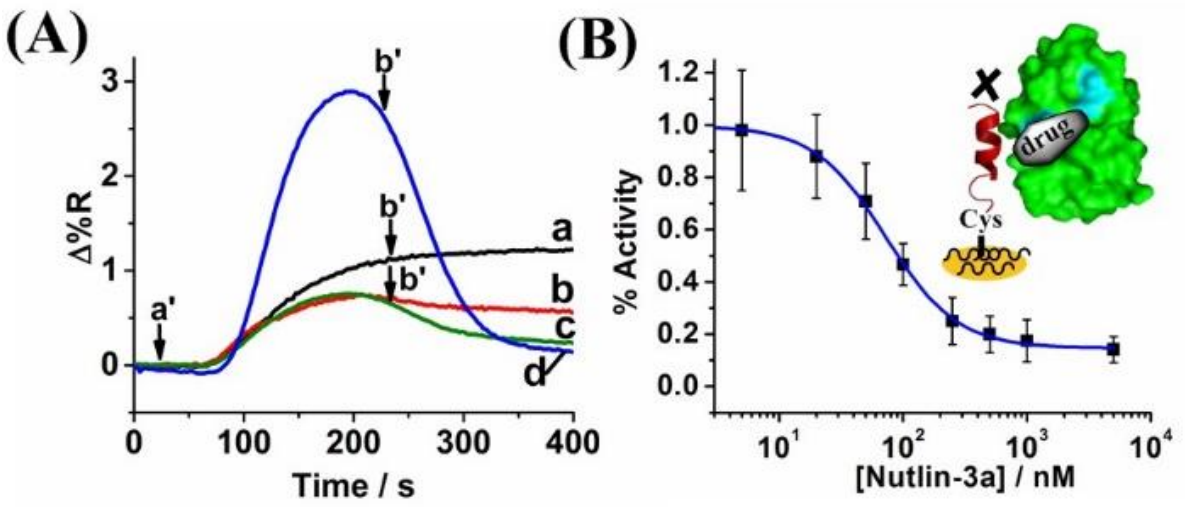

Figure 7. (A) Real-time percentage reflectivity changes for the binding interactions between wild-type p53 and (a) 0 nM, (b) 100 nM, (c) 500 nM, and (d) 5 μM Nutlin-3a treated with MDM2 (1 μM). (B) SPRi inhibition curve for the MDM2-p53 interaction. MDM2 solution flow rate of 50 μL min^{-1} was used in this experiment. Label a': point of sample injection; label b': onset of rinse in buffer.

As shown in Figure 7B, Nutlin-3a competed with the MDM2-p53 interaction in a dose-dependent manner. The measured half-inhibitory concentration of Nutlin-3a (IC_{50}) for the designed microarray method was 90 nM towards inhibiting the MDM2-p53 interaction. The measured IC_{50} value is in good agreement with those of reported studies.[13,15] A notable bulk effect was observed for higher concentrations of Nutlin-3a solution in DMF (albeit DMF was ≤ 0.3%, Figure 7A). The inhibition activity was determined by measuring the difference between the final plateau region and the initial baseline of the real time reflectivity curves (see Figure 7).

These results demonstrate that SPR imaging of the MDM2-p53 interaction is simple, offers good throughput, is sensitive for small molecule screening, and detecting any PPIs is feasible with good sensitivity and selectivity. In addition to developing an imaging-based SPR method for cancer PPIs and inhibition assays, it was shown that one can obtain apparent binding constants from the same sample, thus showing multiple advantages of using SPRi. Prior to imaging the binding or inhibition events on the arrays, real-time reflectivity changes upon MDM2 interaction (50 μL min^{-1} flow rate) were monitored with p53 and, a 1:1 bimolecular interaction kinetic model was used to calculate values for apparent association rate (k_a), dissociation rate (k_d), and binding constant (K_D).[31-33] The apparent values for k_a, k_d, and K_D were 342 (± 27) M^{-1} s^{-1}, 8.4 (± 0.8) × 10^{-5} s^{-1}, and 0.25 (± 0.03) μM, respectively.

The K_D provides an immediate understanding of the affinities between two interacting biomolecules. Reported NMR and isothermal calorimetric techniques showed K_D values in the range of 0.4–0.6 μM for the interaction between the N-terminal p53-interacting domain of MDM2 and p53 TAD.[25, 27, 34-36] Conventional SPR measurements for the interaction of full length p53 and p53 TAD peptide MDM2 yielded K_D values of 0.4 μM and 0.1–1.0 μM, respectively.[9, 15, 37] Thus, the observed K_D value of 0.25 μM is in reasonable agreement with prior reports based on bimolecular kinetics. Nonlinear regression analysis of the sigmoidal response, incorporating higher HDM2 concentrations to calculate K_D (concentration at half-maximal SPRi response in Figure 5B), gave a value of 2.16 (± 0.09) μM.[38-39] The disagreement of the measured K_D values between the two models is not surprising, as this could likely result from the limitation of applying a simple bimolecular model (based on linear least square analysis) at higher substrate concentrations due to factors that break boundary conditions (for e.g., cooperativity, heterogeneity).[40]

QCM experiments were carried out to validate the results obtained from the SPRi microarrays and to obtain quantitative information of immobilized p53 TADs, bound MDM2 molecules, and p53-

MDM2 inhibition by Nutlin-3a. Increased mass on the gold surface of a QCM resonator by immobilization of molecules on the surface causes a decrease in the oscillation frequency of the resonator according to the Sauerbrey equation.[23,41] The surface area-normalized apparent number of molecules bound to the gold surface of the resonator at each step of the assembly, including interaction and inhibition, was determined (see Table 1). It is to be noted that the calculated number of molecules are strictly apparent, because viscoelasticity properties and hydration of protein molecules are not accounted for in the estimation.[42,43] Based on the reported structural information,[25] the MDM2-p53 interaction occurs with a 1:1 stoichiometry, and it was estimated that approximately 56% of p53 TAD peptide molecules were in the appropriate orientation on the gold surface to interact with MDM2 molecules. The less than theoretically possible 100% interaction ratio could be due to the larger size of MDM2, which could cause sterically hindered access to the surrounding p53 peptide binding sites.

Table 1. QCM Estimation.

Assembly	-Δf / Hz	Apparent Number of molecules (x10^{12}) cm^{-2}
Au-p53	57 ± 5	80 ± 7
Au-p53/mPEG-7	129 ± 22	1010 ± 170
Au-p53/mPEG-7/MDM2	213 ± 24	45 ± 6
Au-p53/mPEG-7/MDM2+Nutlin-3a	131± 13	28 ± 3

For the MDM2 solution that was pre-incubated with Nutlin-3a, the decrease in oscillation frequency was smaller than that of the free MDM2 binding to surface p53 due to the drug-induced inhibition of the MDM2-p53 interaction. This effect is illustrated as a change in mass added to the quartz crystal in Figure 8. Mass estimations have shown that about 40% of initially-bound MDM2 molecules are inhibited by the drug treatment when tested for a saturating MDM2 level (10 μM, see Figure 8) at a high concentration of Nutlin-3a (170 μM). This indicates that the surface chemistry of p53 peptide immobilization via a cysteinyl thiol linkage onto gold is reasonably stable in terms of facilitating the MDM2-p53 interaction and monitoring of a small molecule caused inhibition on the SPRi chip. Furthermore, the QCM estimation on the gold surface is complementary to the SPRi analysis.

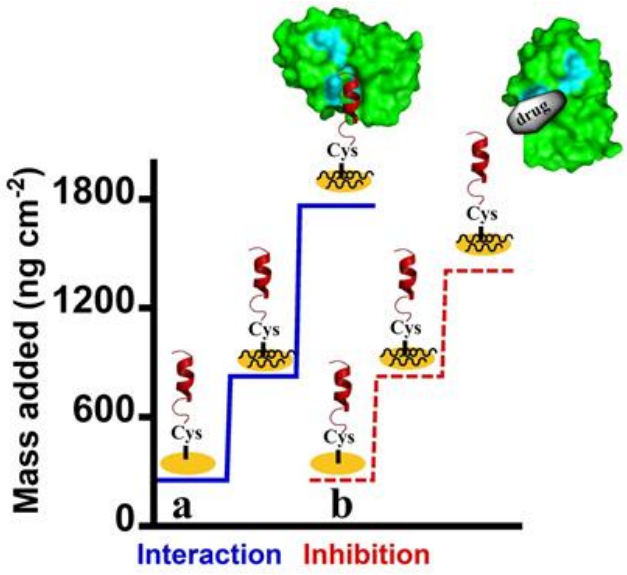

Figure 8. Mass increments due to the attachment of wild-type p53 TAD peptide, mPEG7 blocking step, and 10 µM MDM2 treated with (a) 0 and (b) 170 µM of Nutlin-3a determined by the QCM experiments.

2.4 Conclusions

In conclusion, the results presented above show that the SPRi technique can be used effectively to detect cancer PPIs and to study small molecule inhibition of PPIs in a label-free manner. Additionally, the real-time SPRi technique allows measurement of binding kinetics of biomolecular interactions related to PPIs in cancer or any other disease. Systematic screening of small molecule drug libraries using the SPRi microarray will aid in identification of the most efficient drug candidate to disrupt disease-promoting PPIs and in facilitating instant cancer drug discoveries. Moreover, this label-free *in vitro* array platform is fast, simple, robust, and offers high sensitivity with selectivity. The ability to use synthetic, small peptide binding domains of functional proteins in SPRi microarrays were demonstrated without conducting tedious whole protein purification techniques. The findings of this study represent a significant advancement in identification and characterization of biological interactions and applicability for targeted drug development.

2.5 References

1. Wells, J. A.; McClendon, C. L. *Nature* **2007**, *450*, 1001-1009.
2. White, A. W.; Westwell, A. D.; Brahemi, G. *Expert. Rev. Mol. Med.* **2008**, *10*, e8.
3. Ivanov, A. A.; Khuri, F. R.; Fu, H. *Trends Pharmacol. Sci*. **2013**, *34*, 393-400.
4. Zilfou, J. T.; Lowe, S. W. *Cold Spring Harb. Perspect. Biol.* **2009**, *1*, a001883.
5. Freedman, D. A.; Wu, L.; Levine, A. J. *Cell. Mol. Life Sci.* **1999**, *55*, 96-107.
6. Seefeld, T. H.; Halpern, A. R.; Corn, R. M. *J. Am. Chem. Soc.* **2012**, *134*, 12358-12361.
7. Fasoli, J. B.; Corn, R. M. *Langmuir* **2015**, *31*, 9527-9536.
8. Kim, M.; Park, K.; Jeong, E.-J.; Shin, Y.-B.; Chung, B. H. *Anal. Biochem.* **2006**, *351*, 298-304.
9. Domenici, F.; Frasconi, M.; Mazzei, F.; D'Orazi, G.; Bizzarri, A. R.; Cannistraro, S. *J. Mol. Recognit.* **2011**, *24*, 707-714.
10. Pillet, F.; Romera, C.; Trévisiol, E.; Bellon, S.; Teulade-Fichou, M.-P.; François, J.-M.; Pratviel, G.; Leberre, V. A. *Sensors and Actuators B: Chemical* **2011**, *157*, 304-309.
11. Chen, S.; Deng, T.; Wang, T.; Wang, J.; Li, X.; Li, Q.; Huang, G. *J. Biomed. Opt.* **2012**, *17*, 0150051-0150058.
12. Jung, S. O.; Ro, H.-S.; Kho, B. H.; Shin, Y.-B.; Kim, M. G.; Chung, B. H. *Proteomics* **2005**, *5*, 4427-4431.
13. Vassilev, L. T.; Vu, B. T.; Graves, B.; Carvajal, D.; Podlaski, F.; Filipovic, Z.; Kong, N.; Kammlott, U.; Lukacs, C.; Klein, C.; Fotouhi, N.; Liu, E. A. *Science* **2004**, *303*, 844-848.
14. Smith, J. M.; Frost, J. R.; Fasan, R. *Chem. Commun*. **2014**, *50*, 5027-5030.
15. Pazgier, M.; Liu, M.; Zou, G.; Yuan, W.; Li, C.; Li, C.; Li, J.; Monbo, J.; Zella, D.; Tarasov, S. G.; Lu, W. *Proc. Natl. Acad. Sci. U. S. A.* **2009**, *106*, 4665-4670.
16. Wong, C. L.; Olivo, M. *Plasmonics* **2014,** *9*, 809-824.
17. Kodoyianni, V. *Biotechniques* **2011**, *50*, 32-40

18. Shangary, S.; Wang, S. *Annu. Rev. Pharmacol. Toxicol.* **2009**, *49*, 223-241.

19. Dickens, M. P.; Fitzgerald, R.; Fischer, P. M. *Semin. Cancer. Biol.* **2010**, *20*, 10-18.

20. Haaland, I.; Opsahl, J.; Berven, F.; Reikvam, H.; Fredly, H.; Haugse, R.; Thiede, B.; McCormack, E.; Lain, S.; Bruserud, O.; Gjertsen, B. *Mol. Cancer* **2014**, *13*, 116.

21. Pal-Bhowmick, I.; Sadagopan, K.; Vora, H. K.; Sehgal, A.; Sharma, S.; Jarori, G. K. Eur. *J. Biochem.* **2004**, *271*, 4845-4854.

22. Schneider, C. A.; Rasband, W. S.; Eliceiri, K. W. *Nat Meth* **2012**, *9*, 671-675.

23. Sauerbrey, G. Z. Z. *Phys*. **1959**, *155*, 206-222.

24. Patolsky, F.; Zayats, M.; Katz, E.; Willner, I. *Analytical Chemistry* **1999**, *71*, 3171-3180.

25. Kussie, P. H.; Gorina, S.; Marechal, V.; Elenbaas, B.; Moreau, J.; Levine, A. J.; Pavletich, N. P. *Science* **1996**, *274*, 948-953.

26. Picksley, S. M.; Vojtesek, B.; Sparks, A.; Lane, D. P. *Oncogene* **1994**, *9*, 2523-2529.

27. Shan, B.; Li, D.-W.; Brüschweiler-Li, L.; Brüschweiler, R. *J. Biol. Chem*. **2012**, *287*, 30376-30384.

28. Nowinski, A. K.; Sun, F.; White, A. D.; Keefe, A. J.; Jiang, S. *J. Am. Chem. Soc.* **2012**, *134*, 6000-6005

29. Long, G. L.; Winefordner, J. D. *Anal. Chem.* **1983**, 55, 712A-724A.

30. Vassilev, L. T. *J. Med. Chem.* **2005**, *48*, 4491-4499.

31. Oshannessy, D. J.; Brighamburke, M.; Soneson, K. K.; Hensley, P.; Brooks, I. *Anal. Biochem*. **1993**, *212*, 457-468.

32. Wegner, G. J.; Wark, A. W.; Lee, H. J.; Codner, E.; Saeki, T.; Fang, S.; Corn, R. M. *Anal. Chem.* **2004**, *76*, 5677-5684.

33. Katsamba, P. S.; Navratilova, I.; Calderon-Cacia, M.; Fan, L.; Thornton, K.; Zhu, M.; Bos, T. V.; Forte, C.; Friend, D.; Laird-Offringa, I.; Tavares, G.; Whatley, J.; Shi, E.; Widom, A.;

Lindquist, K. C.; Klakamp, S.; Drake, A.; Bohmann, D.; Roell, M.; Rose, L.; Dorocke, J.; Roth, B.; Luginbühl, B.; Myszka, D. G. *Anal. Biochem.* **2006**, *352*, 208-221.

34. Schon, O.; Friedler, A.; Bycroft, M.; Freund, S. M. V.; Fersht, A. R. *J. Mol. Biol.* **2002**, *323*, 491-501
35. Teufel, D. P.; Freund, S. M.; Bycroft, M.; Fersht, A. R. *Proc. Natl. Acad. Sci. U. S. A.* **2007**, *104*, 700
36. Lai, Z.; Auger, K. R.; Manubay, C. M.; Copeland, R. A. Arch. *Biochem. Biophys.* **2000**, *381*, 278-28
37. Chi, S.-W.; Lee, S.-H.; Kim, D.-H.; Ahn, M.-J.; Kim, J.-S.; Woo, J.-Y.; Torizawa, T.; Kainosho, M.; Han, K.-H. *J. Biol. Chem.* **2005**, *280*, 38795-38802.
38. Copeland, R. A. Enzymes: a practical introduction to structure, mechanism, and data analysis, Second ed.; John Wiley & Sons: New York, 2000.
39. Santos-Carballal, B.; Aaldering, L.; Ritzefeld, M.; Pereira, S.; Sewald, N.; Moerschbacher, B.; Götte, M.; Goycoolea, F. *Scientific reports* **2015**, 5, 13567.
40. O'Shannessy, D. J.; Winzor, D. J. *Anal. Biochem.* **1996**, *236*, 275-283.
41. Singh, V.; Krishnan, S. *Analyst* **2014**, *139*, 724-728.
42. Vörös, J. *Biophys. J*. **2004**, 87, 553-561.
43. Carton, I.; Brisson, A. R.; Richter, R. P. *Anal. Chem*. **2010**, 82, 9275-9281.

CHAPTER 3

A SIMPLE CONSTRUCTION OF ELECTROCHEMICAL LIVER MICROSOMAL BIOREACTOR FOR RAPID DRUG METABOLISM AND INHIBITION ASSAYS

3.1 Introduction

A simple construction of bioactive interfaces of human liver fractions with electrodes, which has the potential to transform the current paradigm of drug development by providing rapid screening platforms for drug metabolism and inhibition, was demonstrated in this study. Human cytochrome P450s (CYPs) are the major drug metabolizing enzymes present in the liver. The remarkable and broad catalytic properties of CYPs suggest that they may prove useful in the stereoselective green syntheses of fine chemicals.[1,2] The *in vivo* catalytic activities of CYPs primarily depend on the electrons supplied by cytochrome P450-reductase (CPR) with NADPH acting as the electron source.[3] The significance of the CYP-CPR interaction in altering CYP enzyme-turnover has been examined in several biochemical and electrochemical studies.[4-7] CPR contains both flavin adenine dinucleotide (FAD) and flavin mononucleotide (FMN) cofactors and is the only known membrane-bound flavoproteins. CPR transfers electrons from NADPH via FAD to FMN and further to the heme centers of CYPs. In this electron transfer (ET)-pathway, phospholipd bilayers play a crucial role in modulating the redox potentials of FMN and FAD in CPR and aid in ET.[8]

In direct electrochemistry, the electrode acts as an electron donor to redox protein films under an applied negative potential.[9-11] Because purification of CYPs is a tedious process, the application of liver microsomes or genetically engineered supersomes (microsomes specifically enriched with a CYP enzyme and its reductase) containing CYPs in the development of new biosensing and electrocatalytic systems is an emerging research area.[7] Human liver microsomes (HLM) are obtained by homogenizing liver tissue in buffer and centrifuging the resulting slurry at 10000 x g to specifically isolate the major membrane-bound drug metabolizing enzymes such as CYP enzymes and their redox partner protein, CPR. HLM are extensively used in pharmaceutical industries for *in vitro* drug metabolism and inhibition assays and for evaluating ADME (Absorption, Distribution, Metabolism and Excretion) properties of any drug in development.[12] Direct ET and catalytic studies of genetically engineered microsomes,[13] rat liver microsomes,[14] and HLM[15] assembled as films with polyions, microsomes coated on different thiolated hydrophobic gold electrodes,[16] and layer-by-layer films of purified human CYPs and microsomal CPR[17] have been conducted.

Carbon electrodes are known for their robustness, inexpensive nature, ease of cleaning, and reusability. The objective of this study is to develop a suitable carbon electrode platform that will allow immobilization of complex HLM by direct adsorption with stability and bioactivity. Such analytical platform is expected to offer a novel, rapid design of HLM electrodes for drug metabolism assays involving simple and cost-effective electrochemical approach. In this study, four commonly used carbon electrodes were chosen, including basal-plane pyrolytic graphite (BPG), edge-plane pyrolytic graphite (EPG), glassy carbon (GC), and high purity graphite (HPG).

Considering the importance of HLM in pharmaceutical drug development and toxicology fields, the demonstration of a rapid, stable, and one-step microsomal bioreactor design for inexpensive electrochemical drug metabolism and inhibition assays is novel and highly significant. Additionally, the insights on the carbon electrode-dependent direct electrochemical and electrocatalytic properties of adsorbed HLM were demonstrated.

3.2 Experimental

3.2.1 Materials and Reagents

HLM (total protein 20 mg mL^{-1}, total CYPs 0.5 nmol mg^{-1} protein, NADPH-cyt c reductase activity 154 nmol mg^{-1} protein min^{-1} that corresponds to 0.051 nmol CPR mg^{-1} protein,[18] and cytochrome b_5 0.34 nmol mg^{-1} protein) were purchased from XenoTech (Lenexa, KS, USA) and used as received. Disk electrodes of EPG, BPG, HPG, and GC were used in this study [geometric area 0.2 cm^2]. Pure EPG and BPG disks were constructed from PG-blocks (1 x 1 x 0.5 inches, Momentive Performance Materials, Albany, NY, USA). Basal planes are present parallel to the PG surface and edge planes are aligned perpendicular to the surface.[19] HPG disks were purchased from McMaster-Carr (POCO EDM-4 grade, Atlanta, GA, USA) and GC electrodes were obtained from CH Instruments (Austin, TX, USA). Testosterone, ketoconazole, and standard 6β-hydroxytestosterone were purchased from Sigma-Aldrich. All other reagents were high purity analytical grade. Unless otherwise specified, all electrochemical measurements were carried out in phosphate buffer containing 0.15 M NaCl, pH 7.0 at 25 °C.

3.2.2 Microsomal Film Preparation

Prior to use, all electrodes were polished and cleaned by following standard procedures to obtain fresh surfaces for adsorbing HLM. Briefly, BPG, EPG, and HPG disk electrodes were freshly polished using SiC paper (P320 grit), and GC electrodes were polished in an aqueous slurry of alumina (1 micron) placed on an alumina-pad (EXTEC Corp., Enfield, CT, USA) to obtain fresh surfaces. The polished electrodes were cleaned by ultrasonication in water for 1 min and then dried under nitrogen. A film of HLM was formed on each freshly polished electrode by adsorption from a 10 μL solution of HLM for 20 min at 4 ºC. The electrodes were rinsed with buffer to remove weakly and unbound HLM and then used for cyclic voltammetry (CV) studies.

3.2.3 Colorimetric Assay for Presence of Microsomal Films on Electrodes

The presence of phospholipids in the microsomal films immobilized on various electrode surfaces was confirmed using a colorimetric assay. The major microsomal phospholipids, such as sphingomyelin, phosphatidyl serine, phosphatidyl ethanolamine, and lecithin, are the active components that form a red color complex with ammonium ferrothiocyanate that absorbs at ~488 nm in chloroform as a solvent.[20]

3.2.4 Fourier Transform Infrared (FTIR) Spectroscopy

The liver microsomal films on the electrodes were characterized by FTIR spectroscopy (Nicolet IS50 FTIR, Thermo Scientific) in the attenuated total reflectance mode (ATR). The electrodes were mounted on an ATR diamond crystal and 64 scans were acquired and averaged to obtain a good signal-to-noise ratio. Similarly, the FTIR spectrum of HLM dry coated directly on an ATR diamond crystal was obtained for comparison.

3.2.5 Microscopic Characterization of the Electrodes

The surface morphologies of BPG, EPG, GC, and HPG disk electrodes before and after coating with a layer of HLM were characterized by scanning electron microscopy (SEM, Model: FEI Quanta 600FE). An accelerating voltage of 20 kV was applied. The images were acquired using the FEI xT Microscope Control Software.

3.2.6 Thickness of HLM Film on Different Electrodes

The dry film thicknesses of adsorbed microsomal films on BPG, EPG, GC, and HPG disk electrodes were measured by a spectral reflectance method using a Filmetrics F40 system (Fairport, NY, USA). Different locations along the microsomal films were scanned to obtain a range of thicknesses representative of the entire surface of each electrode. For each location, the thickness was calculated from the reflectance spectrum obtained at a normal incidence in the visible wavelength region. The refractive index of HLM was assumed to be 1.54 at 632.8 nm.[21] The experiment was repeated with three replicate samples of microsomal films for each type of electrode.

3.2.7 XPS Analysis

X-ray photoelectron spectroscopy (XPS) measurements were performed using the Mg anode of a PHI 300 W twin anode X-ray source and the PHI double-pass cylindrical mirror analyzer as the detector with pass energy of 100 eV. The instrument comprised a surface analysis system with a base pressure of 2×10^{-10} Torr. General survey scans were carried out for polished GC, EPG, BPG, and HPG electrodes. Percentage amounts of C and O were calculated for comparison among electrodes.

3.2.8 Electrochemical Measurements

A CH instrument 6017E electrochemical analyzer was used for CV experiments. Measurements were made in a standard 3-electrode cell consisting of an Ag/AgCl reference electrode (1 M KCl, CH Instruments), a Pt-wire counter electrode, and a HLM-coated working electrode disk (BPG, EPG, GC, or HPG). A 90% IR compensation was employed before starting the CV scans. For anaerobic CV experiments, the cell buffer was purged under high purity nitrogen for 30 min before acquiring voltammograms, and a constant nitrogen atmosphere was maintained during measurements.

3.2.9 Electrocatalytic Oxygen Reduction

Oxygen plays an important role in CYP enzyme-catalyzed reactions by aiding in the formation of the reactive CYP-ferryloxy radical cation [$^{+\bullet}$(CYP-Fe^{IV}=O)].[3] This oxoform is presumed to be the active oxidant of CYPs that can oxygenate a bound drug molecule or other compounds.[3,4] Oxygen binding to CYPs requires the initial reduction of the heme-cofactor of CYPs by CPR involving an *in vivo* electron donor (e.g., NADPH)[4] or it can be driven *in vitro* via the electrode by an applied potential. The HLM catalyzed oxygen reduction was studied in stirred buffer solutions to achieve mass transfer by convection,[22] which provided better film stability than a rotating disk set-up. Defined percentages of oxygen were mixed with nitrogen using two mass flow controllers (Aalborg Instruments & Controls Inc., NY, USA) and supplied to the film of HLM on each electrode. The percentage O_2 was converted to the corresponding concentration using the Henry's law equation.[23,24]

3.2.10 Electrocatalytic Testosterone Hydroxylation and Liquid Chromatography Detection of Products

The electrocatalytic conversion of testosterone to 6β-hydroxytestosterone by the designed microsomal films was confirmed by liquid chromatography.[16, 17] In brief, the electrodes adsorbed with HLM were placed in a stirred, 3-electrode microcell containing 250 μM testosterone in 1 mL of potassium phosphate buffer, pH 7.0. The electrolysis was carried out at an applied potential of –0.6 V vs. Ag/AgCl for 1 h under a constant supply of oxygen. The reaction mixture was analyzed by high performance liquid chromatography (HPLC, C-18 Column, Shimadzu LCMS-2010EV). The product was identified using standard 6β-hydroxytestosterone (Sigma). For inhibition studies, 100 μM ketoconazole was added to 250 μM testosterone in pH 7.0 buffer, electrolysis was carried out, and the reaction mixture was analyzed by HPLC. A gradient elution involving acetonitrile/water solvent mixture was used in HPLC analysis: 10% acetonitrile for 0–10 min followed by 10–50% acetonitrile up to 60 min and a constant 50% acetonitrile until 80 min at a flow rate of 0.3 mL min^{-1}.

3.3 Results and Discussion

3.3.1 Spectral, Spectroscopic, and Microscopic Characterization of Films of HLM on Electrodes

The formation of a red colored complex in the reaction of HLM with ammonium ferrothiocyanate (λ_{max} at 488 nm)[20] confirmed the presence of microsomal phospholipids in the adsorbed microsomal films (Figure 1A). FTIR characterization of HLM on the various electrodes showed the presence of the amide I and amide II bands of microsomal proteins at 1650 and 1542 cm^{-1}, respectively (see Figure 1B). Additionally, the fundamental bond stretching frequencies of phospholipids in the vibrational region 1300–900 cm^{-1} were identified by the FTIR characterization.[20,25,26] The characteristic phospholipid vibrational bands were noted at 1237 (P=O), 1045 (P-O), 990 (P-O-C), and 924 cm^{-1} (C-N of choline group) for microsomal films coated on the electrodes (see Figure 1B). Similar vibrational bands were also noted for the HLM film coated directly on an FTIR-ATR crystal (see Figure 1B), confirming that the electrodes did not induce any notable change in the phospholipid structures of adsorbed HLM.

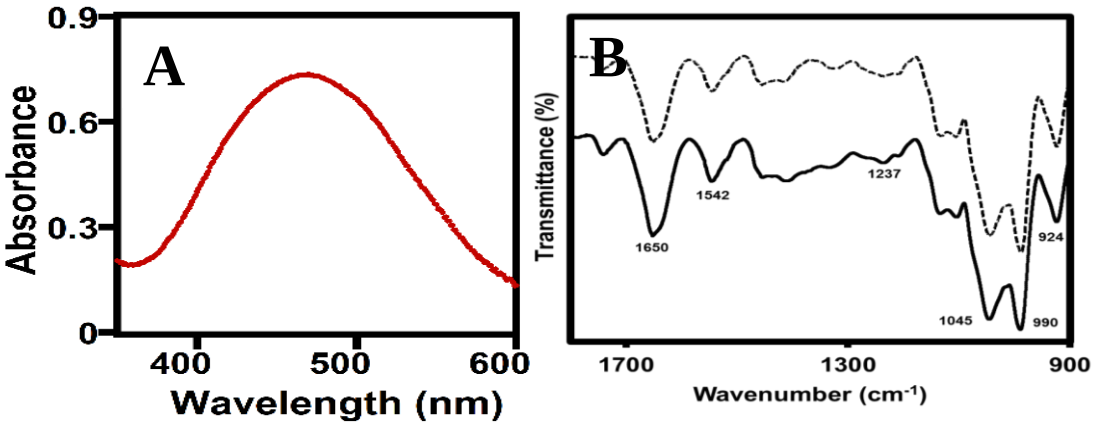

Figure 1. (A) Representative absorbance spectrum of HLM extracted in chloroform from a BPG/HLM electrode and (B) Representative infrared spectrum of HLM adsorbed on an ATR diamond crystal (dotted line) or on a BPG electrode (solid line).

The scanning electron micrographs of polished GC, HPG, EPG, and BPG disk electrodes, and those adsorbed with a layer of HLM are shown in Figure 2 (A-H). The GC surface is relatively smooth, whereas the EPG surface features large surface defects. The BPG surface displayed relatively less surface defects,[19] and the HPG surface exhibited platelet-like surface defects that differ from pure edge and basal planes (see Figure 2 A-D, respectively). All observed surface morphologies of polished electrodes are in good agreement with results of prior studies.[27-30] Adsorption of a layer of HLM on each electrode changed the surface morphology and produced coated film textures, which confirmed the formation of microsomal films on the electrodes (see Figures 2 E-H).

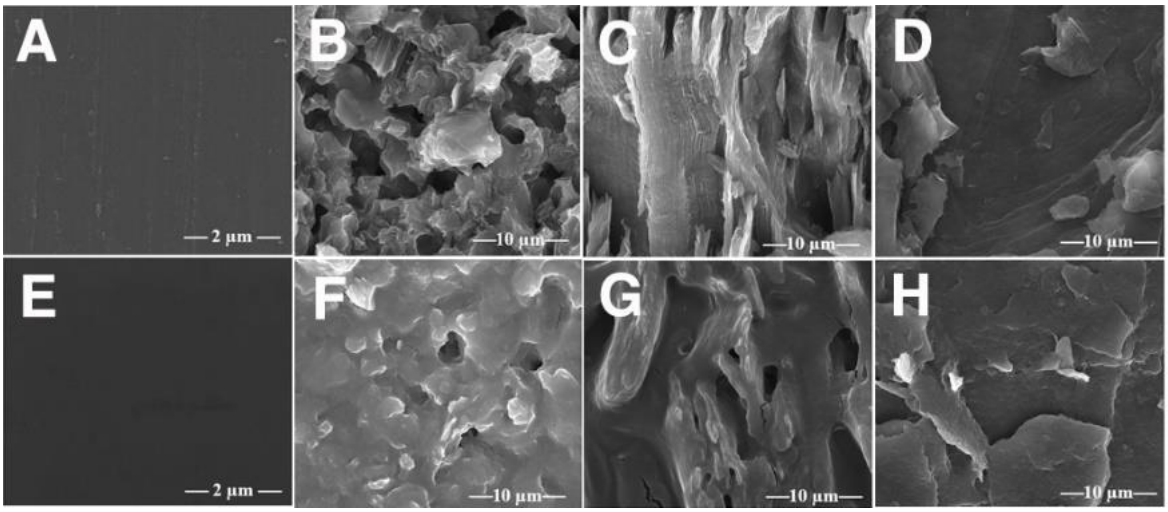

Figure 2. SEM images of polished (A) GC, (B) HPG, (C) EPG, and (D) BPG electrodes and these electrodes after being coated with a layer of HLM: (E) GC/HLM, (F) HPG/HLM, (G) EPG/HLM, and (H) BPG/HLM.

3.3.2 Electrochemical Probing of Microsomal Film Voltammetry

To drive electrocatalysis of a drug conversion into metabolites, it is necessary that electrons are successfully delivered from the electrode to reduce the immobilized liver microsomal proteins. It was examined by utilizing cyclic voltammetry to study the direct electron transfer properties of designed microsomal films on various carbon electrodes. Figure 3 A shows the background subtracted cyclic voltammograms of microsomal films adsorbed on the carbon electrodes in a nitrogen atmosphere at pH 7.0. Polished electrodes with an adsorbed phospholipid film (L-α-phosphatidylchloine) in the absence of microsomal proteins did not show any redox peaks (see Figure 3B), and thus confirmed that the direct electron transfer from the electrode to microsomal proteins was achieved (see Figure 3A). The peak separation between oxidation and reduction potentials with the logarithm of scan rate is shown in Figure 3C for the microsomal films on each electrode.

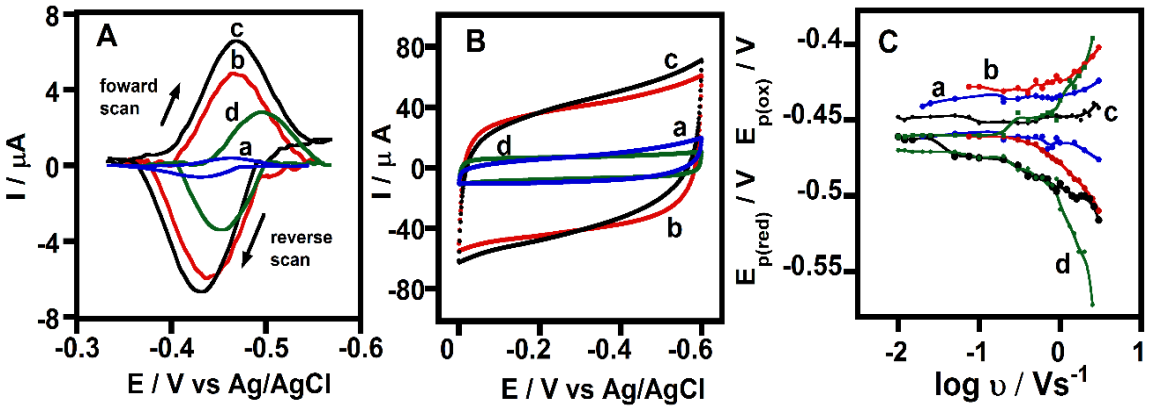

Figure 3. (A) Background subtracted cyclic voltammograms of liver microsomal films physisorbed on (a) GC, (b) HPG, (c) EPG, and (d) BPG electrodes at 0.7 V s^{-1} in anaerobic phosphate buffer, nitrogen atmosphere, pH 7.0, 25 °C. (B) The corresponding cyclic voltammograms (a-d) of control phosphatidylchloine films adsorbed similarly on the various electrodes. (C) Trumpet plots displaying the reduction and oxidation peak potentials of HLM films with logarithm of scan rate on (a) GC, (b) HPG, (c) EPG, and (d) BPG electrodes in anaerobic phosphate buffer, pH 7.0, 0.15 M NaCl, 25 °C.

The average formal potential ($E^{o'}$) of microsomal films was in the range of –0.45 to –0.47 V vs Ag/AgCl. The observed $E^{o'}$ values are in good agreement with prior reports on the formal potential of microsomal CPR protein.[14,15,17,31,32] On the other hand, purified CYPs (–0.3 to –0.33 V vs Ag/AgCl),[33] microsomal cyt b_5,[34] and only CYP-containing microsomes (–0.38 V vs Ag/AgCl)[16] are known to exhibit more positive formal potentials. Furthermore, the anaerobic peak potentials of microsomal films in nitrogen did not shift positive upon supplying carbon monoxide (see Figure 4), which is against the characteristic feature of microsomal CYP enzymes.[33] This suggests that the observed voltammetric properties of microsomal films are characteristics of oxidoreductases in microsomes.[13-15]

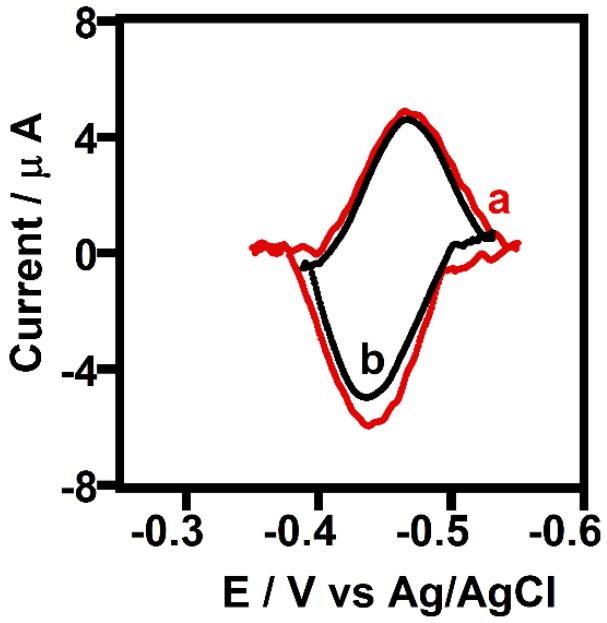

Figure 4. Background subtracted cyclic voltammograms of HPG/HLM films **a.** in N_2 and **b.** after bubbling CO for 15 min, scan rate 0.5 V s^{-1}, pH 7.0 buffer, 0.15 M NaCl, 25 ^{o}C.

The peak currents increased linearly with scan rates from 0.005 to 2 Vs^{-1} for the immobilized microsomal films on all four carbon electrodes (see Figure 5). This property confirms the surface-confined redox voltammetry of HLM. The ratio between the reduction and oxidation peak currents was close to unity.

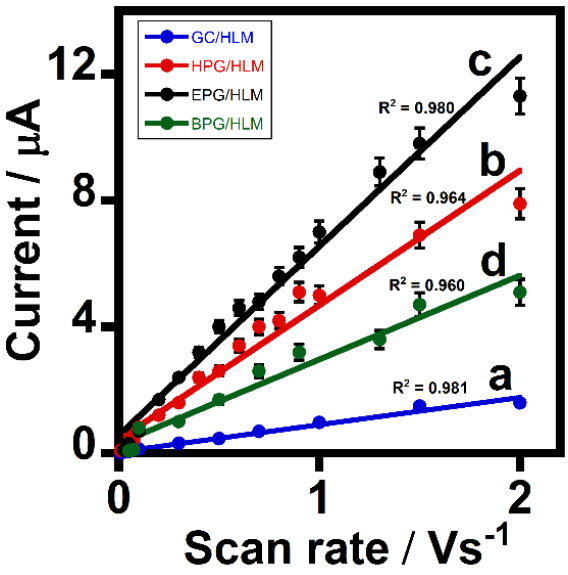

Figure 5. Peak current vs scan rate for the adsorbed microsomal films on (a) GC, (b) HPG, (c) EPG, and (d) BPG electrodes in anaerobic phosphate buffer, nitrogen atmosphere, pH 7.0, 25 °C.

Integration of the peak area provided the charge (Q) in coulombs (see Table 1).[22] The formal potentials of HLM physisorbed on BPG, EPG, GC, and HPG electrodes did not change significantly. However, the electroactive amounts (proportional to the measured charge) of microsomal films among the surface defective EPG and HPG electrodes were comparable to each other, and about 10-times greater than the smooth GC electrode and about 1.5-times greater than the moderately defective BPG electrode (see Table 1).

The positive shifts in formal potentials with decreasing pH suggest the occurrence of proton-coupled ET processes (involving equal numbers of electrons and protons, see Table 1) in the microsomal films on different carbon electrodes. The average shifts in formal potentials per pH unit (tested pH conditions: pH 5.5, 6.5, and 7.5) was close to the Nernstian 59 mV pH^{-1} for the

HPG/HLM and EPG/HLM films and higher than 59 mV for the GC/HLM and BPG/HLM films (see Table 1)[14]. The peak width at half maximum (PWHM) was in the range of 63-82 mV for all microsomal films (see Table 1). This range is between the ideal 90.6 and 45.3 mV for one electron and two electron processes, respectively.[22]

Table 1. Electrochemical parameters of liver microsomal films adsorbed on different carbon electrode materials under nitrogen atmosphere.

Film Type	$E^{o'}$ / V vs Ag/AgCl	Q / nC	PWHM / mV	$\Delta E^{o'}$ / pH mV	k_s (s^{-1})
GC/HLM	0.45 (± 0.01)	33 ± 2	63 ± 4	72 ± 6	91 ± 11
HPG/HLM	0. 45 (± 0.005)	330 ± 58	68 ± 2	64 ± 5	61 ± 4
EPG/HLM	0.45 (± 0.01)	347 ± 20	82 ± 2	57 ± 6	36 ± 4
BPG/HLM	0.47 (± 0.005)	232 ± 20	74 ± 4	75 ± 8	29 ± 5

Prior studies showed that FAD can accept up to two electrons from NADPH, whereas FMN acts as a one electron carrier to reduce CYPs in the biocatalytic pathway.[3,4,35] The observed lower PWHM values of liver microsomal films are similar to that reported for rat liver microsomes in layer-by-layer films with polyions (~ –0.45 V vs Ag/AgCl, pH 7.0, PWHM 70 ± 8 mV).[14] For purified human CPR in surfactant films (~ – 0.47 V vs Ag/AgCl, pH 8.0) that exhibited a PWHM of 70 mV, a multi-electron transfer process was inferred.[31] Based on our results and the reported literature, the possibility for a one electron process or a mixed one and two electron transfer processes taking place in the direct electrochemistry of the designed microsomal films can be suggested. Overall,

the examined electrochemical properties infer the non-ideal surface voltammetry of liver microsomal proteins.

3.3.4 Electrode-dependent Electron Transfer Kinetics

From the increase in peak separation with scan rates (see Figure 3C) that was subtracted for the non-zero constant peak separation at low scan rates (≤ 100 mVs^{-1}), similar to other reported studies,[33,36-38] the direct ET rate constants (k_s, s^{-1})[39] of microsomal films on the BPG, EPG, GC, and HPG disk electrodes were determined (see Table 1). The resulting fit of peak separation with the Butler-Volmer surface voltammetry showed good agreement (Figure 6).[33,38,39]

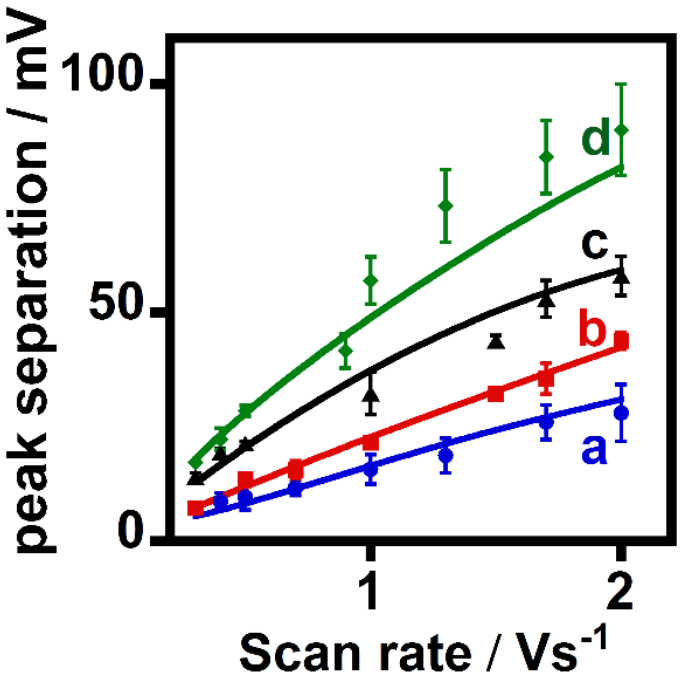

Figure 6. Experimental peak separation (corrected for the non-kinetic constant residual peak at low scan rates) with increasing scan rates for HLM films adsorbed on (a) GC (●), (b) HPG (■), (c) EPG (▲), and (d) BPG (♦) electrodes and the theoretical lines obtained by Butler-Volmer surface-voltammetry for the experimentally determined average rate constants (k_s, Table 1) and α = 0.5.

The direct ET rate of the microsomal film on the smooth GC electrode was 2.5–3.0 times greater than that of the microsomal films on the BPG and EPG electrodes and 1.5-times greater than that of the microsomal film on the HPG electrode (see Table 1). The magnitudes of electroactive

coverage and ET rates suggest that electrode roughness and surface defects favor enhanced amounts of electroactive microsomal proteins (e.g., HPG and EPG), while flat and surface defect-free GC surface seems to allow HLM molecules to orient in a uniform manner with a net fast ET rate (see Figure 2, SEM images). Figure 3C shows that the greater peak separation of microsomal films in the respective electrodes with increasing scan rates correlates inversely with the determined rates of direct ET (see Table 1), as per the Butler-Volmer surface voltammetry.[39]

3.3.5 Film Thickness and Electrochemical Kinetics

Spectral reflectance measurements illustrated that the nominal range of dry film thicknesses of microsomal films on the defective EPG and HPG electrodes was greater than that of the smooth GC and less defective BPG electrodes as presented in Table 2. The upper limits of dry film thicknesses of HLM among electrodes qualitatively correlated with the measured extent of electroactive amounts (see Table 1). In contrast, significant differences were observed in the kinetics of ET and film stability among the microsomal films on the different electrodes. For example, GC/HLM and BPG/HLM films of similar thicknesses displayed the highest and lowest direct ET rates, respectively. A similar feature is also reflected in the k_s values among the EPG/HLM and HPG/HLM electrodes (see Tables 1 and 2).

Table 2. Thickness data of the immobilized microsomal films on different electrodes.

Film Type	Dry Film Thickness (μm)
GC/HLM	0.3–1.3
HPG/HLM	5.0–10.0
EPG/HLM	2.0–8.5
BPG/HLM	0.2–3.0

The absence of correlation between film thickness and ET kinetics suggests the need to consider electrode factors such as surface defects, roughness, geometry, and chemical groups that can influence the secondary interactions between the electrode and the phospholipid membranes of HLM (see Figure 1 and further discussion below on XPS analysis). These factors in turn can alter the orientations of membrane-bound oxidoreductases and metabolic enzymes with respect to electrode. Hence, the pathway of ET between electrode and membrane-bound microsomal proteins appears to be the underlying factor in controlling electrochemical kinetics.

3.3.6 Surface Properties and Connection to Electrochemical Rates

The surface characteristics of polished electrodes were determined by XPS analysis as shown in Figure 7. Results indicate that the GC surface contains the highest oxygen content and the BPG surface has the lowest oxygen content and the reverse was observed with regard to carbon levels. EPG and HPG surfaces consist of intermediate oxygen levels, and carbon content close to the BPG

(see Table 3). The determined percentage values of C and O composition are in agreement with the reported literature on polished graphite and glassy carbon surfaces.[40-43]

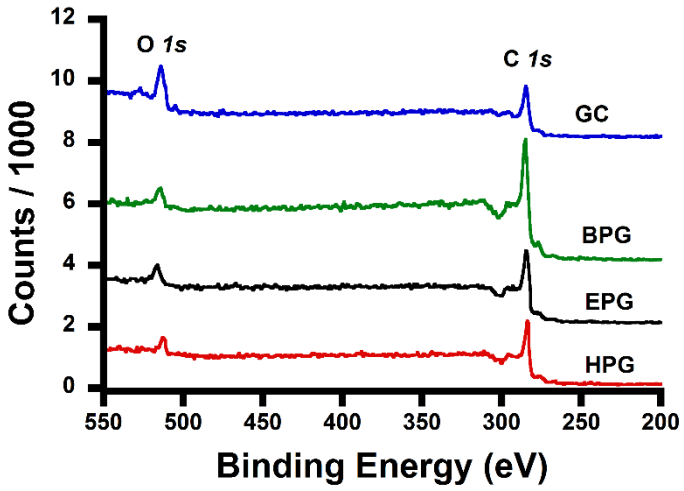

Figure 7. XPS spectra of polished electrode surfaces.

Surface oxygen density can be related to the extent of polarity and the surface carbon levels to the extent of hydrophobicity. The flat/smooth surface (see Figures 2A) of GC is ascribed to enable uniform HLM layer arrangement (with homogeneous protein orientation) and highly polar nature (see Table 3) is attributed to favor faster charge transfer kinetics in a relatively thinner film of HLM on GC over other electrodes. On the other hand, less polar nature of BPG with irregular surface appears to have varying interactions with the phospholipid membranes of HLM and cause mixed orientations of microsomal proteins in film, resulting in slower ET rates. HPG and EPG electrodes with intermediate levels of oxygen functionalities with respect to BPG and GC, and with extensive surface defects showed ET rate constants falling between that of BPG and GC.

Table 3. Carbon and oxygen levels of four carbon electrodes.

Electrode	Carbon	Oxygen
GC	77%	23%
HPG	91%	9%
EPG	89%	11%
BPG	94%	6%

Taken together, this study found that surface oxygen density of a carbon electrode influences charge transports in the phospholipid membranes of immobilized HLM. It is important to note that the determined electron transfer rate constants determined are representative of the whole film of HLM on a given electrode and are not controlled by one specific electrode property due to the complexity of interactions between an electrode and HLM as against a simple purified protein system.

3.3.7 Electroactive Microsomal Film Stability on Electrodes

The electroactive stability of microsomal films on BPG, EPG, GC, and HPG electrodes was monitored by cycling the potential continuously between 0 and –0.6 V vs Ag/AgCl for 200 cycles (scan rate 0.1 Vs^{-1}) in anaerobic pH 7.0 buffer. The GC/HLM film retained ~30% of initial current, the HPG/HLM and EPG/HLM films retained about 85% of the initial currents, and the BPG/HLM film retained about ~50% of the initial current. This level of electroactive HLM stability after 200 cycles on the HPG and EPG electrodes is likely satisfactory for electrocatalytic and biosensing applications.

3.3.8 Electrochemical O_2 Binding Kinetics to HLM

Oxygen is required in CYP-catalyzed monooxygenase activity to form the active CYP-heme oxidant, which can subsequently transfer the reactive oxygen to oxidize a bound substrate.[4,18] For oxygen to bind CYPs, the Fe^{III}-heme of CYP needs to be reduced first to the Fe^{II}-heme-CYP form (a one e^- reduction). Figure 8 (see solid curve in red) shows the catalytic cyclic voltammograms of oxygen reduction currents by microsomal films on the various carbon electrodes. The relative magnitudes of oxygen reduction currents among the designed microsomal films were in the following order: HPG/HLM ≈ EPG/HLM > GC/HLM > BPG/HLM.

The cyclic voltammograms of polished bare electrodes or those adsorbed with a phospholipid layer in the absence of immobilized microsomes did not show the characteristic enzyme-mediated electrocatalytic oxygen reduction (see Figure 8, broken curves), but rather displayed small reduction currents at more negative onset potentials that were due to direct oxygen reduction at carbon electrodes. This result confirms the specific role of microsomal heme proteins in catalyzing oxygen reduction that appears to be facilitated by electron donation from electrode-reduced CPR molecules (see Figure 3A). It is also possible that microsomal Cyt b_5-heme may undergo reduction

by the electrode-reduced CPR. However, this reduction process in the presence of vesicles (as the case for microsomes) has been shown to be slow and less favorable.[44]

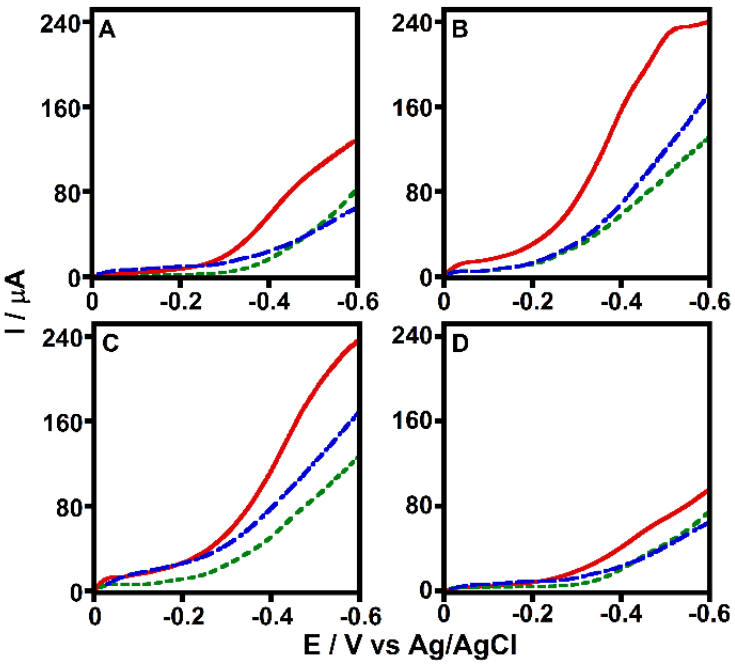

Figure 8. Cyclic voltammograms of microsomal films (red), phospholipid films (blue) and bare electrodes (green) of (A) GC, (B) HPG, (C) EPG and (D) BPG electrodes in 0.9 mM oxygen concentration. Experimental conditions: stirred pH 7.0 phosphate buffer, 0.15 M NaCl, 25 ^{o}C, scan rate 0.3 V s^{-1}.

Oxygen reduction currents by microsomal proteins on electrodes were analyzed by Lineweaver-Burk kinetics (see Figure 9) to obtain the apparent Michaelis-Menten affinity constant (K_M) of each microsomal film. Estimated apparent K_M values among four electrodes were in the range of 0.5-1.0 mM, which is not appreciably different. A possible reason could be the observed reductase-like direct electrochemistry of HLM (see Figure 3A), and as a result indirect oxygen binding to reductase-reduced heme proteins in HLM films is not directly influenced by the type of electrode used.

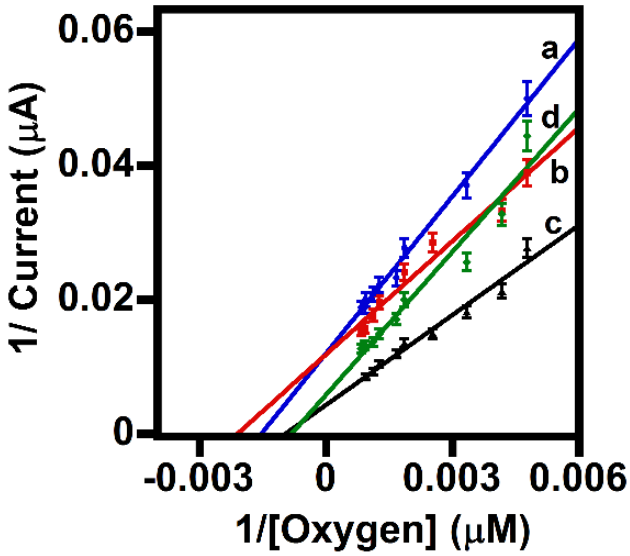

Figure 9. Lineweaver-Burk plot for oxygen reduction currents versus oxygen concentration for (a) GC/HLM, (b) HPG/HLM, (c) EPG/HLM and (d) BPG/HLM electrodes. Experimental conditions: stirred phosphate buffer pH 7.0, scan rate 0.3 V s^{-1}, 25 ^{o}C.

3.3.9 Electrocatalytic Testosterone Hydroxylation and CYP-specific Inhibition

The biocatalytic activity of liver microsomal films was inverstigated by monitoring the conversion of testosterone to 6β-hydroxytestosterone via bulk electrolysis at an applied constant potential of –0.6 V vs Ag/AgCl followed by HPLC detection of the product. Among several CYP enzymes, the CYP 2C9, 2C19, and 3A4 present in HLM have been shown to play roles in catalyzing the testosterone hydroxylation.[46] For the electrolysis study, the catalytically superior and relatively more stable HPG/HLM film were chosen as an optimal electrode system identified. After electrolysis, the reaction mixture was analyzed by HPLC, and the hydroxylation product was identified using the standard 6β-hydroxytestosterone (see Figures 10a and 11 B-a).

To determine whether the testosterone hydroxylation by the HPG/HLM film was catalyzed by CYPs, the reaction was performed in the presence of ketoconazole, a potent inhibitor of CYP activity towards testosterone hydroxylation.[16] Figure 10 b shows that ketoconazole inhibited the CYP-catalyzed formation of 6β-hydroxytestosterone. The observed biocatalytic property indicates that HLM directly adsorbed on HPG can facilitate electron transfer from electrode to CPR to CYPs and retain the bioactivity of bound CYPs. Moreover, it was confirmed that polished bare HPG electrode in the absence of HLM did not catalyze the testosterone hydroxylation (see Figure 11 A). Figure 11 B provides the chromatograms of the 6β-hydroxytestosterone standard and ketoconazole inhibitor.

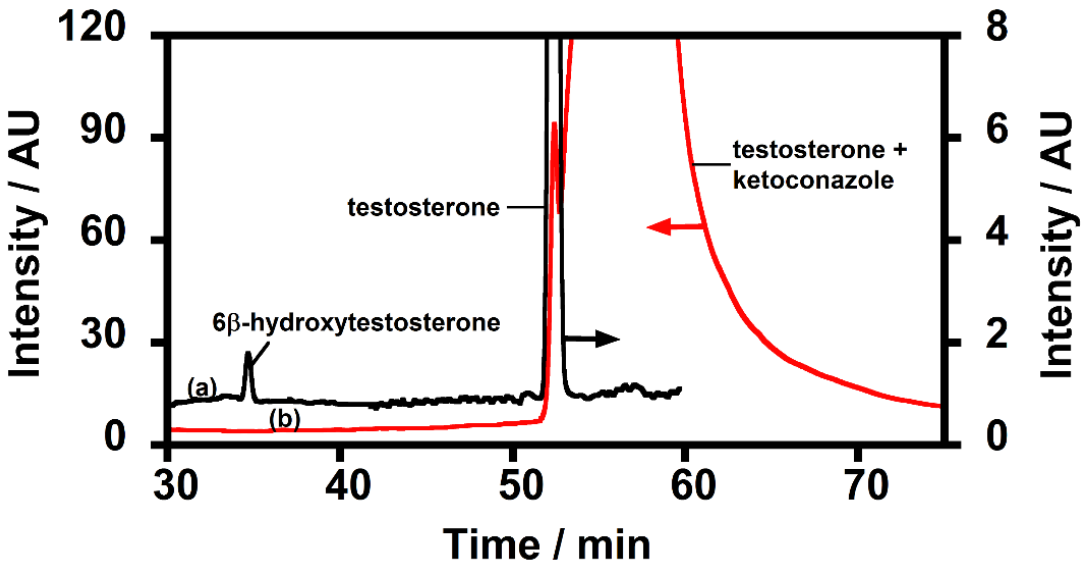

Figure 10. HPLC chromatograms of reaction mixture after 1 h of electrolysis of HPG/HLM electrodes at –0.6 V vs Ag/AgCl under a constant oxygen supply at 25 °C, pH 7.0: (a) 250 µM testosterone; (b) 250 µM testosterone + 100 µM ketoconazole.

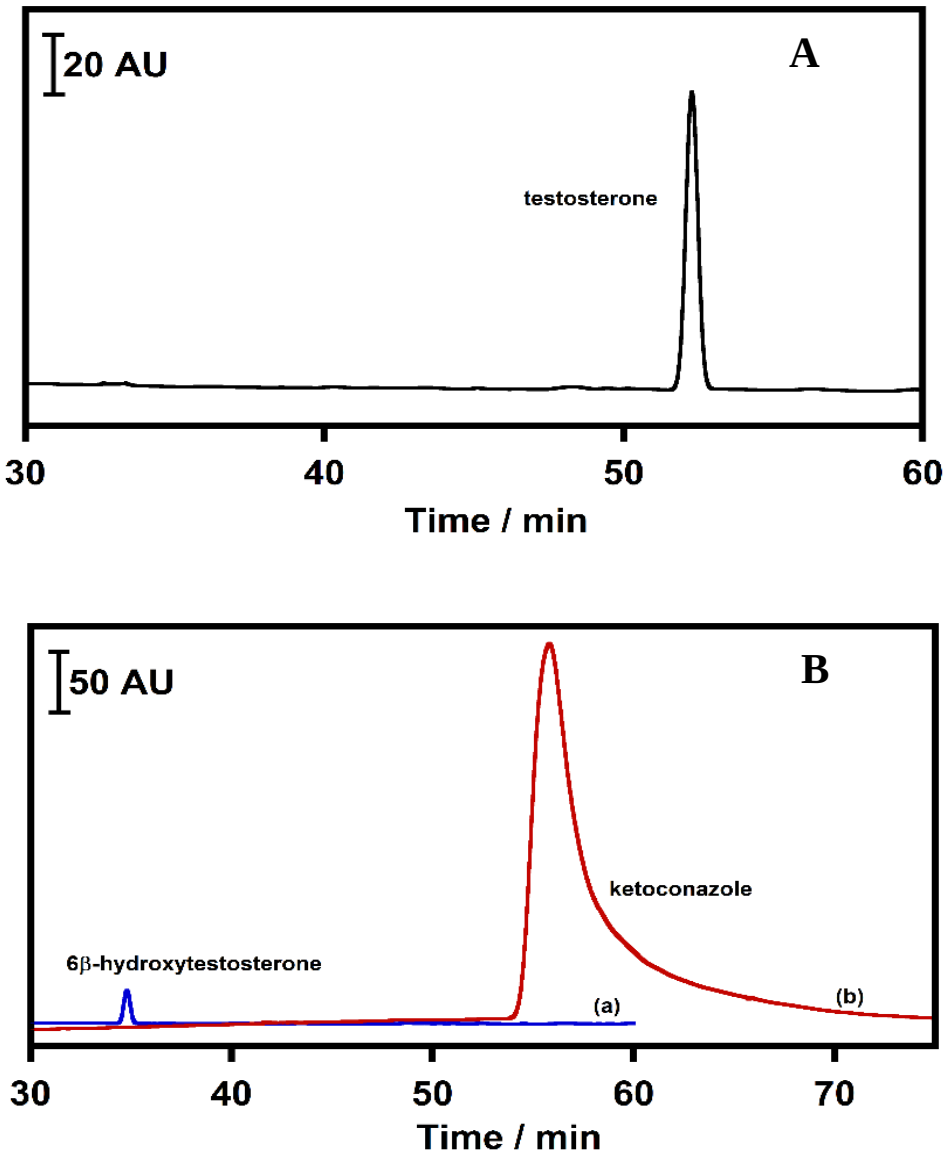

Figure 11. (A) HPLC chromatograms of 250 µM testosterone after 1 h of electrolysis of polished bare HPG electrodes at –0.6 V vs Ag/AgCl under a constant oxygen supply at 25 °C, pH 7.0 and **(B)** HPLC chromatograms of (a) 250 µM 6β-hydroxytestosterone standard and (b) 100 µM ketoconazole inhibitor.

3.4 Conclusions

The results presented demonstrate the feasibility of designing a one-step, rapid microsomal bioreactor on optimal HPG or EPG electrodes for biocatalytic applications. Film thickness of HLM, stability, and electroactive protein amounts are controlled by the extent of electrode surface defects, while rate of ET is controlled by the combined effects of surface oxygen functionalities and surface flatness of electrodes. Considering the importance of human liver microsomes in pharmaceutical drug development and toxicology fields, the presented method to simplify the microsomal bioelectrode design is suggested to be useful for inexpensive drug metabolism and inhibition assays. It is envisioned that the new findings of this study will have notable significance in the design of modern one-step liver microsomal electrodes for rapid electrochemical biosensing and biocatalytic applications.

3.5 References

1. Krishnan, S.; Rusling, J. F. *Thin Iron Heme Enzyme Films on Electrodes and Nanoparticles for Biocatalysis*, Chapter 5, In: *New and Future Developments in Catalysis*, Suib, S. L. Ed.; Elsevier Publishers, **2013**, 125-147.

2. O'Reilly, E.; Kohler, V.; Flitsch, S. L.; Turner, N. J. *Chem. Commun.* **2011**, *47*, 2490-2501.
3. Guengerich, F. P. *J. Biochem. Mol. Toxicol.* **2007**, *21*,163-168.
4. Ortiz de Montellano, P. R. Ed., *Cytochrome P450*, Kluwer/Plenum, New York, 2005.
5. Gutierrez, A.; Grunau, A.; Paine, M.; Munro, A. W.; Wolf, C. R.; Roberts, G. C. K.; Scrutton, N. S. *Biochem. Soc. Trans.* **2003**, *31*, 497-501.
6. Johnson, E. F.; Connick, J. P.; Reed, J. R.; Backes, W. L.; Desai, M. C.; Xu, L.; Estrada, D. F.; Laurence, J. S.; Scott, E. E. *Drug Metab. Dispos.* **2014**, *42*, 9-22.
7. Krishnan, S.; Schenkman, J. B.; Rusling, J. F. *J. Phys. Chem. B* **2011**, *115*, 8371-8380.
8. Das, A.; Sligar, S. G. *Biochemistry* **2009**, *48*, 12104-12112.

9. Krishnan, S.; Walgama, C. *Anal. Chem.* **2013**, *85*, 11420-11426.
10. Walgama, C.; Krishnan, S. *J. Electrochem. Soc.* **2014**, *161*, H47-H52.
11. Nerimetla, R.; Walgama, C.; Ramanathan, R.; Krishnan, S. *Electroanalysis* **2014**, *26*, 675-678.
12. Wienkers, L. C.; Heath, T. G. *Nat. Rev. Drug Discov.* **2005**, *4*, 825-833.
13. Sultana, N.; Schenkman, J. B.; Rusling, J. F. *J. Am. Chem. Soc.* **2005**, *127*, 13460-13461.
14. Krishnan, S.; Rusling, J. F. *Electrochem. Commun.* **2007**, *9*, 2359-2363.
15. Wasalathanthri, D. P.; Malla, S.; Faria, R. C.; Rusling, J. F. *Electroanalysis* **2012**, *24*, 2049 - 2052.
16. Mie, Y.; Suzuki, M.; Komatsu, Y. *J. Am. Chem. Soc.* **2009**, *131*, 6646-6647.
17. Krishnan, S.; Wasalathanthri, D.; Zhao, L.; Schenkman, J. B.; Rusling, J. F. *J. Am. Chem. Soc.* **2011**, *133*, 1459-1465.
18. Guengerich, F. P.; Martin, M. V.; Sohl, C. D.; Cheng, Q. *Nature Protocols* **2009**, *4*, 1245-1251.
19. Banks, C. E.; Compton, R. G. *Analyst* **2006**, *131*, 15-21.
20. Stewart, J. C. *Anal. Biochem.* **1980**, *104*, 10-14.
21. Samoc, A.; Miniewicz, A.; Samoc, M.; Grote, J. G. *J. Appl. Polym. Sci.* **2007**, *105*, 236-245.
22. Bard, A.; Faulkner, L. R. *In*: Electrochemical Methods: Fundamentals and Applications, Second Ed., Wiley, NJ, USA 2001.
23. Sander, R. Compilation of Henry's Law Constants for Inorganic and Organic Species of Potential Importance in Environmental Chemistry, Version 3, 1999. Available at www.henrys-law.org
24. Cracknell, J. A.; Wait, A. F.; Lenz, O.; Friedrich, B.; Armstrong, F. A. *Proc. Natl. Acad. Sci. U. S.* A. **2009**, *106*, 20681-20686.
25. Goñi, F. M.; Arrondo, J. L. R. *Faraday Discuss. Chem. Soc.* **1986**, *81*, 117-126.
26. Beng, G.; Pop, V. I.; Ionescu, M.; Hodârnău, A.; Tilinca, R.; Frangopol, P. T. *Biochim. Biophys. Acta* **1983**, *750*, 194-199.

27. Rice, R. J.; Pontikos, N. M.; McCreery, R. L. *J. Am. Chem. Soc.* **1990**, *112*, 4617-4622.

28. Blanford, C. F.; Armstrong, F. A. *J. Solid State Electrochem.* **2006**, *10*, 826-832.

29. Huang, H.; Hu, N.; Zeng, Y.; Zhou, G. *Anal. Biochem.* **2002**, *308*, 141-151.

30. Xiao, L.; Dickinson, E. J. F.; Wildgoose, G. G.; Compton, R. G. *Electroanalysis* **2010**, *22*, 269-276.

31. Shukla, A.; Gillam, E. M. J.; Bernhardt, P. V. *Electrochem. Commun.* **2006**, *8*, 1845-1849.

32. Sultana, N.; Schenkman, J. B.; Rusling, J. F. *Electroanalysis* **2007**, *19*, 2499-2506.

33. Krishnan, S.; Abeykoon, A.; Schenkman, J. B.; Rusling, J. F. *J. Am. Chem. Soc.* **2009**, *131*, 16215-16224.

34. Aono, T.; Sakamoto, Y.; Miura, M.; Takeuchi, F.; Hori, H.; Tsubaki, M. *J. Biomed. Sci.* **2010**, *17*, 90.

35. Evans, J. P.; Xu, F.; Sirisawad, M.; Miller, R.; Naumovski, L.; Ortiz de Montellano, P. R. *Mol. Pharmacol.* **2007,** *71*, 193–200.

36. Razzaq, H.; Qureshi, R.; Schiffrin, D. J. *Electrochem. Commun.* **2014**, *39*, 9–11.

37. Ghanem, M. A.; Chrétien, J.-M.; Pinczewska, A.; Kilburn, J. D.; Bartlett, P. N. *J. Mater. Chem.* **2008**, *18*, 4917–4927.

38. Munge, B.; Das, S. K.; Ilagan, R.; Pendon, Z.; Yang, J.; Frank, H. A.; Rusling, J. F. *J. Am. Chem. Soc.* **2003**, *125*, 12457–12463.

39. Laviron, E. *J. Electroanal. Chem.* **1979**, *101*, 19-28.

40. Wang, Y.; Cao, J.; Zhou, Y.; Ouyang, J.-H.; Jia, D.; Guo, L. *J. Electrochem. Soc.* **2012**, *159*, A579-A583.

41. Wei, L.; Wu, F.; Shi, D.; Hu, C.; Li, X.; Yuan, W.; Wang, J.; Zhao, J.; Geng, H.; Wei, H.; Wang, Y.; Hu, N.; Zhang, Y. *Sci. Rep.* **2013**, *3*, 2636.

42. Brunetti, B.; De Giglio, E.; Cafagna, D.; Desimoni, E. *Surf. Interface Anal.* **2012**, *44*, 491-496.

43. Chen, P.; McCreery, R. L. *Anal. Chem.* **1996**, *68*, 3958-3965.

44. Guengerich, F. P. *Arch. Biochem. Biophys.* **2005**, *440*, 204-211.

45. Kim, E. J.; Amorelli, B.; Abdo, M.; Thomas, C. J.; Love, D. C.; Knapp, S.; Hanover, J. A. *J. Am. Chem. Soc.* **2007**, *129*, 14854-14855.

46. Yamazaki, H.; Shimada, T. *Arch Biochem. Biophys.* **1997**, *346*, 161-169.

CHAPTER 4

SINGLE DROP ELECTROANALYSIS AND INTERFACIAL INTERACTIONS: SENSITIVITY VERSUS LIMIT OF DETECTION

4.1 Introduction

Chemical reactions in bulk solutions have been studied extensively, and researchers have started exploring reactions using ultra-small volumes due to advantages such as faster reaction kinetics, enhanced analytical sensitivity, and small sample requirements.[1-3] Superior biochemical characteristics of droplets are due to enhanced mixing and mass transfer and the ability to function as small reactors.[4-5] Investigation of such properties via quantitative and qualitative analysis of the contents of droplets is only possible with sophisticated analytical techniques, including molecular spectroscopy, mass spectrometry, electrophoresis, and electrochemistry.[6]

Among the various analytical techniques available, electrochemical detection of analyte droplets is favored due to its simplicity, cost-effectiveness, and the ability to modify the electrode surface to obtain good sensitivity.[7-8] Interfacial electrochemistry of droplets placed on electrodes and fundamental insights based on mass and ion transfer mechanisms have been reported.[9] Recently, Oliveira et al. showed that a single drop electrochemical system consisting of two liquid phases of water and oil can diminish charge transfer resistance in the detection of 4-nitrophenol in oil.[10] Using a single drop of redox active hexachloroiridate, changes in the heterogeneous electron

Adapted from Walgama, C.; Gallman, M.; Krishnan, S., Single Drop Electroanalysis and Interfacial Interactions: Sensitivity versus Limit of Detection. *Electroanalysis* **2016**, 28 (11), 2791-2796.

transfer rates with respect to number of layers of graphene and microscopic defects on the graphene surface (edge/basal planes) were electrochemically investigated.[11]

Heavy metals,[12] polycyclic aromatic hydrocarbons,[13] microorganisms, radioactive agents, and many other environmental pollutants[14] can be monitored via single drop electrochemical analysis. Blood glucose analysis is a remarkable point-of-care biomedical application of single drop electrochemical biosensors.[15-17] Chen et. al. developed a disposable screen printed electrode (SPE) approach for detection of uric acid in droplets of whole blood.[18] Thus, biologically and chemically relevant analytes have been detected in ultra-micro volumes.

In this study, the electroanalytical measurements of four compounds in single droplets were performed on carboxylated multiwalled carbon nanotubes (MWCNT-COOH) modified SPEs and their presence and concentration were detected using cyclic voltammetry. Acetaminophen is a pain reliever and fever reducing drug; NADH is a co-enzyme and a dietary supplement; ascorbic acid is an antioxidant and also used as a dietary supplement; and nicotine is a tobacco smoke carcinogen and present in anti-smoking pharmaceuticals. The focus of this study was to evaluate the detection sensitivity and limit of detection (LOD) of single drop assays relative to molecular sizes of anlaytes, and polar and nonpolar interfacial interactions of analytes with the MWCNT- COOH surface. To our knowledge, this study is the first to describe single drop electroanalysis for the selected compounds with insights into interfacial interactions controlling sensitivity and LOD. Detailed electron transfer, mass transport, and electrochemical kinetics were investigated in a separate study.

Results of this study convey the importance of electroanalytical methods in measuring low levels of analytes and the significance of droplet-based biosensors utilizing desired chemically or biologically functionalized SPEs. SPEs were chosen because of their user-friendly design, miniature size, portability, low cost, and disposability and because they lack interference arising from surface contamination and cleaning protocols between experiments.[19-20] Figure 1A illustrates

the schematic of SPEs for single drop analysis of analytes based on electrochemical methods. Figure 1B shows the structures of measured analytes in this study as single drops.

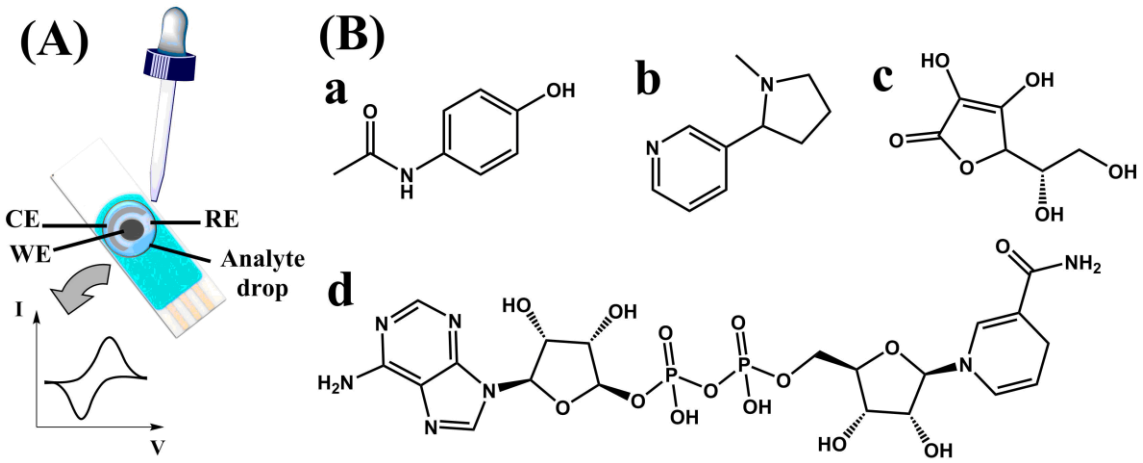

Figure 1. (A) Schematic representation of single droplet analysis using SPE made of a carbon counter electrode (CE), an MWCNT-COOH coated working electrode (WE), and a silver pseudo-reference electrode (RE). (B) a-d. Chemical structures of measured analytes as single drops. a. acetaminophen, b. nicotine, c. ascorbic acid, and d. NADH.

4.2 Experimental

4.2.1 Materials

SPEs (110 CNT, dimensions: length 33 mm; width 10 mm; height 0.5 mm) were purchased from Dropsens Ltd. [Llanera (Asturias) Spain]. The SPE electrode geometric area was 0.16 cm^2, and it was modified with MWCNT-COOH. The counter electrode was made of carbon and the pseudo-reference electrode was made up of silver. L-Nicotine was purchased from ACROS Organics and all other analytical grade chemicals, including acetaminophen, L-ascorbic acid, and NADH (β-Nicotinamide adenine dinucleotide, reduced disodium salt hydrate), were purchased from Sigma.

Acetaminophen, ascorbic acid, and NADH tablets, and nicotine gum were purchased from a local pharmacy.

4.2.2. Cyclic Voltammetric Measurements

A CH instrument 6017E electrochemical analyzer was used for cyclic voltammetry experiments under ambient atmosphere. Different concentrations of the four analytes prepared in pH 7.0 phosphate buffer were placed as 50 µL droplets on SPEs, and voltammograms were obtained.

4.2.3 Sample Preparation

Acetaminophen (2 of 500 mg), ascorbic acid (1 of 1000 mg), and NADH (8 of 5 mg) tablets were finely powdered and transferred separately into 250 mL conical flasks containing 100 mL of pH 7.0 phosphate buffer. Then the contents of flasks were sonicated for 30 min, and the mixtures were filtrated through Whatmann filter papers to remove insoluble materials. Filtrates were used for voltammetric analysis. The nicotine containing chewing gums (2 of 4 mg) were cut and dissolved in 20 mL of hexane. The mixture was then filtered and extracted with 100 mL, pH 7.0 phosphate buffer. The buffer extract was used for voltammetric analysis.[21] Appropriate sample dilutions were made to fit in the voltammeric calibration plots and estimate the amounts in the real samples.

4.3 Results and Discussion

4.3.1 Electrochemical Behavior of Analytes

The analytes were placed as a single drop (50 µL volume) on separate MWCNT-COOH SPEs, and electrochemical signals were measured by cyclic voltammetry. Figure 2 shows the background cyclic voltammograms (CVs) for buffer droplets on the SPE electrodes (dotted lines) and that of 100 µM analyte droplets (bold lines). A small sharp spike (0 - 0.1 V range) was observed for bare SPEs in buffer droplets, but the spike did not interfere with the identification of analyte peaks.

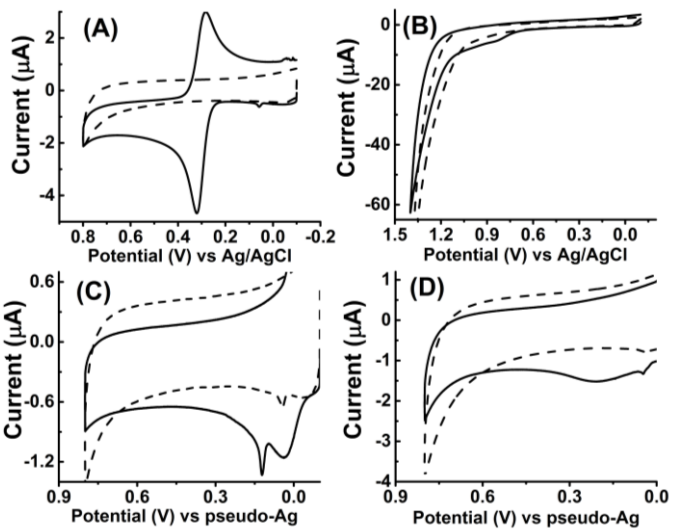

Figure 2. CVs of 100 μM droplets (50 μL volume) of (A) acetaminophen, (B) nicotine, (C) ascorbic acid, and (D) NADH placed on MWCNT-COOH SPEs at 25 °C, scan rate 25 mV s^{-1} (solid lines). Dashed lines are the CVs of a buffer drop with no added analyte.

Figure 3 represents the CVs of analyte droplets with increasing scan rates (at 1 mM analyte concentration). A linear relationship between oxidation peak currents and the square root of scan rates was observed for all four analytes (see insets in Figure 3). This indicated the diffusion-controlled electrochemical process of analytes in droplets of 50 μL volume.[22]

Figure 3 also illustrates the differences in the CV peak shapes of each analyte. For example, acetaminophen CVs suggested a quasi-reversible process (significant peak separation between oxidation and reduction peaks with increase in scan rate), and nicotine, ascorbic acid and NADH displayed the feature of almost irreversible redox process. These variations in peak shapes are indicative of differences in the kinetics of direct electron transfer and mass transport of analyte molecules at the interface of the droplet and MWCNT-COOH SPE.[22]

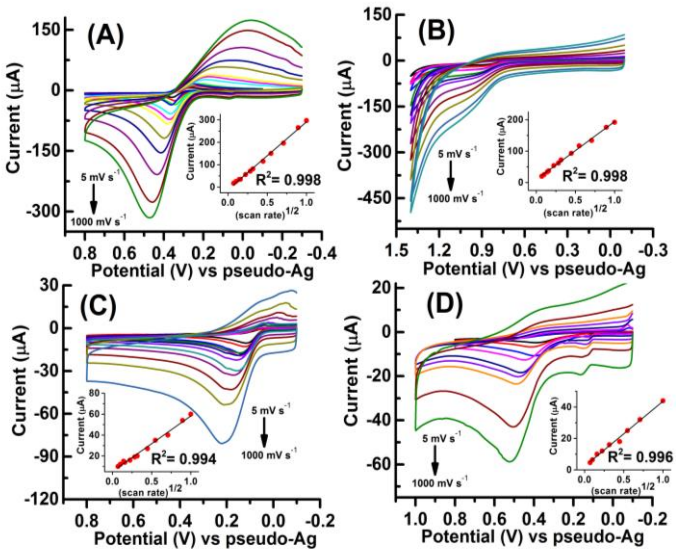

Figure 3. Scan rate dependent CVs of 1 mM droplets (50 μL volume) of (A) acetaminophen, (B) nicotine, (C) ascorbic acid, and (D) NADH placed on MWCNT-COOH SPEs. (scan rates inner to outer : 5 to 1000 mV s^{-1}). Insets show the plots of peak current vs square root of scan rate.

Figures 4A-D show the CVs for various concentrations of acetaminophen, nicotine, ascorbic acid, and NADH [(i) is for lower concentration range and (ii) is for higher concentration range of analyte droplets].

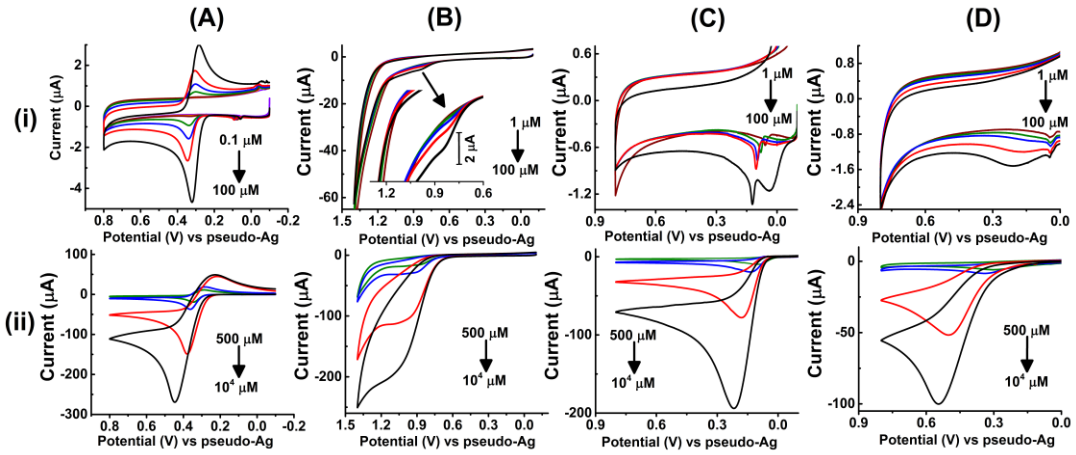

Figure 4. CVs of 50 μL droplets of varying concentrations of analytes placed on MWCNT-COOH SPEs at 25 °C, scan rate 25 mV s^{-1}: (A) acetaminophen, (B) nicotine (inset shows the enlarged view

of voltammograms), (C) ascorbic acid, and (D) NADH: (i) CVs at lower concentration range and (ii) CVs at higher concentration range.

Figure 5A shows the increase in oxidation peak currents with increasing concentration of each analyte. The sensitivity of the method from the slopes of this plot was estimated. The LOD of each analyte was calculated to be $3S_b/m$, where S_b is the standard deviation of the blank signal and m is the slope of the calibration plot (see Table 1).[23-24] The observed wide dynamic range of detection (from the LOD to 1 mM) is comparable to or better than that of many reported carbon-based SPE sensors for similar analytes.[7, 25-29]

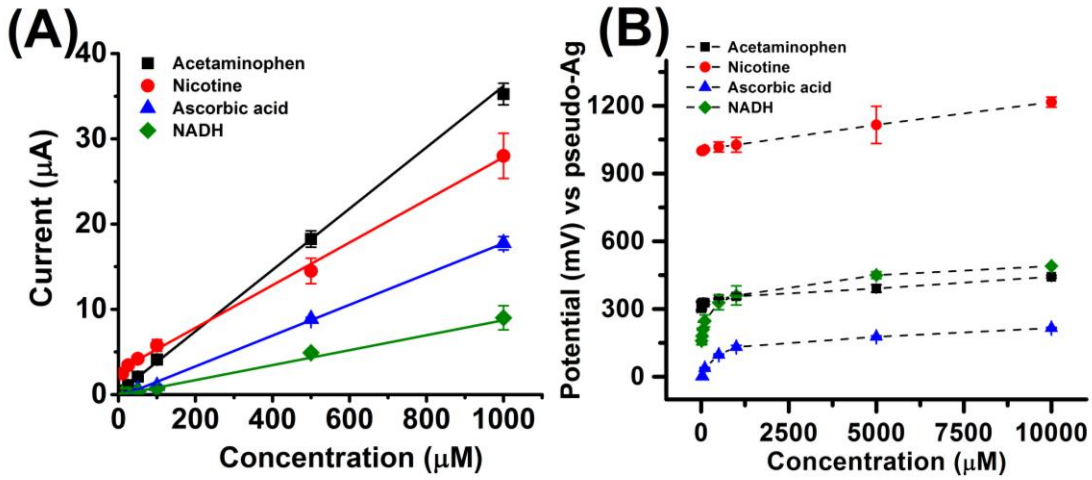

Figure 5. (A) Oxidation peak currents versus concentration of a single drop of analyte placed on MWCNT-COOH SPEs at 25 °C and measured by cyclic voltammetry at a scan rate of 25 mV s^{-1}. (B) Effect of varying concentration of analytes on the oxidation peak potential.

The oxidation peak potential of each analyte shifted to more positive values with increasing concentration (see Figure 5B). The peak shifts were more prominent for ascorbic acid and NADH compared to nictotine acetaminophen. This observation suggests greater overpotential requirements at higher concentrations of relatively polar compounds due to possible charge repulsions with the surface (related to energetics). Once the required overpotential barrier is

overcome, analytical detection features from interfacial charge transfer can be achieved (i.e., current signals).[30]

The differences in the observed LODs and sensitivity among the four analytes can be explained by the nature of interfacial secondary interactions of analytes with the MWCNT-COOH-modified SPE surface. A MWCNT is made of concentric cylindrical layers of graphene. MWCNT-COOH contains both polar –COOH groups and nonpolar sp^2 carbons of MWCNT. The sidewall basal planes of MWCNT can undergo pi-pi stacking as well as nonpolar interactions with pi-bonds and nonpolar groups of analytes.[31] The edge planes and defective sites of MWCNT are mostly polar. The -COOH groups of MWCNT offer electrostatic and hydrogen bond interactions with the polar groups of analytes.

The data showed that higher sensitivity does not always correlate with lower LOD in electroanalysis (Table 1). In this study, the decreasing order of detection sensitivity was acetaminophen > nicotine > ascorbic acid > NADH (see Figure 5A). The highest sensitivity observed for acetaminophen can be explained by its combined pi-pi and nonpolar interactions with MWCNT along with hydrogen bonding and electrostatic interactions with surface –COOH groups (via –OH and NH groups) (see Figure 6). Ascorbic acid is relatively more polar than acetaminophen and thus can interact predominantly via dipole-dipole and hydrogen bonding interactions with the MWCNT-COOH surface. This major polar interaction (i.e., less nonpolar) might be the reason for this anlayte's lower sensitivity compared to acetaminophen. Similarly, although NADH is polar, the relatively larger size of this compound compared to ascorbic acid can cause sterically hindered interaction with the electrode and thus explains its low detection sensitivity on the MWCNT-COOH surface.

Table 1. Electroanalytical measurements of single drops of acetaminophen, nicotine, ascorbic acid, and NADH.

Analyte	Oxidation Peak Potential / mV (at 100 μM)	LOD (μM)	Sensitivity (nA μM^{-1})
Acetaminophen	327 ± 7	0.13	36
Nicotine	1006 ± 4	4.8	25
Ascorbic acid	38 ± 3	0.83	18
NADH	247 ± 27	1.7	9

Nicotine is the least polar of the four compounds and it has predominantly nonpolar (e.g., dispersion, pi-pi) interactions, which further supports the influence of nonpolar interactions in providing better sensitivity than polar ascorbic acid and NADH molecules.

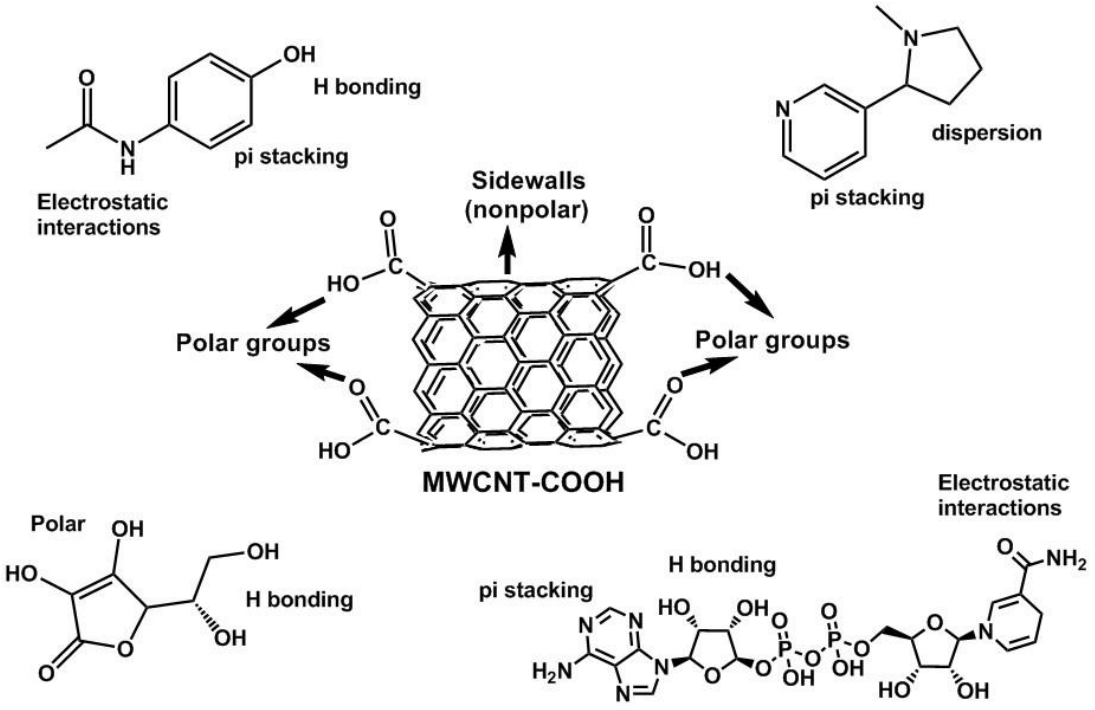

Figure 6. Possible interfacial interactions of analytes with the MWCNT surface and –COOH groups; these interactions may explain the observed variations in sensitivity and LODs of the measured analytes.

The following trend of increasing magnitudes of LODs was observed: acetaminophen < ascorbic acid < NADH < nicotine. This observation suggests that polar compounds (acetaminophen, ascorbic acid, and NADH) favor better charge transport at the interface of an analyte droplet and the MWCNT-COOH SPE surface than moderate polar/nonpolar compounds (e.g., nicotine). The lowest LOD of acetaminophen is attributed to the synergistic combination of polar and nonpolar interactions with the MWCNT surface and –COOH functional groups as described above.

Taken together, the results suggest that the detection sensitivity of a redox analyte is controlled by the extent of predominant nonpolar interactions of the analyte with the MWCNT-COOH SPE

sensor surface. However, LOD is controlled by the extent of charge transfer occurring at the interface of analyte molecules and the electrode and is favored by polar interfacial interactions. Thus, higher sensitivity does not always have to correlate with lower detection limits in an electroanalytical method.

4.3.2 Application to Commercial Pharmaceuticals

The practical application of the SPEs for single drop electroanalysis of acetaminophen, nicotine, ascorbic acid, and NADH was validated using real pharmaceutical samples. Sample preparation is described under Experimental. The results are summarized in Table 2.

Table 2. Determination of acetaminophen, nicotine, ascorbic acid, and NADH in commercially available pharmaceuticals.

Sample	Label amount (mg)	Determined (mg)	Recovery (%)
Acetaminophen tablet	500	489 ± 10	97.8
Nicotine chewing gum	4	3.7 ± 0.1	92.2
Ascorbic acid tablet	1000	985 ± 20	98.5
NADH tablet	5	5.0 ± 0.2	99.4

Excellent recovery percentages (> 97%) were obtained in the estimation of acetaminophen, ascorbic acid, and NADH in commerically available tablets. The relatively lower percentage recovery of nicotine in chewing gum (~ 92%) is attributed to the extraction efficiency of the procedure followed rather than the detection aspect.

4.4 Conclusions

In summary, a single drop analysis of four pharmaceutically and biologically relevant compounds was described using MWCNT-COOH-modified SPEs. The favorable large surface area and multiple interactions offered by the electrode surface provided highly sensitive detection of analytes with a wide dynamic range, and interfacial charge transport facilitated by polar interactions offered lower detection limits. Above droplet electroanalytical method and the fundamental insights regarding the molecular interactions with the sensor surface should allow design of sensors with high sensitivity and low detection limits via appropriate control of surface properties to induce desired interfacial interactions based on analyte structures confined in a droplet. Successful demonstration on real samples implies negligible interferences from the matrix and applicability of the method for pharmaceutical quality assurance (QA) purposes.

4.5 References

1. J. K. Lee, S. Banerjee, H. G. Nam, R. N. Zare, *Quarterly reviews of Biophysics* **2015**, *48*, 437-444.
2. S. F. Bakhoum, G. R. Agnes, *Anal. Chem.* **2005**, *77*, 3189-3197.
3. T. Schneider, J. Kreutz, D. T. Chiu, *Anal. Chem.* **2013**, *85*, 3476-3482.
4. H. Song, R. F. Ismagilov, *J. Am. Chem. Soc.* **2003**, *125*, 14613-14619.
5. H. Song, J. D. Tice, R. F. Ismagilov, *Angew. Chem. Int. Ed.* **2003**, *42*, 768-772.
6. Y. Zhu, Q. Fang, *Anal. Chim. Acta* **2013**, *787*, 24-35.
7. P. Fanjul-Bolado, P. J. Lamas-Ardisana, D. Hernández-Santos, A. Costa-García, *Anal. Chim. Acta* **2009**, *638*, 133-138.
8. S. D. Sprules, J. P. Hart, R. Pittson, S. A. Wring, *Electroanalysis* **1996**, *8*, 539-543.

9. C. E. Banks, T. J. Davies, R. G. Evans, G. Hignett, A. J. Wain, N. S. Lawrence, J. D. Wadhawan, F. Marken, R. G. Compton, *Phys. Chem. Chem. Phys.* **2003**, *5*, 4053-4069.
10. E. S. Oliveira, P. A. Fiorito, H. B. Suffredini, *Electroanalysis* **2014**, *26*, 1660-1663.
11. P. S. Toth, A. T. Valota, M. Velicky, I. A. Kinloch, K. S. Novoselov, E. W. Hill, R. A. W. Dryfe, *Chemical Science* **2014**, *5*, 582-589.
12. K. C. Honeychurch, J. P. Hart, *Trends Anal. Chem.* **2003**, *22*, 456-469.
13. E. J. Moore, M. P. Kreuzer, M. Pravda, G. G. Guilbault, *Electroanalysis* **2004**, *16*, 1653-1659.
14. Hayat, J. L. Marty, *Sensors (Basel, Switzerland)* **2014**, *14*, 10432-10453.
15. Heller, B. Feldman, *Chem. Rev.* **2008**, *108*, 2482-2505.
16. K. E. Toghill, R. G. Compton, *Int. J. Electrochem. Sci.* **2010**, *5*, 1246-1301.
17. Chen, Q. Xie, D. Yang, H. Xiao, Y. Fu, Y. Tan, S. Yao, *RSC Advances* **2013**, *3*, 4473-4491.
18. J.-C. Chen, H.-H. Chung, C.-T. Hsu, D.-M. Tsai, A. Kumar, J.-M. Zen, *Sensors and Actuators B: Chemical* **2005**, *110*, 364-369.
19. Z. Taleat, A. Khoshroo, M. Mazloum-Ardakani, *Microchim Acta* **2014**, *181*, 865-891.
20. M. Li, Y.-T. Li, D.-W. Li, Y.-T. Long, *Anal. Chim. Acta* **2012**, *734*, 31-44.
21. Ľ. Švorc, D. M. Stanković, K. Kalcher, *Diamond Relat. Mater.* **2014**, *42*, 1-7.
22. Bard, L. R. Faulkner, in *Electrochemical Methods: Fundamentals and Applications, 2nd Ed.*, Wiley, NJ, USA 2000.
23. G. L. Long, J. D. Winefordner, *Anal. Chem.* **1983**, *55*, *712A-724A.*
24. M. R. Shahmiri, A. Bahari, H. Karimi-Maleh, R. Hosseinzadeh, N. Mirnia, *Sensors and Actuators B: Chemical* **2013**, *177*, 70-77.
25. Fernandez, Z. Heger, R. Kizek, T. Ramakrishnappa, A. Boruń, N. H. Faisal, *Int. J. Electrochem. Sci* **2015**, *10*, 7440-7452
26. T. R. Saciloto, P. Cervini, É. T. Gomes Cavalheiro, *Anal. Lett.* **2013**, *46*, 312-322.

27. L. Highton, R. O. Kadara, N. Jenkinson, B. Logan Riehl, C. E. Banks, *Electroanalysis* **2009**, *21*, 2387-2389.

28. J. Ping, J. Wu, Y. Wang, Y. Ying, *Biosens. Bioelectron.* **2012**, *34*, 70-76.

29. F. Valentini, D. Romanazzo, M. Carbone, G. Palleschi, *Electroanalysis* **2012**, *24*, 872-881.

30. Z. Wang, J. Liu, Q. Liang, Y. Wang, G. Luo, *Analyst* **2002**, *127, 653-658.*

31. Walgama, N. Means, N. F. Materer, S. Krishnan, *Phys. Chem. Chem. Phys.* **2015**, *17*, 4025-4028.

CHAPTER 5

EDGE-TO-EDGE INTERACTION BETWEEN CARBON NANOTUBE-PYRENE COMPLEXES AND ELECTRODES FOR BIOSENSING AND ELECTROCATALYTIC APPLICATIONS

5.1 Introduction

Carbon nanotube-mediated enhanced biocatalytic reactions of enzymes is an emerging research area. Applications of CNTs in the globally important areas of biocatalysis, biodevices, biosensing, and sustainable energy have been detailed in the literature.[1-3] In this study, w the π-π stacked nanotube-pyrene-based surface chemistry that allows covalent immobilization of enzyme catalysts was focused to study relevant direct electrochemical and biocatalytic properties.[4] Pyrolytic graphite material consists of basal (parallel to the surface) and edge planes (perpendicular to the surface). Dai et al. reported that the basal plane of sidewalls of CNTs could undergo π-π interaction with functionalized pyrene compounds, which would allow facile covalent protein immobilization.[5] Compton et al. unraveled the contribution of CNT edge planes to the electrocatalytic properties of CNTs.[6] They also illustrated the greater electroactivity of edge plane electrodes over basal plane electrodes for a dissolved redox species in solution.

Adapted from Walgama, C.; Means, N.; Materer, N. F.; Krishnan, S., Edge-to-edge interaction between carbon nanotube-pyrene complexes and electrodes for biosensing and electrocatalytic applications. *PCCP* **2015**, 17 (6), 4025-4028 with permission from the PCCP Owner Societies.

In another study, Lisdat et al. investigated the effects of different aromatic compounds stacked with CNT-modified electrodes on the oxygen reduction efficiency of immobilized bilirubin oxidase enzyme. Krishnan and Armstrong developed a membraneless hydrogen fuel cell with enhanced power output and stability by covalently immobilizing E. coli hydrogenase-1 as the anode catalyst and bilirubin oxidase as the cathode catalyst on CNT-pyrenebutyric acid (CNT/Py)-modified electrodes.[8] Katz et al. designed an implantable glucose biofuel cell that utilized CNT-pyrene surface chemistry.[9] Direct and efficient reduction of oxygen by laccase immobilized on different pyrene compounds-modified CNT electrodes has also been shown.[10,11] These studies show that nanotube-pyrene-based electrode surface modification for biocatalytic applications is receiving immense attention at present.

Our group has previously demonstrated the differential immobilization of a heme protein via Lys or Glu residues onto different pyrene derivatives bound to CNTs on the surface of high purity graphite (HPG) electrodes.[4] Since an HPG surface consists of a mixture of basal and edge planes to varying extents, the selective interaction of CNT with either basal plane or edge plane in affecting the pyrene compound stacking and electrocatalytic properties of immobilized redox enzyme is not easily understood. It can be proposed that the understanding this fundamental feature is crucial for designing efficient electrochemical enzyme biosensors and bioreactors.

Therefore, in this study, the interaction of purely basal plane (BP) or purely edge plane (EP) pyrolytic graphite electrodes with multi-walled carbon nanotubes (MWNT), π-π stacked with pyrenyl compounds in influencing the electrocatalytic properties of immobilized myoglobin (Mb), was demonstrated using as a redox protein model. For comparison, two non-graphitic electrodes (with no EP or BP surface) including glassy carbon (GC) and gold (Au) electrodes were chosen. The MWNT/Py modification was performed on each electrode surface, and this step was followed by the covalent immobilization of Mb (denoted as MWNT/Py-Mb). The procedure to covalently

attach myoglobin to obtain MWNT/Py-Mb films is similar to that described in our gorup's prior report.[4]

In this study, the results of electrocatalytic currents, electroactive enzyme coverage, and spectroscopic studies are compared to understand the influences of the underlying edge versus basal plane surface on MWNT/Py modification and subsequent peroxidase activity of the attached Mb film. The electrochemical and electrocatalytic peroxide reduction properties of immobilized Mb on the designed various electrode materials were investigated by cyclic and rotating disk voltammetry (RDV) methods, respectively.

5.2 Experimental

5.2.1 Chemicals and Materials

Disk electrodes made of purely EP or purely BP (Momentive Performance Materials Ltd.), and non-graphitic Au and GC electrodes (CH Instruments) were used in this study (geometric area of each electrode was 0.2 cm^2). MWNT (outer diameter 10–15 nm, inner diameter 2–6 nm, length 0.1–10 μm), equine heart myoglobin (Mb, ≥ 90%, SDS-PAGE), dimethyl formamide (DMF), 1-pyrenebutyric acid (Py), t-Butyl hydroperoxide (t-BuOOH), 1-ethyl-3-[3-dimethylaminopropyl]carbodiimide hydrochloride, and N-hydroxysuccinimide were purchased from Sigma (Milwaukee, USA). All other chemicals were analytical grade.

5.2.2 Preparation of Protein Films on Various Electrodes Modified with MWNT/Py Units

The procedure to covalently attach myoglobin to MWNT/Py-modified electrodes to obtain MWNT/Py-Mb films was similar to that described in our group's prior reports.[2,8] Briefly, 15 μL of 1 mg mL^{-1} MWNT in DMF were dry coated on electrodes and π-π stacked with Py (10 mM in DMF) molecules. The Mb surface lysine residues (PDB: 2FRF) were covalently attached to the –COOH groups of the MWNT/Py surface of various electrodes by amine-carboxylic acid coupling chemistry (denoted as electrode/MWNT/Py-Mb, where electrode = EP, BP, GC, or Au). The electrochemical and electrocatalytic peroxide reduction properties of immobilized Mb on the designed electrode materials were investigated by cyclic voltammetry and rotating disk voltammetry (RDV) methods, respectively.

5.2.3 Instrumentation

Electrochemical measurements were performed using a CH instrument (Model: CHI 6017E, Texas, USA). RDV was performed to study the catalytic reduction rate of t-BuOOH at a rotation rate of 1000 rpm (EcoChemie Autolab rotator supplied with a motor controller, Metrohm Inc.). A three-electrode electrochemical cell equipped with an Ag/AgCl reference (3 M KCl), a Pt-wire counter electrode, and MWNT/Py-Mb films on the various working electrodes were used. Fluorescence emission spectra of Py solutions were obtained using a Varian Cary eclipse fluorescence spectrophotometer. The excitation and emission slit widths were set at 5 nm. The excitation wavelength was set at 284 nm and emission was monitored at 377 nm. The X-ray photoelectron spectroscopy (XPS) analyses were performed using the Mg anode of a PHI 300 W twin anode X-ray source and the PHI double-pass cylindrical mirror analyzer as the detector with a pass energy of 100 eV. The instrument was equipped with a surface analysis system with a base pressure of 2 x 10^{-10} Torr. General survey scans were carried out for the EP/MWNT/Py-Mb and BP/MWNT/Py-

Mb electrodes to qualitatively assess how the edge and basal plane effects on MWNT/Py modification and influence the surface density of immobilized Mb molecules.

5.3 Results and Discussion

Figure 1 represents the background subtracted anaerobic (in nitrogen) cyclic voltammograms (CVs) of the designed Mb films on EP, BP, GC, and Au electrodes. The observed reversible CVs confirm the direct electronic communication between the modified electrodes and the Mb-heme redox center.[12]

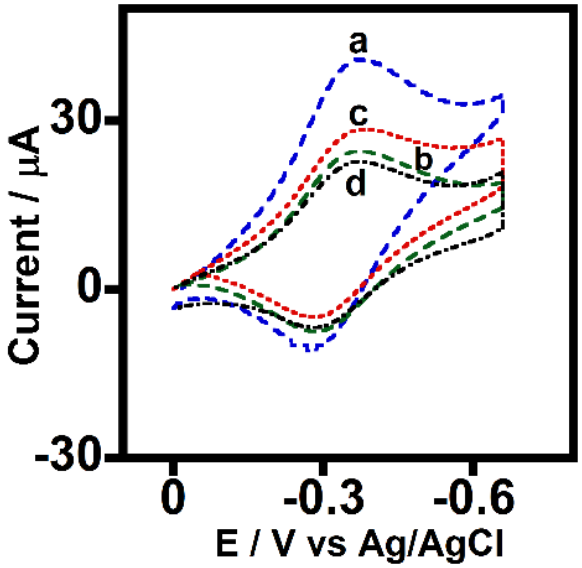

Figure 1. Background subtracted cyclic voltammograms of MWNT/Py-Mb films on a. EP, b. BP, c. GC, and d. Au electrodes at 25 °C in anaerobic nitrogen purged phosphate buffer containing 0.15 M NaCl (pH 7.0), scan rate 0.5 Vs^{-1}.

Figure 2 shows the tert-Butyl hydrogenperoxide (t-BuOOH) reduction currents catalyzed by the covalent Mb films on various electrode materials modified with MWNT/Py units (see curves a-d). These catalytic currents were subtracted for the small background currents (due to direct oxygen reduction) from the respective MWNT/Py films on each electrode with no attached Mb (see Figure 2, e-h).

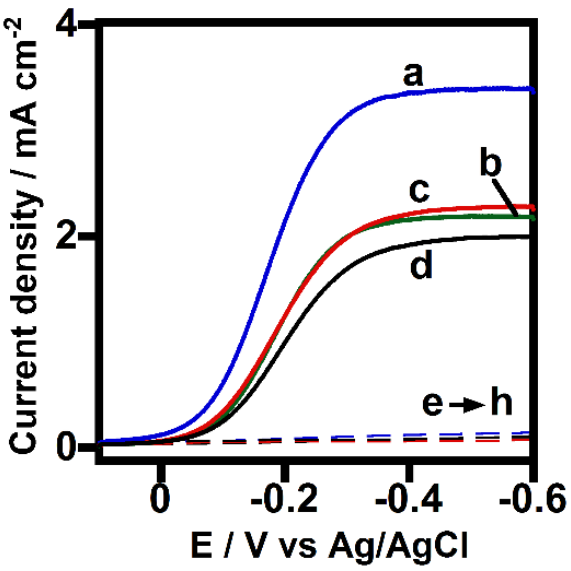

Figure 2. Peroxide reduction currents for modified MWNT/Py-Mb films on a. EP, b. BP, c. GC, and d. Au electrodes at 2.0 mM t-BuOOH. The small background currents from MWNT/Py films in the absence of immobilized Mb on each electrode are also shown (curves e-h). Experimental conditions: anaerobic pH 7.0 phosphate buffer, 0.15 M NaCl, 25 ^{o}C, scan rate 0.1 V s^{-1}, rotation rate 1000 rpm.

The Tafel analysis of the catalytic voltammograms yielded similar slope values for all Mb films on MWNT/Py-modified electrodes (see Figure 3). This indicates that similar peroxide reduction mechanism is followed by the designed Mb films.[13] The decrease in Tafel slope values at low over-potentials can be attributed to the presence of adsorbed peroxide molecules on the modified protein electrode surfaces to rapidly undergo reduction (see Figure 3).[14]

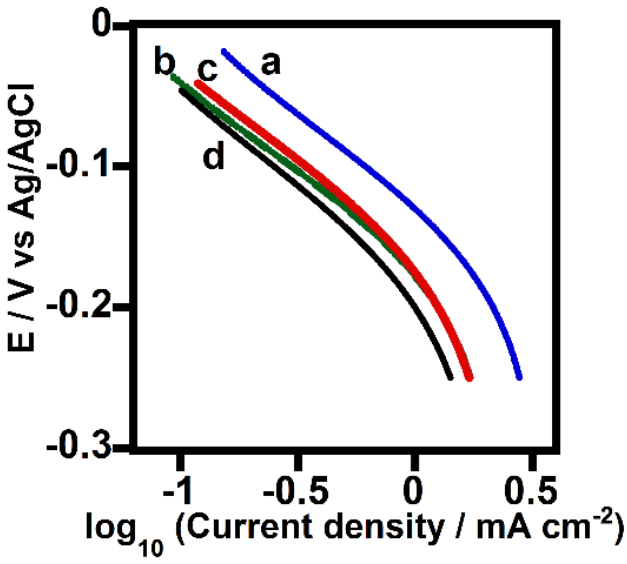

Figure 3. Tafel plots for peroxide reduction by MWNT/Py-Mb films on a. EP, b. BP, c. GC, and d. Au electrodes for the catalytic voltammograms shown in Figure 2

The average reduction current densities among the BP/MWNT/Py-Mb and non-graphitic GC/MWNT/Py-Mb and Au/MWNT/Py-Mb electrodes were comparable to each other. In contrast, the EP/MWNT/Py-Mb electrode showed a significantly greater reduction current density than the BP/MWNT/Py-Mb electrode (see Figure 2). In addition, the EP/MWNT/Py-Mb film required relatively smaller onset peroxide reduction potential compared to the Mb films on the BP/MWNT/Py and other electrodes (Figure 2a versus 2b-d). This suggests the possibility for the existence of a catalytically superior edge-edge interaction between MWNT and edge plane electrodes to expose a large surface area of MWNT-basal planes for high density stacking of Py and the protein attachment. In order to examine this, a further investigation was specifically focused on understanding the interaction of purely edge and purely basal plane characteristics of electrodes towards the MWNT/Py modification and subsequently immobilized heme protein properties as detailed below.

When EP was used as the substrate electrode, the possible interaction of the edge plane sides of the MWNT with the electrode can expose a large portion of the MWNT sidewalls. As a result, the basal plane nature of MWNT sidewalls can thus allow highly dense π-π stacking of Py molecules with

exposed –COOH end groups. In contrast, in the case of the BP electrode, the MWNT would interact mainly via the sidewalls basal planes, and thereby expose only a small proportion of MWNT-basal plane sites to undergo π-π stacking with Py molecules. The described edge versus basal plane surface effects was experimentally verified by quantifying the immobilized Py molecules via fluorescence spectrometry. The difference in the fluorescence intensities of free Py solutions before and after stacking onto EP/MWNT or BP/MWNT electrode were measured (Figure 4). From this, it was estimated that about 3.6 nmol of Py molecules were bound to the EP/MWNT electrode and 2.7 nmol of Py molecules were bound to the BP/MWNT electrode per unit electrode geometric area (in cm^2). Figure 4 (inset) shows the calibration plot of standard Py solutions used in the estimation of MWNT/Py-bound Py molecules.

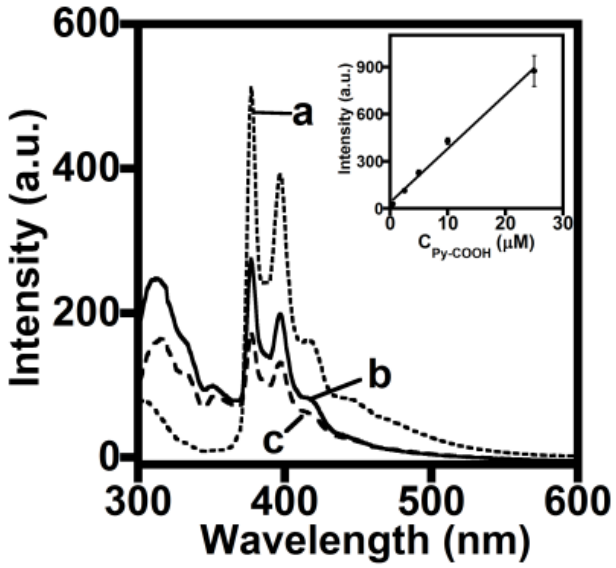

Figure 4. Fluorescence emission spectra of Py solutions: a. before adding to electrodes; and those after π-π stacking with b. BP/MWNT and c. EP/MWNT electrodes. Inset shows the calibration plot of Py standards used for estimating the electrode-bound Py molecules based on the emission peak at 377 nm.

The availability of more π-π stacked Py-linkers on EP/MWNT electrode compared to the BP/MWNT electrode can be further expected to facilitate the covalent immobilization of larger number of Mb molecules on the EP/MWNT/Py electrode. This premise is indeed supported by the observed larger electroactive protein coverage of the Mb film on EP/MWNT/Py electrode compared to the other electrodes (see Table 1 and Figure 1).

The area under the anaerobic cyclic voltammetry peak provided the electric charge (Q in coulombs) from which the electroactive protein amount was calculated using the equation $Q = nFA\Gamma$, where, n is the number of electrons transferred in the redox reaction (n = 1 for Mb-heme), F is the Faraday constant (96485 C), A is the electrode area (0.2 cm^2), and Γ is the electroactive protein coverage in mol cm^{-2}.[15] Table 1 also lists the measured formal potentials and peroxide reduction current densities (reduction current divided by electrode geometric area) of MWNT/Py-Mb films on different electrodes. All modified electrodes exhibited similar formal potentials that corresponded to the Mb-heme redox center at pH 7.0.[4,16]

Table 1. Formal potentials, electroactive surface coverage, and reduction current densities of MWNT/Py-Mb films assembled on various electrodes.

Electrode	Eo' (V)	Γ (pmol cm^{-2})	Reduction current density at 0.5 V vs. Ag/AgCl, 2 mM t-BuOOH, 1000 rpm, pH 7.0. (mA cm^{-2})
EP	–0.32 ± 0.01	237 ± 11	3.5 ± 0.2
BP	–0.32 ± 0.01	122 ± 17	2.0 ± 0.1
GC	–0.33 ± 0.01	117 ± 5	2.2 ± 0.1
Au	–0.32 ± 0.01	84 ± 5	1.8 ± 0.1

The estimated Γ of Mb film attached to MWNT/Py units on the EP electrode was ~ 2-fold greater than that of the analogous films on BP and GC electrodes and ~3-fold better than that on the Au electrode. Taken together, the BP, and the smooth and relatively defect free GC and Au electrodes with no edge plane feature do not appear to provide any better enzyme coverage and catalytic properties than the EP electrode for MWNT/Py modification and protein immobilization.

The Mb films on EP/MWNT/Py-Mb and BP/MWNT/Py-Mb electrodes were characterized by X-ray photoelectron spectroscopy (XPS) under high vacuum conditions. The XPS data showed the presence of higher quantity of nitrogen element (arising from the Mb polypeptide) in the EP/MWNT/Py-Mb film compared to the BP/MWNT/Py-Mb film (see Figure 5). Thus, the fluorescence and XPS results support the observed electrochemical properties and ascertain the favorable edge-edge interaction of EP surface with MWNT/Py modification to allow high density electroactive protein immobilization via the exposed Py-linkers from MWNT-basal planes.

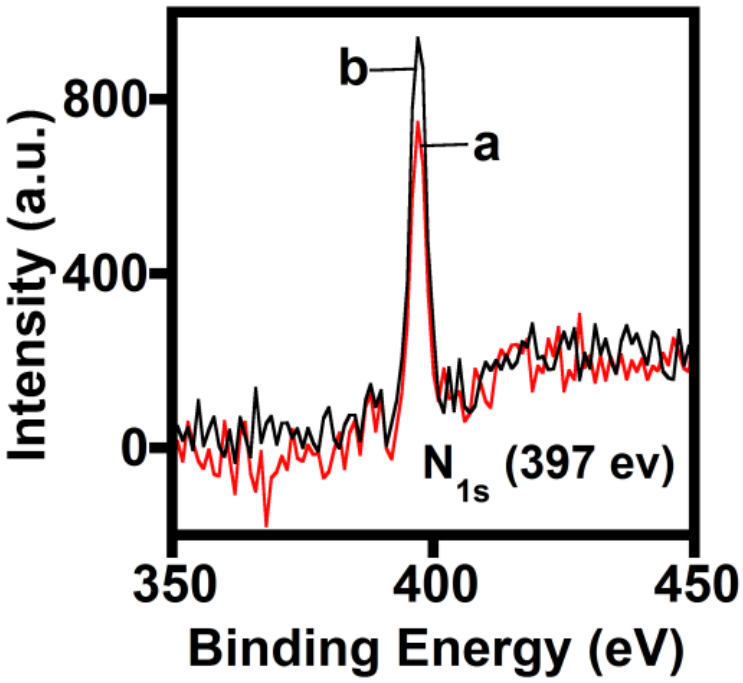

Figure 5. XPS spectra of a. BP/MWNT/Py-Mb and b. EP/MWNT/Py-Mb electrodes.

5.4 Conclusions

In summary, the edge plane effect in the design of a large, conductive MWNT/Py framework for protein immobilization and electrocatalytic applications was demonstrated. The observed catalytic currents suggest the role of MWNT arrangement in controlling the Py stacking and subsequent covalent protein immobilization more favorably on EP electrodes in comparison with BP and non-graphitic GC and Au electrodes. To our knowledge, this is the first report that details the interaction of nanotube-pyrene surface chemistry with various carbon and non-graphitic electrode materials. Exposure of the basal plane of nanotubes for efficient pyrene compound stacking and facilitating high density electroactive protein immobilization on EP electrode is suggested to be crucial in providing high catalytic currents. Detailed kinetic studies of the designed protein electrodes are planned as next objectives. Overall, the outcome of this communication is expected to be significant in the development of efficient electrocatalytic systems for synthesis, sensing, and renewable

energy applications, as the nanotube-pyrene arrangements can be suitably controlled by the choice of underlying electrode substrate.

5.5 References

1. E. Lojou, *Electrochim. Acta,* **2011**, *56,* 10385.
2. M. F. L. De Volder, S. H. Tawfick, R. H. Baughman and A. J. Hart, *Science*, **2013**, *339*, 535.
3. S. Park, M. Vosguerichian and Z. Bao, *Nanoscale*, **2013**, *5*, 1727.
4. C. Walgama and S. Krishnan, *J. Electrochem. Soc.*, **2014**, *161*, H47.
5. R. J. Chen, Y. Zhang, D. Wang and H. Dai, *J. Am. Chem. Soc.,* **2001**, *123,* 3838.
6. C. E. Banks and R. G. Compton, *Analyst*, **2006**, *131*, 15.
7. G. Göbel and F. Lisdat, *Electrochem. Commun.*, **2008**, *10,* 1691.
8. S. Krishnan and F. A. Armstrong, *Chem. Sci.*, **2012**, *3*, 1015.
9. L. Halamkova, J. Halamek, V. Bocharova, A. Szczupak, L. Alfonta and E. Katz, *J. Am. Chem. Soc.*, **2012**, *134*, 5040.
10. F. Giroud and S. D. Minteer, *Electrochem. Commun.*, **2013**, *34*, 157.
11. N. Lalaoui, K. Elouarzaki, A. Le Goff , M. Holzinger and S. Cosnier, *Chem. Commun.*, **2013**, *49*, 9281.
12. S. Krishnan, A. Abeykoon, J. B. Schenkman and J. F. Rusling, *J. Am. Chem. Soc.*, **2009**, *131*, 16215.
13. M. S. Thorum, C. A. Anderson, J. J. Hatch, A. S. Campbell, N. M. Marshall, S. C. Zimmerman, Y. Lu and A. A. Gewirth, *J. Phys. Chem. Lett.*, **2010**, *1*, 2251.
14. (a) E. Negro, K. Vezzu, F. Bertasi, P. Schiavuta, L. Toniolo, S. Polizzi and V. Di Noto, *ChemElectroChem*, 2014, **1**, 1359; (b) E. Negro, S. Polizzi , K. Vezzu, L. Toniolo, G. Cavinato and V. Di Noto, *Int. J. Hydrogen Energy*, **2014**, *39*, 2828.

15. S. Krishnan, D. Wasalathanthri, L. Zhao, J. B. Schenkman and J. F. Rusling, *J. Am. Chem. Soc.*, **2011**, *133*, 1459.

16. R. Nerimetla, C. Walgama, R. Ramanathan and S. Krishnan, *Electroanalysis,* **2014**, *26*, 675.

CHAPTER 6

ENHANCED ELECTROACTIVITY AND SUBSTRATE AFFINITY OF MICROPEROXIDASE-11 ATTACHED TO PYRENE-LINKERS Π-Π STACKED ON CARBON NANOSTRUCTURE ELECTRODES

6.1 Introduction

The nature of protein arrangement on the surface of electrode plays an important role in controlling the direct electron transfer and catalytic properties.[1-4] Due to this reason, the specific immobilization of metalloenzymes on various functionalized "nano" surfaces has gained enormous attention recently. Both the covalent and non-covalent attachment methods have been reported for attaching enzymes to carbon nanostructures for electrocatalytic applications.[5-12] Among several redox-active proteins attached to nanotube-modified electrodes, MP-11 (an 11- amino acid heme-iron peptide of cytochrome c) has gained enormous interests due to its small size with hydroxylation and peroxidase activities, similar to heme peroxidases and drug-metabolizing cytochrome P450 enzymes.[9,13] Microperoxidases are obtained from the proteolytic digestion of cytochrome c and retain the proximal histidine (His18) ligand of heme with the proximal imidazole coordinated to the heme-iron tightly at neutral pH.[14]

Adapted from Prasad, K. S.; Walgama, C.; Krishnan, S., Enhanced electroactivity and substrate affinity of microperoxidase-11 attached to pyrene-linkers π–π stacked on carbon nanostructure electrodes. *RSC Advances* **2015**, 5 (16), 11845-11849 with permission from The Royal Society of Chemistry.

The axial coordination of histidine to the ferric-heme has been shown to have a crucial role in the activity of peroxidases.[15-16] Prior studies reported the immobilization of MP-11 on gold surface by self-assembly techniques, simple adsorption and covalent attachment onto carbon nanotubes, and adsorption to nonporous films of indium tin oxide or silica cavity arrays. [9,13-25]

Katz and Willner studied the direct electrochemistry of MP-11 as a self-assembled monolayer on a cystamine-modified gold electrode.[18] Gooding et al. examined the MP-11 film bound to the free ends of aligned –COOH functionalized, shortened single-walled carbon nanotubes (SWNT) on the surface of cysteamine-layered gold electrodes.[9] Dong et al. used an adsorption approach involving the immersion of MWNT-modified glassy carbon electrodes in MP-11 solution for 10 h.[22] Another study utilized the covalent immobilization of MP-11 onto carbon nanotube structures by ion soft-landing method.[17] However, to our knowledge, the electrocatalytic properties of MP-11 films covalently linked onto pyrenyl carbon-nanostructures have not been investigated.

6.2 Experimental

6.2.1 Materials

Equine heart microperoxidase-11 (MP-11) sodium salt, multiwalled carbon nanotubes (carbon >90% trace metal basis, outer diameter 10–15 nm, inner diameter 2–6 nm, length 0.1–10 μm, average wall thickness 5-15 graphene layers), 1-ethyl-3-[3-dimethylaminopropyl]carbodiimide hydrochloride (EDC), *tert*-butyl hydroperoxide (t-BuOOH), 1-pyrenebutyric acid (Py), and N-hydroxysuccinimide (NHS) were purchased from Sigma and used as received. High purity graphite electrode disks (Grade: POCO EDM-4, Average Particle Size: <4 microns) were purchased from EDM Inc., MN, USA. All other chemicals used were high purity analytical grade.

6.2.2 Voltammetry

Voltammetric studies were carried out with a CHI 6017E workstation (Austin, TX, USA) at room temperature (25 °C) under a nitrogen atmosphere. A 3-electrode system consisting of a HPG electrode modified with MWNT/Py surface and attached with MP-11 as the working electrode, an Ag/AgCl (3 M KCl) reference electrode, and a platinum wire auxiliary electrode were used. Prior to surface modification, the HPG electrodes were sanded to expose a fresh surface by polishing on a SiC paper (P320 grit) followed by sonication in ethanol-water mixture and drying under nitrogen. The rotating disk voltammetry (RDV) was performed at a rotation rate of 1000 rpm using an EcoChemie Auto lab rotator system equipped with a motor controller unit (Metrohm Inc., USA).

6.2.3 Preparation of MP-11 Fims on MWNT/Py Modified Electrodes.

The procedure to prepare MWNT/Py modified electrodes and covalent MP-11 immobilization is similar to our group's prior report.[4] In brief, to the polished and cleaned surface of HPG electrodes (geometric area 0.2 cm^2), a 15 µL suspension of 1 mg/mL MWNT in dimethylformamide (DMF) was added and allowed to dry at room temperature. Following this, a 10-µL aliquot of 1-pyrenebutyric acid (Py, 10 mM) in DMF was added to each electrode. The electrodes were covered with a moisturized beaker (to avoid the Py solution from drying) and allowed for 1 hour to form the strong π-π stacked MWNT/Py assemblies. Then the electrodes were rinsed well with water.

For the selective covalent attachment of MP-11 through the free amine groups (Lys-13 and N-terminus Val-11), MWNT/Py electrodes were treated with a freshly prepared mixture of 0.35 M 3-[3- dimethylaminopropyl]carbodiimide hydrochloride (EDC) and 0.1 M N-Hydroxysuccinimide (NHS) to activate the carboxylic acid surface groups of Py by reacting for 10 min. The electrodes

were rinsed in deionized water and subsequently 20 µL of MP-11 (1 mM in 0.1 M PBS) were added, and the solution was incubated for 1 hour at 4 °C to obtain MP11-amine$_{cov}$ films.

6.2.4 Characterization of MP11-aminecov Films

The characterization and surface morphological studies of the designed MWNT/Py modified electrodes and those attached with MP-11 films were carried out by Raman spectroscopy (Nicolet NXR FT-Raman module, Nd:YVO4 laser, 0.2 W, resolution 4 cm^{-1}), Fourier transform infrared spectroscopy in the attenuated total reflection mode (Varian 800 FTIR, Scimitar Series), scanning electron microscopy (SEM), energy dispersive spectroscopy (EDS, FEI Quanta 600 field emission gun ESEM with Evex EDS and HKL EBSD) and transmission electron microscopy (TEM, JEOL JEM-2100).

6.3 Results and Discussion

The MP-11 used in this study was the sodium salt of microperoxidase prepared from equine heart cytochrome c by peptic digestion. The direct electrochemistry of MP-11 films on high purity graphite (HPG) electrodes modified with multiwalled carbon nanotubes (MWNT) and π-π stacked with 1-pyrenebutyric acid (MWNT/Py) was investigated by cyclic voltammetry. The covalent attachment of the two MP-11 amine groups (N-terminus Val-11 and Lys-13) to the terminal carboxylic acid groups of Py in MWNT/Py surface was through the amine-carboxylic acid coupling chemistry, similar to that reported previously (denoted as MP11-aminecov film, see Figure 1).[4]

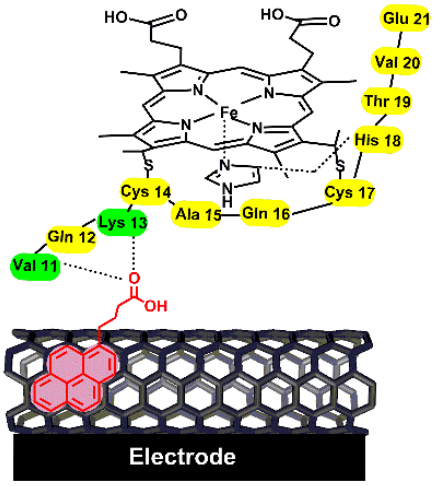

Figure 1. Representation of the covalent immobilization of MP-11 on MWNT/Py modified HPG electrodes.

Figure 2 shows that the characteristic D and G bands of MWNT in the Raman spectrum were shifted to lower frequencies as a result of π-π interaction with Py molecules.[26,27] Thus, Raman spectroscopy confirmed the π-π stacking of Py with surface MWNT coated on HPG electrodes.

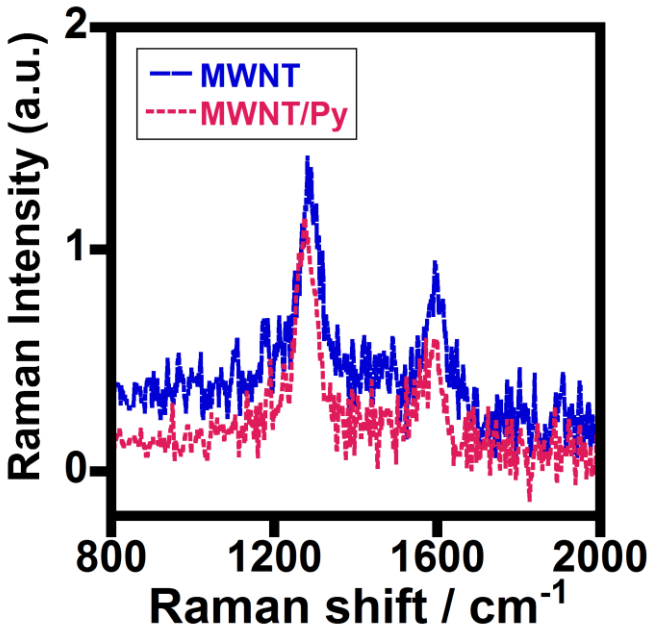

Figure 2. Raman spectra of MWNT and MWNT/Py films on HPG electrodes.

The formation of MP-11 films on the surface of MWNT/Py electrodes was confirmed by Fourier transform infrared spectroscopy operated in the attenuated total reflection mode (FTIR-ATR, see Figures 2). The HPG electrode and MWNT showed the carbonyl vibration peaks at 1660 cm^{-1} (see Figure 3b). The FTIR spectra were taken after each modification step on HPG electrodes (Figure 3c-f). The MP-11 exhibited peaks between the regions 1500-1600 and 1600-1700 cm^{-1}, which were assigned to the amide-I C=O and the amide-II N-H bending frequencies typical of a peptide backbone.[28.29] The free amine groups of MP-11 vibration bands (Lys-13 and N-terminus Val-11) were assigned at 1627 cm^{-1}. The MWNT/Py modified HPG electrodes exhibited bands at 1665 cm^{-1} for carbonyl stretching and a broad band at 3480 cm^{-1} for the –OH stretching, both are attributed to the end –COOH groups of the Py-linker molecules.

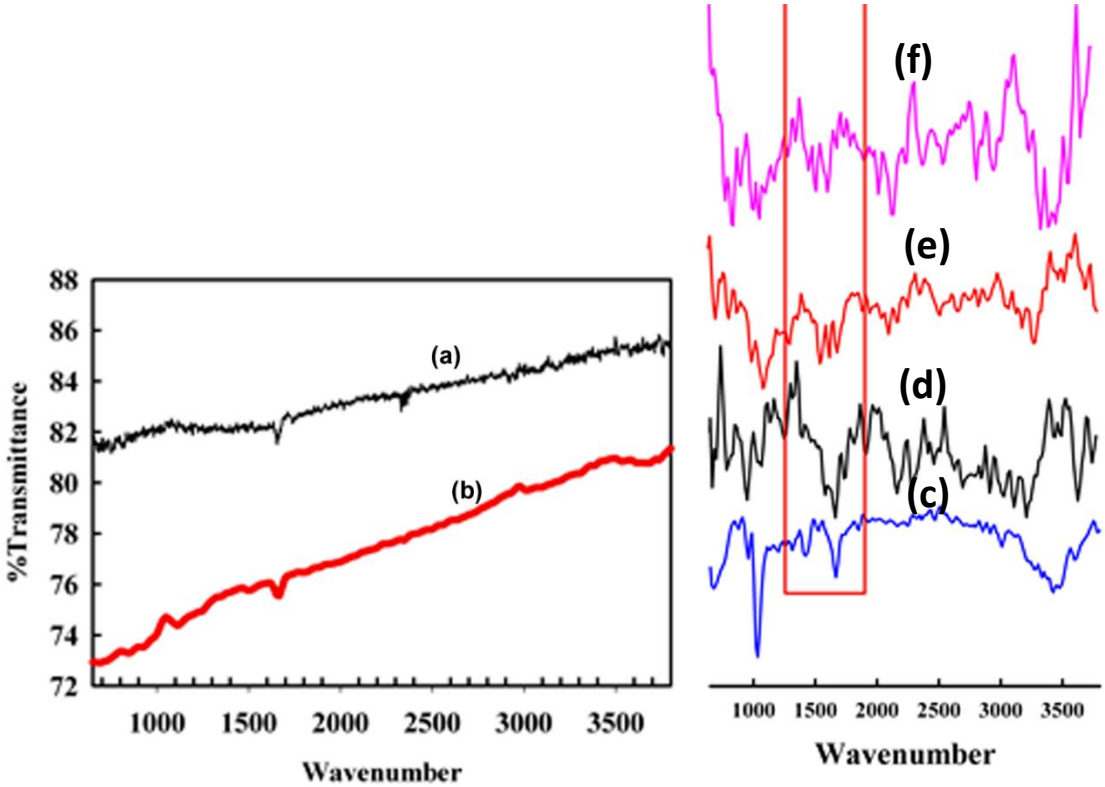

Figure 3. FTIR spectra of (a) only HPG; (b) only MWNT; (c) MWNT/Py; (d) EDC-NHS treated MWNT/Py; (e) MP11-$amine_{cov}$ films; and (f) only MP-11.

The EDC-NHS treatment of MWNT/Py assemblies led to the disappearance of the –OH stretching band of –COOH (originally at 3480 cm^{-1}) due to its conversion to N-succinimidyl groups and the appearance of new peaks centered at 1452 and 1769 cm^{-1} were attributed to C-N and C=O stretchings, respectively.[30] The IR-spectrum obtained after the covalent bonding of MP-11 to MWNT/Py assemblies depicted characteristic bands for peptide amide-I and amide-II bonds in the region of 1500 to 1700 $cm^{-1.}$ Additionally the appearance of bands in the region of 3270 to 3400 cm^{-1} represent the amide A and B bonds of MP-11.[2] Taken together, the FTIR characterization confirmed the covalent immobilization of MP-11 to MWNT/Py units on HPG electrodes.

The attachment of MP-11 to MWNT/Py units was also confirmed by surface morphological characterization using scanning electron microscopy (SEM, see Figure 4), transmission electron microscopy (TEM, see Figure 5), and energy dispersive spectroscopy (EDS, see Figure 6).

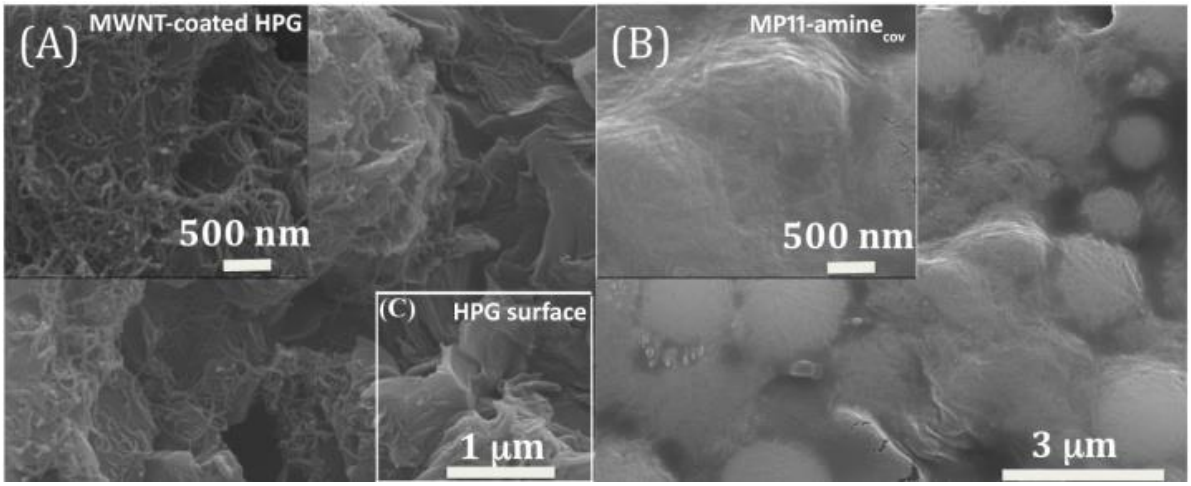

Figure 4. SEM images for (A) HPG/MWNT/Py and (B) MP11-aminecov films. (C) The image of a bare HPG surface displaying the texture of graphite flakes is shown for comparison.

For the SEM imaging, polished HPG surface was only partially modified with MWNT/Py assembly to allow the comparison of bare HPG surface and that coated with MWNT. As can be seen from Figure 4, the HPG surface showing platelet like features is covered by bundles of MWNT (see Figure 4C and 3A). After the covalent attachment of MP-11 via amine groups, the MWNT/Py features were buried under the peptide film and resulted in a fiber-like texture (see Figure 4B). The TEM images additionally supported the inferences obtained from SEM (see Figure 5).[31] The presence of Fe and S (possibly from the MP-11 heme and cysteinyl sulfur, respectively) identified in the EDS analysis further confirmed the immobilization of MP-11 on the MWNT/Py modified electrodes (see Figure 6).[32]

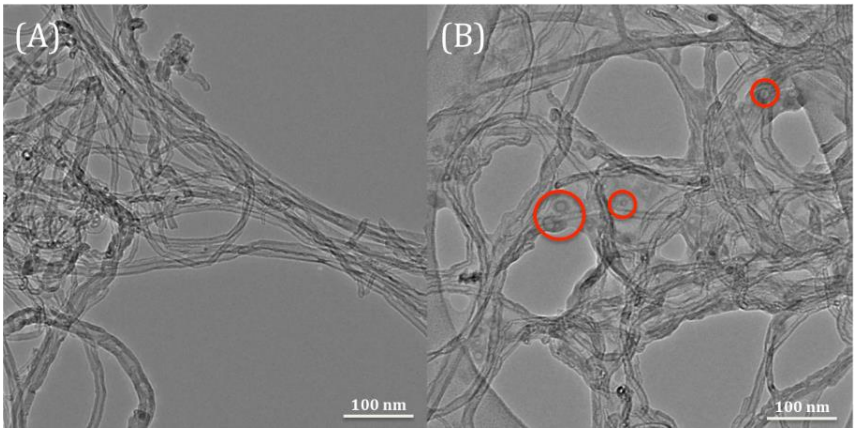

Figure 5. TEM images for (A) MWNT/Py and (B) MP11-aminecov films (MP-11 features around the tubes are circled).

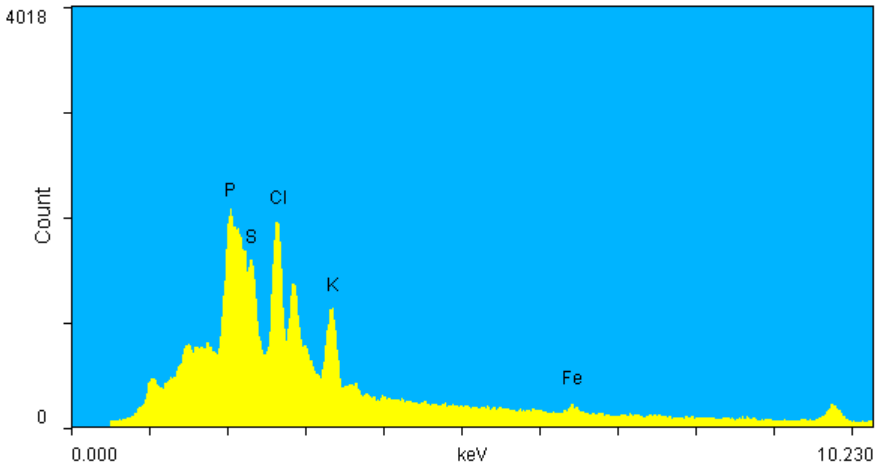

Figure 6. EDS of the MP11-aminecov film. The presence of P, K, and Cl peaks is attributed to arise from PBS.

Electrochemical studies were carried out to investigate the effect of MP-11 immobilization onto the pyrene linkers of MWNT/Py modified electrodes with respect to the electroactive MP-11 amount, direct electron transfer (ET) rates, and organic peroxide reduction currents. The cyclic voltammograms of the designed MP11-aminecov film in 0.1 M phosphate buffer saline (PBS), pH 7.4 displayed well-defined quasi-reversible redox peaks, and indicated the direct electron transfer between the heme cofactor of MP-11 and the MWNT/Py modified electrode surface (see Figure 7A a). Similarly, the control MP-11 films coated on only HPG or HPG/Py or HPG/MWNT electrodes showed reversible voltammograms, however, at more positive $E^{o'}$ values due to the differences among the electrode surfaces that can possibly influence the MP-11 arrangements (see Figure 7A b-d and Table 1). In the absence of immobilized MP-11, the MWNT/Py modified electrode alone or only the HPG electrode did not show any redox peaks (see Figure 7B). This confirmed that the observed voltammetry in Figure 7A was of MP-11.

In fact, the large double layer capacitance of MWNT/Py modified HPG electrode indicated the feature of high surface area [see Figure 7B(a)] and also suggested a supercapacitor property that has been shown for MWNT electrodes.[33] By plotting the charging current densities with scan rates for the HPG/MWNT/Py and bare HPG electrodes, the capacitance values of each electrode from the slopes of the resulting plots (see Figure 8) was obtained.[34] By this procedure, it was determined that the capacitance of HPG/MWNT/Py was 1066 μF cm^{-2} and that of the polished HPG surface was 367 μF cm^{-2}. This indicated that the MWNT/Py modification on HPG electrode offered an ~3-fold greater electroactive surface area than the unmodified HPG electrode.

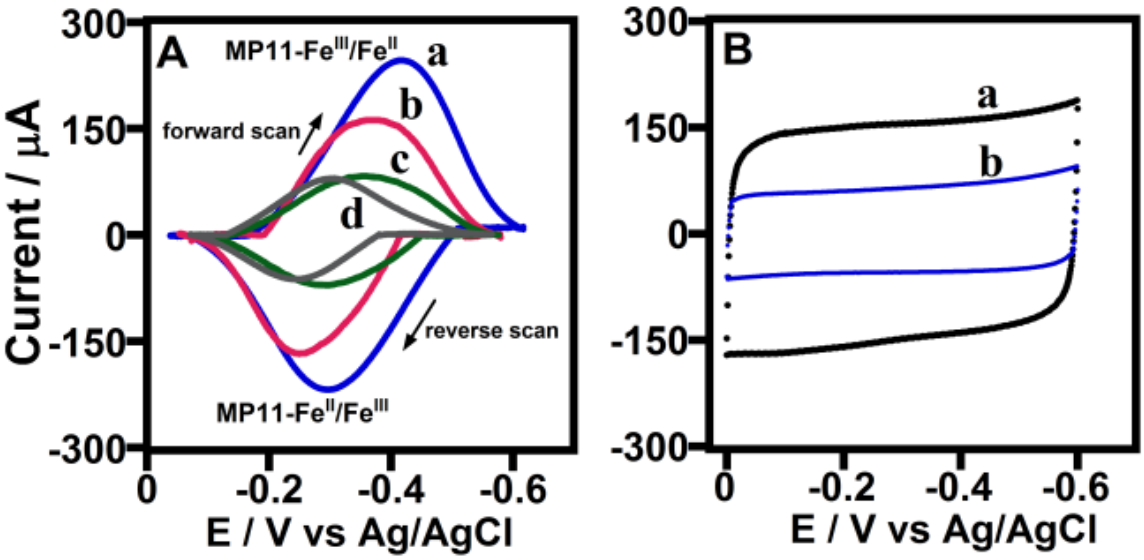

Figure 7. (A) Background subtracted cyclic voltammograms of a. MP11-aminecov, b. MWNT-MP11 (EDC/NHS activated MWNT, but no pyrene linker), c. HPG/Py-MP11 with no MWNT, and d. HPG/MP11 with no Py and MWNT at 0.7 V/s in pH 7.4, PBS. (B) Cyclic voltammograms of a. MWNT/Py modified electrode and b. only HPG electrode with no MP-11 film.

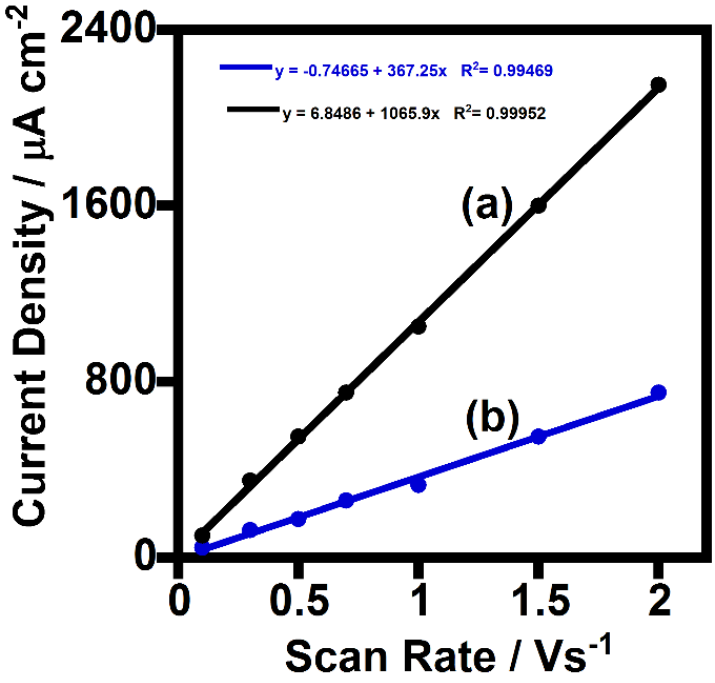

Figure 8. Current density versus scan rate plot for the charging currents measured for (a) HPG/MWNT/Py electrode and (b) polished HPG electrode in the absence of immobilized MP-11.

The cathodic (E_{pc}) and anodic (E_{pa}) peak separation (ΔE_p) with increasing scan rate of the MP11-aminecov film was used to calculate the standard ET rate constant (ks) by the Laviron's method.[35,36] A ks value of 4.6 ± 0.2 s-1 was obtained for the designed MP11-aminecov film. The electroactive surface concentration (Γ) of MP11-aminecov film was calculated by integrating the area of the reduction or oxidation peak (since the peak current ratio was close to unity).[4,36,37] The MP11-aminecov film exhibited an ~ 2-fold higher electroactive coverage than the MWNT-MP11 film (EDC/NHS activated MWNT) without the pyrene linker [see Figure 7A(b)], and ~ 3 to 4-fold enhancement in Γ than the films of HPG/Py-MP11 with no MWNT [see Figure 7A(c)] and HPG/MP11 with no Py and MWNT [see Figure 7A(d)] (see Table 1 for all values). This property confirms the unique role of the pyrene linkers in facilitating higher density covalent immobilization of MP-11 and the associated large electroactive enzyme coverage in the MP11-$amine_{cov}$ film over other control films.

Table 1. Comparison of the electroactive MP-11 amounts on MWNT/Py electrodes with control films and the reported myoglobin-$amine_{cov}$ film.

MP-11 Film	**Γ / pmol cm^{-2}**	**Ref.**
MP11-$amine_{cov}$ HPG/MWNT-MP11 HPG/MP11 HPG/Py-MP11	2385 ± 103 1250 ± 66 619 ± 28 746 ± 30	This study
myoglobin-$amine_{cov}$	300 ± 60	4

Furthermore, an 8-fold enhancement in Γ was obtained for the MP11-amine$_{cov}$ film when compared to a myoglobin film (-0.35 V vs Ag/AgCl, Table 1) attached similarly via surface amino groups on MWNT/Py modified electrodes (denoted as myogl obin-amine$_{cov}$, see Table 1).[4] The electroactive coverage of MP-11 films on the modified electrodes suggests the formation of multilayer films, with a highly possible electron self-exchange phenomenon occurring between adjacent MP-11 heme centers.[21,23,36]

The electrocatalytic property of the MP11-amine$_{cov}$ film and other control films was investigated by monitoring the reduction of *tert*-butyl hydroperoxide (t-BuOOH) to *tert*-butanol (t-BuOH). The larger electroactive MP-11 in the MP11-aminecov film led to a 1.5 to 2-fold greater catalytic reduction current density of this film over control MP-11 films (see Figure 9, Table 2). Thus, the enhancement effect of pyrene linkers on both the electroactive coverage and the electrocatalytic currents of immobilized MP-11 in the MP11-amine$_{cov}$ film can be understood. The currents were measured at the plateau region at -0.5 V vs Ag/AgCl, which is a high enough overpotential region, where the interfacial ET-rate is presumed to be not rate limiting.[10,11,36] The reduction currents were subtracted for the small background currents (≤ 5% of the catalytic current) from the respective electrodes with no immobilized MP-11 films (i.e., MWNT/Py, MWNT, HPG/Py, and only HPG; see Figure. 11b illustrates the background reduction currents from the HPG/MWNT/Py electrode).

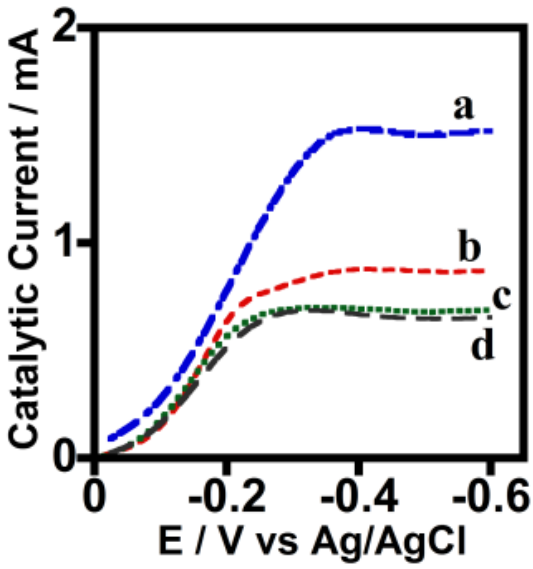

Figure 9. Electrocatalytic t-BuOOH (4.8 mM) reduction currents at 1000 rpm in PBS (pH 7.4), 25 ^{o}C, catalyzed by a. MP-amine$_{cov}$, b. MWNT-MP11 (EDC/NHS activated MWNT, but no pyrene linker), c. HPG/Py-MP11 with no MWNT, and d. HPG/MP11 with no Py and MWNT.

Table 2. Contribution of pyrene linker in enhancing the catalytic reduction currents of MP11-amine$_{cov}$ film over control films.

Enzyme film type	$E^{o'}$ (in V) vs Ag/AgCl	Catalytic Current Density (mA cm^{-2}) (at -0.5 V vs Ag/AgCl)
MP11-amine$_{cov}$	-0.36 (± 0.01)	7.5 ± 0.4
HPG/MP11 (no MWNT and Py-linker)	-0.28 (± 0.01)	3.4 ± 0.2
HPG/Py-MP11 (no MWNT)	-0.33 (± 0.01)	3.6 ± 0.1
HPG/MWNT- MP11 (no Py-linker)	-0.32 (± 0.03)	4.8 ± 0.2
myoglobin-amine$_{cov}$ (Ref. 4)	-0.35 (± 0.02)	4.1 ± 0.3

The t- The t-BuOOH reduction currents catalyzed by the MP11-aminecov film, versus the applied potential for increasing t-BuOOH concentrations, are shown in Figure 10.

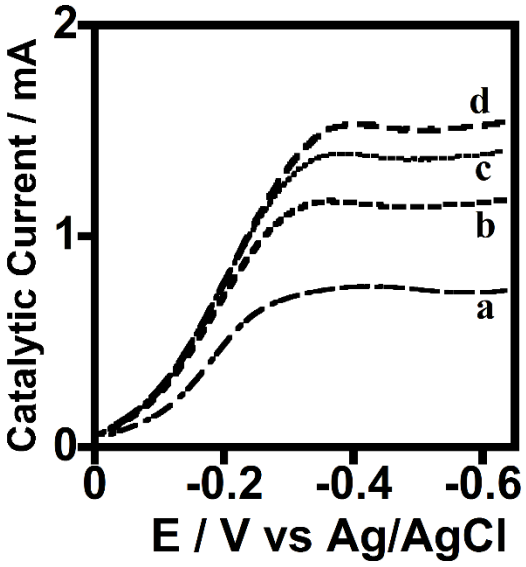

Figure 10. Reduction currents versus t-BuOOH concentration at 1000 rpm catalyzed by the MP11-amine$_{cov}$ film in pH 7.4 PBS for **a.** 0.8, **b.** 1.6, **c.** 3.2, and **d.** 4.8 mM t-BuOOH.

The catalytic reduction current density (current divided by the electrode geometric area) versus the concentration of t-BuOOH present in solution is shown in Figure 11a. The small background reduction currents from the MWNT/Py electrodes with no MP-11 film are shown in Figure 11b.

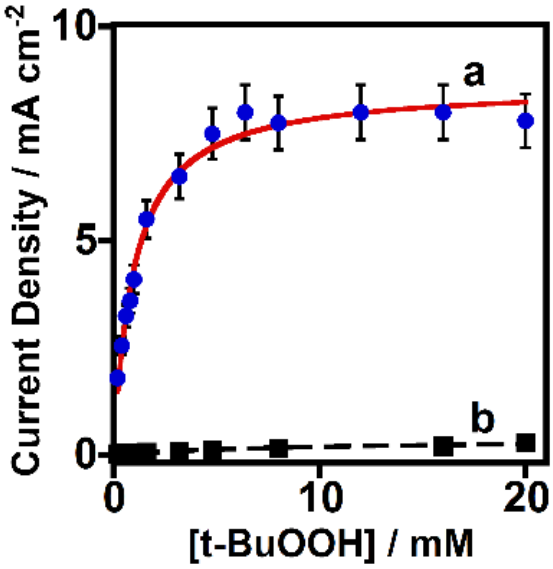

Figure 11. Catalytic current densities with t-BuOOH concentration at 1000 rpm for the designed (a) MP11-aminecov film and (b) MWNT/Py electrode in the absence of attached MP-11 in pH 7.4, PBS, 25 ^{o}C.

The designed MP11-amine$_{cov}$ film exhibited a high electrocatalytic activity with a current density of 7.5 mA cm^{-2} towards an organic peroxide reduction. The current density is greater by about 2–fold than the myoglobin-amine$_{cov}$ films.[4] This feature can be attributed to the small size of MP-11 heme peptide favoring high density surface concentration compared to the relatively large myoglobin protein. More interestingly, the apparent Michaelis-Menten constant (Kmapp) obtained from the Michaelis-Menten fit of reduction current density plot (Figure 11a) of the designed MP11-aminecov film (K_m^{app} = 1 mM) is 12-fold smaller than that observed by us for the myoglobin-amine$_{cov}$ film (K_m^{app} = 12 mM).[4] This suggests the stronger affinity of short MP-11 peptide by the designed covalent strategy over the similarly prepared large myoglobin protein film towards an organic peroxide substrate.

6.4 Conclusions

The results presented demonstrate that the π-π stacking of pyrene linkers with carbon nanotubes offers enhanced electroactive redox protein molecules and catalytic currents probably by retaining the innate electronic properties of MWNT and additionally by the presence of a large number of stacked pyrene units for high density, stable covalent enzyme immobilization. Furthermore, the findings above suggest a new potential direction in achieving high electrocatalytic activities of a large, fragile, redox-center buried, or otherwise difficult to study metalloenzymes by mutating them into small catalytically active redox domains to effectively connect with electrodes.

6.5 References

1. C. Leger and P. Bertrand, *Chem. Rev*., **2008**, *108*, 2379–2438.
2. Walcarius, S. D. Minteer, J. Wang, Y. Lin and A. Merkoci, *J. Mater. Chem. B,* **2013**, *1*, 4878-4908.
3. E. S. Redeker, D. T. Ta, D. Cortens, B. Billen, W. Guedens and P. Adriaensens, *Bioconjugate. Chem*., **2013**, *24*, 1761–1777.
4. C. Walgama and S. Krishnan, *J. Electrochem. Soc.*, **2014**, *161*, H47-H52.
5. Willner and E. Katz, *Angew. Chem. Int. Ed.,* **2000**, *39*, 1180−1218.
6. E. Lojou, *Electrochim. Acta,* **2011**, *56*, 10385-10397.
7. M. Calvaresi and F. Zerbetto, *Acc. Chem. Res.,* **2013**, *46*, 2454–2463.
8. R. J. Chen, Y. Zhang, D. Wang and H. Dai, *J. Am. Chem. Soc.,* **2001**, *123*, 3838-3839.
9. J. Gooding, R. Wibowo, J. Q. Liu, W. R. Yang, D. Losic, S. Orbons, F. J. Mearns, J. G. Shapter and D. B. Hibbert, *J. Am. Chem. Soc.,* **2003**, *125*, 9006–9007.
10. G. Göbel and F. Lisdat, *Electrochem. Commun.*, **2008**, *10*, 1691-1694.
11. S. Krishnan and F. A. Armstrong, *Chem. Sci.,* **2012**, *3*, 1015–1023.
12. Halamkova, J. Halamek, V. Bocharova, A. Szczupak, L. Alfonta and E. Katz, *J. Am. Chem. Soc*., **2012**, *134*, 5040−5043.
13. Wang, F. Zhao, Y. Liu and S. Dong, *Biosens. Bioelectron*., **2005**, *21*, 159-166.
14. T. Mashino, S. Nakamura, M. Hirobe, *Tetrahedron Lett.* **1990**, *31*, 3163-3169.
15. E. Ryabova and E. Nordlander, *Dalton Trans*., **2005**, *7*, 1228–1233.
16. T. L. Poulos, *J. Biol. Inorg. Chem*., **1996**, *1*, 356–359.
17. F. Mazzei, G. Favero, F. Frasconi, A. Tata and F. Pepi, *Chem. Eur. J.*, **2009**, *15*, 7359–7367.
18. E. Katz and I. Willner, *Langmuir* **1997**, *13*, 3364-3373.

19. T. Lotzbeyer, W. Schuhmann, E. Katz, J. Falter and H.-L. Schmidt, *J. Electroanal. Chem*., **1994,** *377*, 291–294.

20. T. Lotzbeyer, W. Schuhmann and H.-L. Schmidt, *J. Electroanal. Chem.,* **1995**, *395*, 341–344.

21. T. Ruzgas, A. Gaigalas and L. Gorton, *J. Electroanal. Chem*., **1999**, *469*, 123–131.

22. Y. Liu, M. Wang, F. Zhao, Z. Guo, H. Chen and S. Dong, *J. Electroanal. Chem*. **2005**, *581*, 1–10.

23. Yarman, T. Nagel, N. Gajovic-Eichelmann, A. Fischer, U. Wollenberger and F. W. Scheller, *Electroanalysis*, **2011**, *23*, 611-618.

24. Renault, C. P. Andrieux, R. T. Tucker, M. J. Brett, V. Balland and B. Limoges, *J. Am. Chem. Soc.,* **2012**, *134*, 6834−6845.

25. S. Tian, Q. Zhou, Z. Gu, X. Gu, L. Zhao, Y. Li and J. Zheng, *Talanta*, **2013**, *107*, 324–331.

26. Y. Zhang, S. Yuan, W. Zhou, J. Xu and Y. Li, *J. Nanosci. Nanotechnol.,* **2007**, *7*, 2366.

27. Q. Yang, L. Shuai, J. Zhou, F. Lu and X. Pan, *J. Phys. Chem. B*, **2008**, *112*, 12934.

28. M. F. Cabral, J. D. Barrios, E. M. Kataoka, S. A. S. Machado, E. Carrilho, C. D. Garcia and A. A. Ayon, *Colloids Surf. B*, 2013, **103**, 624– 629.

29. L. K. Tamm and S. A. Tatulian, *Q. Rev. Biophys*., 1997, **30**, 365-429.

30. A. Barth, *Prog. Biophys. Mol. Bio*., 2000, **74**, 141-173.

31. D. Zhang, L. Zhang, L. Shi, C. Fang, H. Li, R.Gao, L. Huang and J. Zhang, *Nanoscale*, **2013**, *5*, 1127.

32. D. Zhang, L. Zhang, C. Fang, R. Gao, Y. Qian, L. Shi and J. Zhang, *RSC Adv*., **2013**, *3*, 8811.

33. E. Frackowiak, K. Metenier, V. Bertagna and F. Beguin, *Appl. Phys. Lett.*, **2000**, *77*, 2421.

34. D. Svedruzic, J. L. Blackburn, R. C. Tenent, J.-D. R. Rocha, T. B. Vinzant, M. J. Heben and P. W. King, *J. Am. Chem. Soc.,* **2011**, *133*, 4299.

35. E. Laviron, *J. Electroanal. Chem*., **1979**, *101*, 19-28.

36. S. Krishnan, A. Abeykoon, J. B. Schenkman and J. F. Rusling, *J. Am. Chem. Soc.*, **2009**, *131*, 16215.

37. S. Krishnan and C. Walgama, *Anal. Chem.* **2013**, *85*, 11420.

CHAPTER 7

SUMMARY

Analytical methodologies to facilitate the drug development process have been one of the foci of the research outlined in this dissertation. Optical approaches for cancer target identification and electrochemical approaches for preclinical drug screening and quality assurance have been the subject of exhaustive study. Under the theme of bio-electrocatalysis, nanostructure architectures for catalytic applications were also investigated. Furthermore, numerous analytical insights into biomedical and bioelectronics have been gained in these studies. The contributions made to analytical chemistry are summarized below.

In one study (see Chapter 2), surface plasmon resonance micro array imaging technique was successfully used to detect targeted cancer protein-protein interactions and to study small molecule inhibition of these interactions in a label-free manner. A rapid optical microarray imaging approach which includes the use of a mass sensor for validation was investigated for anti-cancer drug screening at specific cancer protein-protein interface targets with binding kinetics. SPRi demonstrated a 3.5-fold greater specificity for interactions between MDM2 and wild type p53 over a non-specific p53 mutant in a real time microfluidic analysis. Significant percentage reflectivity changes (Δ%R) in the SPRi signals and molecular level mass changes were detected for both the MDM2-p53 interaction and its inhibition by the small molecule Nutlin-3 drug analog known for its

anti-cancer property. Additionally, it was demonstrated that synthetic, inexpensive binding domains of interacting cancer proteins are sufficient to screen anti-cancer drugs by an array-based SPRi technique with excellent specificity and sensitivity. This imaging array, combined with a mass sensor can be used to study any protein-protein interactions and to screen for small molecules with the desired binding and potency.

In another study (see chapter 3), a new method for pre-clinical drug screening was demonstrated by designing a one-step, rapid microsomal electrochemical bioreactor technology for drug metabolite synthesis and inhibition. In order to design a green microsomal bioreactor on suitably identified carbon electrodes, it is important to understand the direct electrochemical properties at the interfaces between various carbon electrode materials and HLM. The novelty of this work was on the investigation of directly adsorbed HLM on different carbon electrodes with the goal to developing a simple, rapid, and new bioanalytical platform of HLM useful for drug metabolism and inhibition assays. These bio-interfaces were designed in this study using a one-step adsorption of HLM directly onto polished BPG, EPG, GC, or HPG electrodes. The estimated direct electron transfer rate constant of HLM on the smooth GC surface was significantly greater than that of the other electrodes. On the other hand, the electroactive surface coverage and stability of microsomal films were greater on a rough EPG and HPG electrode surface compared to smooth GC and less defective hydrophobic BPG surfaces. The presence of significantly higher oxygen functionalities and flatness of the GC surface was attributed to promote faster ET rates of the coated layer of the thin HLM film compared to the EPG, BPG, and HPG electrodes. The cytochrome P450-specific bioactivity of the liver microsomal film on the catalytically superior, stable HPG surface was confirmed by monitoring the electrocatalytic conversion of testosterone to 6β-hydroxytestosterone and its inhibition by the CYP-specific ketoconazole inhibitor. The identification of optimal HPG and EPG electrodes to design biologically active interfaces with liver microsomes was suggested

to have immense significance in the design of one-step, green bioreactors for stereo-selective drug metabolite synthesis and for drug metabolism and inhibition assays.

In a third study (see chapter 4), single drop electroanalysis was demonstrated as a cost-effective and instant analytical strategy for the quality assurance of active pharmaceutical ingredients in drugs. Single drop electroanalytical measurements of pharmaceutically and biologically relevant compounds using screen printed electrodes modified with MWNT-COOH as the sensor surface were studied. Acetaminophen, nicotine, ascorbic acid, and the reduced form of nicotinamide adenine dinucleotide were detected in a single drop of solution. It was shown that combined polar and nonpolar interactions of analytes with –COOH functional groups and large surface area of MWCNT, respectively, allow highly sensitive analyte detection with wide dynamic range. Smaller analytes could bind to a significantly greater number of sensor sites than bulkier analytes and offer better detection sensitivity. Results suggested that sensitivity is controlled by predominant nonpolar interactions which an analyte can undergo with the MWCNT-COOH SPE sensor surface, whereas the limit of detection was controlled by the extent of polar interactions between an analyte and the sensor surface, facilitating interfacial charge transport and an electrochemical signal output. This could be a likely reason for why sensitivity does not need to always correlate with lower detection limits as variations in the interfacial interactions are critical. Application of the designed single drop method to a real sample was validated by estimating the amounts of acetaminophen, nicotine, ascorbic acid, and NADH in commercially available pharmaceuticals with excellent recovery.

In a final study (see chapters 5), it was shown that edge-to-edge interaction between carbon nanotubes and edge plane electrodes plays an important role in exposing a large proportion of the basal planes of the CNTs to allow enhanced π-π stacking of a pyrenyl compound and subsequent

high density protein immobilization yielding large electrocatalytic currents. In the same way (see chapter 6), an exceptionally large electroactively connected MP-11 with strong affinity for an organic peroxide and offering a high electrocatalytic reduction current density of 7.5 mA cm^{-2} has been achieved for the first time. Insights into the multiwall carbon nanotube arrangement in controlling the pyrene stacking and subsequent covalent protein immobilization was significant for high efficient catalytic and sensing applications in modern bioelectronics.

These studies suggest several new optical and electrochemical approaches for high throughput drug screening and bio-inspired, stable nanostructure electrocatalytic platforms for green energy generation. The applicability of SPRi technology for array based detection of cancer protein interactions with binding kinetics can provide new insights to cancer research. Also, the simple construction of potential driven microsomal electrodes for drug metabolite synthesis, compared to conventional biological assays will have a positive impact on pre-clinical drug screening industry. Additionally, controlled and stable immobilization of biologically relevant enzymes onto nanostructured electrodes may generate new opportunities towards the development of high efficient biocatalytic systems.

VITA

Charuksha Thameera Walgama
Candidate for the Degree of
Doctor of Philosophy

Thesis: SURFACE PLASMON MICROARRAY AND VOLTAGE-DRIVEN BIOCATALYSIS FOR DRUG DEVELOPMENT AND BIOELECTRONICS

Major Field: ANALYTICAL CHEMISTRY

Biographical:

Education:

Completed the requirements for the Doctor of Philosophy in your Chemistry at Oklahoma State University, Stillwater, Oklahoma in July 2017.
Completed the requirements for the Bachelor of Science in Chemistry at University of Kelaniya, Sri Lanka in 2010.

Experience:

Graduate Assistant, Oklahoma State University (2012 -2017)

- Research fields – Micro-array sensors, Potential driven liver microsomal drug metabolizing platforms, Nanostructure electrode designs for sensing, catalytic and fuel cell applications
- Teaching – Advanced Analytical Chemistry laboratories, Organic Chemistry Laboratories, General Chemistry I and II laboratories.

Fellowships and awards:

- Joseph. W. Richards Summer Fellowship, Electrochemical Society (ECS), 2016
- Distinguished Graduate Fellow (DGF) Award, OSU Graduate College, 2015-2017
- Creativity, Innovation and Entrepreneurship (CIE) Scholar Award, OSU Spears School of Business, 2015
- O. C. Dermer Scholarship, Henry P. Johnston Fellowship, and Skinner Fellowship, OSU Chemistry Department, 2012-2016
- 1st place, Physical Sciences and Technology Division, 25th Annual OSU Research Symposium 2014

Professional Affiliations:

- Chair - Oklahoma region student chapter, Electrochemical Society (ECS), 2017
- Vice President – Chemistry Graduate Student Society, OSU, 2016-2017
- Student memberships - The Honor Society of Phi Kappa Phi (PKP), American Chemical Society (ACS), ECS, OSU Student Alumni Organization